

Studies on the Emergence of Order in Out-of-equilibrium Systems

by

Atanu Bikash Chatterjee

A Dissertation

Submitted to the Faculty of

WORCESTER POLYTECHNIC INSTITUTE

in partial fulfillment of the requirements for the degree of

Doctor of Philosophy

in

Physics

September 2020

Advisor:

Prof. Germano S. Iannacchione, Department of Physics, WPI

Committee Members:

Dr. Mor Nitzan, John Harvard and James S. McDonnell Fellow, Harvard University

Prof. Padmanabhan K. Aravind, Department of Physics, WPI

Prof. L. Ramdas Ram-Mohan, Department of Physics, WPI

Happiness cannot be pursued; it must ensue.

—Viktor Emil Frankl

Acknowledgement

I thank my advisor, Germano Iannacchione for his incredible mentorship and guidance over the last four years. Since the day I met him, he has been a consistent source of support and guidance. He always gave me the freedom to choose the direction I wanted to pursue in my research, and was ever receptive to my thoughts and ideas. In my lifetime, if I can become even a fragment of the scholar, teacher, and mentor that he is, I will have accomplished much.

As a young undergraduate engineering student in India, my aspirations to take up physics would have never materialized without the active encouragement and support of Georgi Georgiev. I am immensely grateful to him for nurturing my interests, and for supporting my decision to pursue a PhD in Physics.

My time here has been incredibly enriched by some outstanding members of the WPI Physics community. I consider myself lucky to have come into contact with brilliant teachers like Aravind K. Padmanabhan and L. R. Ram–Mohan. Their passion for teaching and research continues to inspire me, and their sustained help and support throughout has made my graduate school experience a positive one.

I would also like to thank Mor Nitzan for her support and encouragement, for agreeing to serve on my dissertation committee, and for her willingness to collaborate on future projects.

Over the course of my doctoral work, I had the great good fortune of interacting with a number of brilliant scientists – physicists, mathematicians, complexity theorists, and biologists – from all over the world: Yaneer Bar–Yam (NECSI and MIT), Carlos Gershenson (UNAM), Umberto Lucia (Torino), Cesar Hidalgo (Toulouse), Hiroki Sayama (Binghamton), Massimiliano Esposito (Univ. Luxembourg), Francis Heylighen (VUB), Giovanni Gallavotti (Roma), Jun Zhang (NYU), Gerard Jagers (Wageningen), Marios Kyriazis, Oren Raz (Weizmann), Roland Riek (ETH Zurich),

Felix Ritort (Univ. Barcelona), Naoki Masuda (Univ. Buffalo), and Ofer Feinerman (Weizmann). My interactions with them have not only been crucial to my research but have also inspired me and enriched my career in immeasurable ways.

I am equally grateful for the opportunity to interact and work with several brilliant young minds. Thanks are due to Thanh Vu, Noor Kawmi, Jocelyne Tamayo, Sean McGrath (Assumption College) and Yaofeng Wang, Emily Whittles, Nick Mears, and Yash Yadati (WPI) for their faith in me. I consider myself fortunate to have been able to mentor and guide them in their research. Undoubtedly, they have taught me much more than I could teach them.

On the personal front, I am thankful to Saarthak for his unwavering friendship through the years. I know I can always count on him. I am challenged to find the right words to adequately thank my parents. I am grateful to them for relentlessly supporting my intellectual pursuits, and for always pushing me to follow my dreams. Every day I realize how much they have done for me. I could not have asked for more.

Finally, I thank my partner, Stuti. Thank you for the coffee, for the conversations, for loving me, and for loving me back, but most of all, for your kindness that always manages to bring in some much-needed order when life appears out-of-equilibrium.

Abstract

A challenge in fundamental physics and especially in thermodynamics is to understand emergent order in far-from-equilibrium systems. While at equilibrium, temperature plays the role of a key thermodynamic variable whose uniformity in space and time defines the equilibrium state the system is in, this is not the case in a far-from-equilibrium driven system. When energy flows through a finite system at steady-state, temperature takes on a time-independent but spatially varying character. In this study, the convection patterns of a Rayleigh-Bénard fluid cell at steady-state is used as a prototype system where the temperature profile and fluctuations are measured spatio-temporally. The thermal data is obtained by performing high-resolution real-time infrared calorimetry on the convection system as it is first driven out-of-equilibrium when the power is applied, achieves steady-state, and then as it gradually relaxes back to room temperature equilibrium when the power is removed. This work provides new experimental data on the non-trivial nature of thermal fluctuations when stable complex convective structures emerge. The thermal analysis of these convective cells at steady-state further yield local equilibrium-like statistics as the temperature manifold bifurcates into regions of emergent order (sources) and disorder (sink). These localized domains which co-exist together, reveal equilibrium-like fluctuations for the temperature scalar. We extend these experimental results to derive a thermodynamic equation of state for a driven system with emergent order from the first principles. We present a field theoretic formalism by defining the Lagrangian density as a function of a generic thermodynamic scalar. Our definition of the thermodynamic Lagrangian density involves two components, the internal work or the coherent part which gives rise to

emergent order, and the internal dissipation or the incoherent part which acts as the internal sink. The salient feature of this formulation is that it takes into account the spatial and temporal gradients of the thermodynamic scalar as the system is driven out-of-equilibrium, similar to the Rayleigh-Bénard system. The action functional defined on this scalar manifold connects local equilibrium-like domains. On minimizing the action and solving the Euler-Lagrange equation, we obtain a generalized thermodynamic equation of state for a driven system with emergent order. In conclusion, these results correlate the spatial ordering of the convective cells with the evolution of the system's temperature manifold.

Contents

1	Introduction	1
2	Thermodynamics	7
2.1	Equilibrium Thermodynamics	7
2.2	Non-equilibrium Thermodynamics	12
2.2.1	The Non-equilibrium Steady-state	13
2.2.2	The Case of Local Equilibrium	17
3	A Prototypical Complex System	19
3.1	Self-organization and the Origin of Order	19
3.2	The Rayleigh-Bénard Convection	21
3.3	Perspectives from Fluid Mechanics	23
3.4	Experimental Methodology	24
3.5	Results and Discussion	31
3.5.1	Temporal Analysis	31
3.5.2	Spatial Analysis	37
4	Theoretical Formalism of a Complex System	45
4.1	Broken Symmetries	46
4.2	Foundations of a Theory	52

4.3	Thermodynamic Lagrangian	54
4.4	Equation of State with Emergent Order	58
5	Future Directions	62
5.1	Further Theoretical Considerations	62
5.2	Equilibrium Thermodynamics: Extended Discussion	64
5.3	Ising Model, Kuramoto Oscillators, and Turbulent Convection	66
6	Discussion and Conclusion	75

List of Figures

1.1	Examples of far-from-equilibrium phenomena: (left to right) molten glass freezing into a solid, high-strength light-weight nickel foam, styrofoam, swarming schools of fish, swirling storms, and far-from-equilibrium growth in snowflakes [1, 2]	2
1.2	a) Classical concept of a global minimization of a system's free-energy, \mathcal{F} that dictates the equilibrium (observed) value of some order-parameter ϕ_{eq} . b) A system driven out-of-equilibrium in which \mathcal{F} has multiple local minima but no global minima, and thermal energy is enough for many co-existing ϕ_i . c) A system driven far-from-equilibrium where $\mathcal{F}(\mathbf{r}, t)$ varies such that the thermal energy also exhibits a gradient in \mathbf{r} and t revealing a dynamically driven minima at ϕ_{loc} . The directional derivative of the temperature manifold, ∇T tells us how the system collapses into a state governed by ϕ_{loc} [3, 4].	4
2.1	Figure shows a one-to-one correspondence between a thermodynamic process macroscopically driven along an arbitrary path in a $P - V$ phase-diagram such that the work done, $\delta W = \int PdV$ (left) and the microscopic representation in a n -dimensional phase-space where work is given by, $\delta W = \int dq_i \dot{p}_i$ [5].	8

2.2	Figure depicts space and time-reversal symmetry in a system at equilibrium when subjected to a quasi-static process of mixing. Two types of particles (red and green) are allowed to mix once the partition is quasi-statically removed ($A \rightarrow D$). As the system goes through the states B , C , and E it is not only impossible to distinguish between the states but it is also equally impossible to predict the chronology of the events (temporal ordering of states).	11
2.3	a) Figure shows a theoretical Carnot engine, C , operating between the thermal reservoirs T_1 and T_2 ($T_1 > T_2$). It derives heat Q_1 from the reservoir kept at T_1 , rejects heat, Q_2 into the reservoir kept at T_2 while performing work, W . b) Figure shows a practical Carnot engine, C' , operating between two thermal reservoirs θ_1 and θ_2 kept at a steady-state by the constant heat influxes, q_1 and q_2 . It derives heat Q'_1 from the reservoir kept at θ_1 , rejects heat, Q'_2 into the reservoir kept at θ_2 while performing work, W' ($W' < W$) [4].	14
2.4	Figure shows a typical open thermodynamic system (canonical ensemble), for example, a plate with a thin film of fluid when heated from the bottom along z -axis. The rate of change in the energy (\dot{e}) of the system is balanced by the entropy (\dot{s}_{gen}) generated by it. As the system boundary does not move, the work done by the system is zero. T_0 is the temperature of the surrounding.	15

3.1	Cartoon illustrates the experimental configuration of the current study. The Rayleigh–Bénard system at steady–state is set up by heating a thin film of viscous liquid from the bottom (\dot{Q}). The temperature difference between T_{bottom} and T_{top} gives rise to convection rolls. While at steady–state, T_{bottom} is constant, real–time thermal imaging of the top layer is performed to extract the spatial and temporal distribution of T_{top} . The line cut of the thermal profile $T_{top}(\mathbf{r}, t)$ is also shown [6].	22
3.2	Figure illustrates the experimental setup with the copper pan ($2R = 0.225\text{ m}$), the three thermocouples (T_1, T_2, T_3), inlet and outlet ducts for the forced convective heat transfer, and the infra–red camera for real–time thermal imaging. The inlet and the outlet ducts are present on the top cover and the copper pan sits on a wooden bottom rest and a polyurethane foam foundation which acts as an insulator [6].	25
3.3	Figure shows Rayleigh–Bénard Convection setup: Top View (left) and Side View (right). All dimensions are in meters. The three thermocouples used to record the temperature of the pan, the inlet and the outlet of the heat–exchanger are denoted in blue (T_1, T_2 and T_3). The heater attached to the bottom of the copper pan is denoted in red. The thermal images are recorded from the top using an infra–red camera [7].	27
3.4	Figure shows the steady–state relationship between the infra–red camera recorded temperature and the base thermocouple temperature at different power settings for the five randomly chosen spots on the empty copper pan [7].	28

3.5	<p>a) Figure shows steady-state thermal images recorded for two thickness, $l_z = 4.74 \text{ mm}$ and 5.02 mm at various powers. b) Figure shows the time-evolution of the $l_z = 4.74 \text{ mm}$ at 95.0 W over a period of two hours. Note that the shown images are logarithmically placed in time [6].</p>	29
3.6	<p>a) Figure illustrates the temporal analysis of an arbitrary region of interest on the images as a function time as the system evolves from room temperature equilibrium to an out-of-equilibrium steady-state. b) Figure shows the regions of interest for the spatial analysis on the steady-state image of a Rayleigh-Bénard convection. The complete image is denoted by I, the annular region without any structures by R, the circle at the center by P, the upward (bright spots) and downward plumes (dark spots) by P_{hot} and P_{cold} respectively [6, 7]. . .</p>	30
3.7	<p>Figure shows on a semi-log scale the temperature mean and standard deviation as a function of time of the top of the silicone oil film as it responds to the applied heating power until steady-state is reached for various values of input power. The left axis corresponds to the temperature mean in degrees Celsius (solid blue circles) and the right axis corresponds to the standard deviation (solid red triangles). Plots a, c, e show heating profiles for a film thickness of $l_z = 4.74 \text{ mm}$, and plots b, d, f for $l_z = 5.02 \text{ mm}$. Note that the applied heating power in Watts are labeled by the far left y-axis [6].</p>	32

3.8	Figure shows on a semi-log scale the temperature mean and standard deviation as a function of time of the top surface of the silicone oil film as it relaxes to room temperature after the applied heating power is removed. The left axis corresponds to the temperature mean in degrees Celsius (solid blue circles) and the right axis corresponds to the standard deviation (solid red triangles). Plots <i>a</i> , <i>c</i> , <i>e</i> show cooling profiles for the film thickness of $l_z = 4.74 \text{ mm}$, and plots <i>b</i> , <i>d</i> , <i>f</i> for $l_z = 5.02 \text{ mm}$. Note that the applied heating power in Watts are labeled by the far left <i>y</i> -axis [6].	33
3.9	a), b) Figure shows the functional relationship between the standard deviation of the temperature for the non-pattern region with time as the Rayleigh-Bénard system evolves from a room temperature equilibrium to an out-of-equilibrium steady-state for $l_z = 4.74 \text{ mm}$ and 5.02 mm at 42.2 W and 66 W . In c) and d) the data is shown for the pattern region. In e) a comparison is done between the two thickness at 66 W with the time windows identified: cyan for 5.02 mm and light grey for 4.74 mm [7].	34
3.10	Figure shows the histograms for the scaled-thermal fluctuations averaged over time after the system has reached a steady-state on a semi-logarithmic scale. The panels a) denote the hot regions (P_{hot}), b) the entire region (P), and c) the cold regions (P_{cold}). The mean temperature, $\langle T \rangle$ (in $^{\circ}C$) of the various regions of interest are also denoted. The histograms are fitted with normal distribution functions all centered at zero [6].	36

3.11	Figure shows the histograms for the scaled-thermal fluctuations averaged in space after the system has reached a steady-state. The top panel shows the distributions for $l_z = 4.74 \text{ mm}$ and the bottom panel for $l_z = 5.02 \text{ mm}$. Panels <i>a)</i> and <i>c)</i> plots the scaled-fluctuation frequency counts for the patterned region, P with a kernel density estimate (dashed). Panels <i>b)</i> and <i>d)</i> plot the scaled-fluctuation frequency counts for the non-patterned annular region, R with a normal curve fit centered at zero (solid) [6].	39
3.12	a) Figure shows the mean thermal profiles of six spatially averaged horizontal lines for $L_z = 5.02 \text{ mm}$ (blue) and 4.74 mm (magenta) at 66 W . b) Figure shows the mean thermal profiles of six spatially averaged horizontal lines for $L_z = 5.02 \text{ mm}$ (blue) and 4.74 mm (magenta) at 42.2 W . The shaded bands about the mean thermal profiles represent the standard deviation [7].	40
3.13	a) Figure shows the two-point autocorrelation function, \mathcal{G}_2 as function of distance, r with exponential fits, $\mathcal{G}_2(r) \sim \exp(-\frac{r}{\xi})$ where ξ is the correlation length on a log-log scale. The data shown in grey filled-circles with a single fit is for the non-patterned region of interest (R), whereas the data shown in white-filled circles with two fits is for the region of interest that shows emergent structures (P). The shown analysis is run on a steady-state image for a 4.74 mm , 95 W sample at steady-state. b) Figure shows the time-dependence of the correlation length for a 4.74 mm sample at 23.8 W (green triangles) and 95 W (red and blue triangles) as it evolves from room-temperature equilibrium to an out-of-equilibrium steady-state on a semilog scale [6-8].	41

3.14	a) Figure shows the spatial autocorrelation data along with exponential fits for 4.74 mm sample at steady-state. b) Figure shows the distribution of the two correlation lengths as the 4.74 mm sample evolves into an out-of-equilibrium steady-state from room temperature equilibrium. The two distribution functions: normal (in magenta) and lognormal (in red) are also shown in the figure [6-8]. . . .	43
4.1	a) Figure shows a bimodal distribution of the temperature frequency distribution over a region of pattern. Two independent Gaussian fits are performed which are identified as ‘hot’ (in red) and ‘cold’ (in blue). The shaded region is the cumulative function obtained from the two independent fits. In b) and c) a threshold temperature, T_{th} is used to slice the data into two separate 1D arrays and their frequency histograms are plotted with the respective Gaussian fit functions. The normality is further tested in d) and e) by plotting the respective Q-Q plots at 95% CI [7].	47
4.2	a) Figure shows the spatially averaged temperature in different regions of interest as a function of time in a time-series plot. In b), c), and d) the time-series data is plotted as frequency histograms for ‘cold’ (in blue), whole (in light grey), and ‘hot’ (in red) regions respectively. In e), f), and g) the Q-Q plots are shown for each case to test for normality [7].	49

4.3	<p>Figure shows the temperature plots ($T_{P_{hot}}, T_{P_{cold}}, T_{cond}$ and T_{bottom}) for the steady-state images at different values of input power for a) $l_z = 4.74 \text{ mm}$ and b) $l_z = 5.02 \text{ mm}$. The inset plots capture the variation in the plume temperatures ($T_{P_{hot}}$ and $T_{P_{cold}}$) about the theoretical conduction temperature (T_{cond}) as a function of power. For details about the specific points denoted in the plots, refer Table 4.1. Also, note that ϵ is arbitrary [6].</p>	51
4.4	<p>Figure shows a typical Rayleigh-Bénard convection with emergent order. When the fluid film is heated from the bottom (z-axis), regions of order (ϵ_i) and disorder (ϵ_j) emerge on the top-layer of the fluid film (xy-plane). The presence of the internal gradients leads to internal currents, j_{ji} that converts heat (\mathcal{Q}) into work (\mathcal{W}), and j_{ij} dissipates order back to disorder. These local internal fluxes exist because the system as a whole is driven far-from-equilibrium, and one exists as long as the other does hence, $j_{ij} = -j_{ji}$. The distribution ($\rho(X)$) in the insets represent the statistical distribution of the temperature in the domains ϵ_i and ϵ_j. Since, local equilibrium hypothesis holds true, one can see that the distribution is normal and centered around the mean, $\langle X \rangle$.</p>	53

5.1	<p>a) Figure shows the scaled standard deviation (σ/σ_{max}) of the angular frequency as a function of time (log-scale) in a two-dimensional Kuramoto system on a lattice for different coupling strengths (κ). b) – d) Figures show scaled standard deviation of the temperature as a function of time (log-scale) for different fluid samples in a Rayleigh-Bénard convection system. Note that the Rayleigh number (Ra) changes from non-turbulent to turbulent. e) – h) Figures show the evolution of the order parameter (R) as a function of time (log-scale) for the four systems [9].</p>	67
5.2	<p>a) Figure shows the probability density functions (log-scale) for the scaled angular frequency fluctuation ($\delta\omega^*$). The initial randomized state data is fit with a Gaussian (in black) and the final state data is fit with a Lorentzian (in red). b) Figure shows the probability density functions (log-scale) for the scaled thermal fluctuation (δT^*) for two different fluid samples at room temperature along with respective Gaussian fits. c) Figure shows the probability density functions (log-scale) for the scaled thermal fluctuation for two different fluid samples at steady-state along with kernel density estimates (KDE). Note that in the final state the two samples correspond to two separate Rayleigh numbers. d) Figure shows the probability density functions (log-scale) for the scaled thermal fluctuation for two different fluid samples at steady-state along with respective Gaussian (in black) and Lorentzian (in red) tails. The absence of sufficient data points prevent us from fitting the final state data of the $Ra = 1790$ sample with a Lorentzian function [9].</p>	72

List of Tables

3.1	Table outlines thermal and material properties of the silicone oil sample that was used to perform the current study [10]. The units for viscosity (ν) is cSt , for density (ρ) kg/m^3 , for thermal conductivity (α) $W/m - K$, for specific heat ($c_{p_{oil}}$) ($J/kg - K$), for thermal diffusivity (α) m^2/s , and for thermal compressibility (β_T) m^2/N	28
4.1	Table shows the calorimetric data from the steady-state images at different powers for the two thickness ($l_z = 4.74\text{ mm}$ and 5.02 mm). The numbers listed in the first column denote the specified points in the plots shown in Figure 4.3. The top temperature (T_{top}) is recorded by the thermal camera, bottom temperature (T_{bottom}) by the thermocouple T_2 , the hot and cold spot temperatures ($T_{P_{hot}}$ and $T_{P_{cold}}$) are obtained by spatially averaging regions of interest (P_{hot} and P_{cold}) from the thermal images, conduction temperature (T_{cond}) is calculated from Equation 4.1, and the Rayleigh Number ($Ra = \frac{g\beta l_z^3}{\nu\alpha}(T_{bottom} - T_{top})$) from the listed values in Table 3.1 [6].	50

Chapter 1

Introduction

We live in a beautiful world, surrounded by objects and life-forms that continually evolve, adapt, and exhibit tremendous complexity as they steadily consume energy [1, 2, 11, 12]. Therefore, thermodynamics plays a crucial role in understanding how nature works. If one traces the development of classical thermodynamics back to antiquity, one will realize that we have been extremely successful in describing the thermodynamics of systems and processes at equilibrium. An isolated system in a state of complete equilibrium is ‘dead’ and is completely indistinguishable from its surrounding media, whereas an open system allows for a constant supply of energy that not only creates a state of dynamic equilibrium but also prevents the system from collapsing into a state of complete thermodynamic equilibrium [13, 14]. Therefore, it is apparent that most of what we see around us are thermodynamically ‘open’, and we lack sufficient tools to understand the origins of this emergent complexity. These systems, that are thermodynamically open are therefore ‘alive’ and are far-from-equilibrium as they continually exchange matter and energy with the surrounding media. The hallmark of such systems is their ability to spontaneously give rise to intricate patterns through local interactions. These emergent patterns

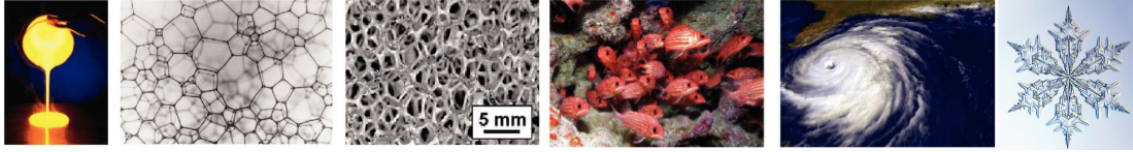


Figure 1.1: Examples of far-from-equilibrium phenomena: (left to right) molten glass freezing into a solid, high-strength light-weight nickel foam, styrofoam, swarming schools of fish, swirling storms, and far-from-equilibrium growth in snowflakes [1,2]

not only alter the material properties but also redistribute energy across a hierarchy of nested structures ranging from the microscopic to the macroscopic scale. One can find numerous examples in condensed matter physics, ranging from complex fluids such as, polymers, gels, colloids, liquid crystals, even biological materials and ensembles to granular systems [1,2,15,16]. While the spectrum of condensed matter systems those exhibiting emergent phenomena is fairly broad, it is important to understand the underlying processes as well which drive a system from a state of equilibrium to a state of stable dynamic equilibrium. Therefore, it is not surprising to know that far-from-equilibrium processes, that drive systems out-of-equilibrium also span a wide range of time-scales. From processes at macroscopic scale to molecular processes at the microscopic level; from processes as fast as electronic transition between states to processes as slow as glassy relaxation, one can find a wide spectrum of processes confined within these bounds. Some dramatic examples that span such a broad spatio-temporal scale include, turbulence in thermo-fluid convective phenomena, crack propagation in media, or the ever-changing weather patterns, see examples in Figure 1.1. Given the large phase-space of spatio-temporal scales, it is therefore, a challenging task to define a general framework that describes the dynamics of such a broad class of systems. Quite naturally, the study of such systems and processes lie at the intersection of complex systems science and condensed matter physics [12,15,17].

The complexity in these systems arises from the fact that they have numerous components that interact with each other in multiple ways. While these interactions are often random and stochastic, they lack a global control. From a thermodynamic perspective, a system as such is difficult to theorize. As one starts to formally describe such a system, one easily encounters numerous epistemological troubles. The first of which is to do with the concept of entropy, as the system is driven out-of-equilibrium it is natural to assume that a driven system will dissipate more and hence will have greater entropy (than a system at equilibrium). However, the origin of complexity implies that equilibrium structures representing global minima are replaced by higher-order organizational states consisting of various local metastable minima of different structures, see Figure 1.2 [3, 4, 18, 19]. Therefore, emergent order should reduce local entropy. Digging deeper leads to a more central problem in non-equilibrium thermodynamics, i.e. the definition of temperature for non-equilibrium states. Temperature, as an easily measurable thermodynamic quantity holds a prominent position in the canonical description of equilibrium thermodynamics. Therefore, its interpretation holds an equally important significance in the far-from-equilibrium description. In fact, in order to develop a ‘good’ theory for emergent order in far-from-equilibrium systems from first principles we need ‘good’ definitions for the underlying physical variables. Also, a theory that is physically sound must abide by the fundamental laws of nature, i.e. the first (the law of conservation of energy to be specific) and the second law(s) of thermodynamics. Therefore, one must exploit the symmetries present in the system leading to the origins of conserved quantities [20–23]. Classical and quantum physics has already mastered this approach through the description of space and time as a continuum and developing a field-theoretic framework around it using the principle of stationary action. Proceeding along those lines brings us to our final problem: the

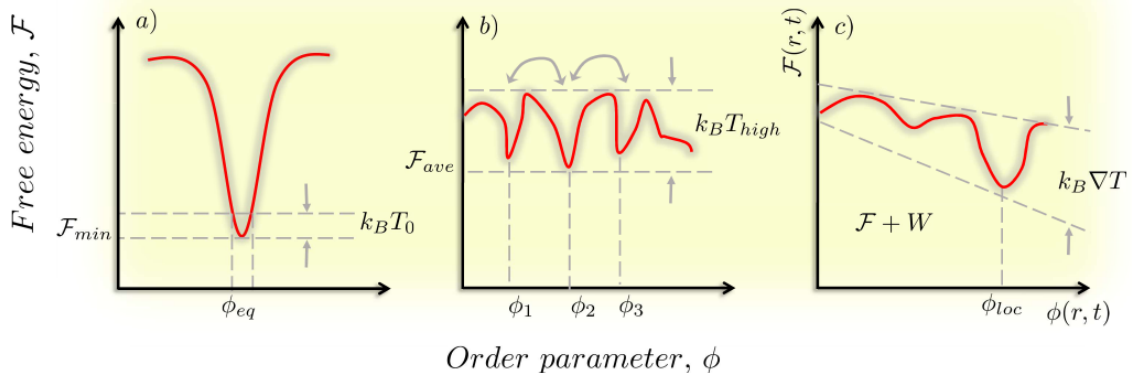


Figure 1.2: a) Classical concept of a global minimization of a system’s free–energy, \mathcal{F} that dictates the equilibrium (observed) value of some order–parameter ϕ_{eq} . b) A system driven out–of–equilibrium in which \mathcal{F} has multiple local minima but no global minima, and thermal energy is enough for many co–existing ϕ_i . c) A system driven far–from–equilibrium where $\mathcal{F}(\mathbf{r}, t)$ varies such that the thermal energy also exhibits a gradient in \mathbf{r} and t revealing a dynamically driven minima at ϕ_{loc} . The directional derivative of the temperature manifold, ∇T tells us how the system collapses into a state governed by ϕ_{loc} [3, 4].

definition of the system: dissipative or conservative and the constraints: holonomic and non–holonomic present in the system [24, 25].

We try to tackle these problems in this work, a step at a time. We start with our current understanding of the thermodynamics of equilibrium and non–equilibrium phenomena in the first chapter of the thesis. In the section, “Non–equilibrium Thermodynamics” we discuss the broad challenges and our state of knowledge in approaching such problems. We get into the details of two special cases in the study of non–equilibrium phenomena: “The Non–equilibrium Steady–state” and “The Case of Local Equilibrium”. We discuss them in detail along with the general class of fluctuation–dissipation theorems, the Onsager–Machlup formulation, Onsager’s reciprocal relations, and the Jarzynski equality. We proceed from there into the more central parts of the thesis that describe the actual work done during the doctoral research. In the chapter, “A Prototypical Complex System” we de-

scribe the general properties of a complex system, or what is meant by a complex system. We briefly discuss the process of self-organization in complex systems and how it is related to pattern formation in the section, “Self-organization and the Origin of Order”. One of the most commonly used complex system, the Rayleigh-Bénard convection is studied as a part of this doctoral work. We discuss the brief history and the wide range of contributions from the fluid mechanics community in the next two chapters: “The Rayleigh-Bénard Convection” and “Perspectives from Fluid Mechanics”. We discuss the setup used in this experimental study in great detail and the types of experimental studies done in the section, “Experimental Methodology”. Following which we present our results in the section, “Results and Discussion”. In sub-section, “Temporal Analysis” we discuss the results as the Rayleigh-Bénard system is driven in time from a room temperature equilibrium state to an out-of-equilibrium steady-state. While, in sub-section, “Spatial Analysis” we discuss the results as the stable patterns are analyzed to obtain insights about the nature of thermal fluctuations. We use our experimental results and move towards theoretical formalism in the chapter, “Theoretical Formalism of a Complex System”. In the section, “Broken Symmetries” we revisit the experimental results from the Rayleigh-Bénard study and derive inspiration to build a theory based on the definition of temperature under the conditions of local equilibrium hypothesis. In the following sections, we present our theoretical formalism in detail by first defining a thermodynamic Lagrangian and then solving the Euler-Lagrange equation to obtain a thermodynamic equation of state for driven systems with emergent order. In the chapter, “Future Directions” we present the various possible directions the research can be extended. In the chapter, “Further Theoretical Considerations” we discuss the possible extensions of the proposed theoretical formalism into Riemann geometry and fluid mechanics. Similarly, in “Equilibrium Thermodynamics:

Extended Discussion” we extend our understanding of temperature and its connections to ‘thermodynamic time’ through an action functional approach. Finally, we look for connections between our results with other systems which include driven Ising system, a system of Kuramoto oscillators and turbulent convection. We discuss these connections in detail in the section, “Ising Model, Kuramoto Oscillators, and Turbulent Convection”.

Chapter 2

Thermodynamics

Classical thermodynamics is perhaps one of the oldest and the most extensively studied branches of natural science and engineering. The laws of thermodynamics although being phenomenological in essence have never been found to violate any physical phenomena in nature. For reversible processes under the conditions of thermodynamic equilibrium, the first law of thermodynamics proposes that the energy must always be conserved, while the second law sets an upper bound to the practically realizable efficiency of a process [13, 26–28]. Due to their universal applicability, the laws of thermodynamics not only have consistently stood the test of time but also have become one of the cornerstones of classical and modern physics.

2.1 Equilibrium Thermodynamics

Thermodynamics of equilibrium phenomena is an extensively studied area in classical physics. A state of equilibrium is achieved when all the interactions present within a system are completely balanced. The best, as well as the most trivial example of such a system is the one in which the system is completely isolated from its surrounding media. As the system is completely isolated from its surroundings,

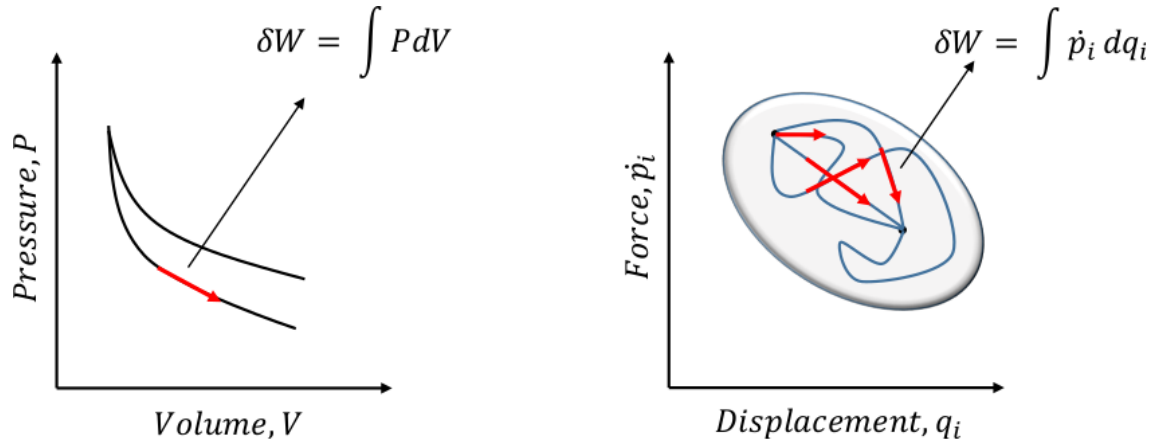


Figure 2.1: Figure shows a one-to-one correspondence between a thermodynamic process macroscopically driven along an arbitrary path in a $P - V$ phase-diagram such that the work done, $\delta W = \int P dV$ (left) and the microscopic representation in a n -dimensional phase-space where work is given by, $\delta W = \int dq_i \dot{p}_i$ [5].

the total energy of the system and the number of particles present inside the system remain constant over time. In the language of statistical mechanics, such a system is known as a micro-canonical ensemble. The micro-canonical ensemble is defined by assigning an equal probability to every micro-state whose energy falls within a range centered at $\langle E \rangle$ [29,30]. All the other micro-states have a probability of zero. Since the probabilities must add up to 1, the probability ρ is the inverse of the number of micro-states Z , or $\rho = 1/Z$. According to the second law of thermodynamics, the entropy of a micro-canonical ensemble must always increase, therefore, $S = k_B \ln Z$ or in terms of probability $S = -k_B \ln \rho$ [14]. Since, all the physical variables describing a micro-canonical ensemble are conserved in time, the system never evolves although its constituents are always in motion. Since, classical mechanics and statistical physics are very intimately connected, one can invoke the phase-space description of a physical system by defining a suitable Hamiltonian $H(p_1, \dots, p_n; q_1, \dots, q_n)$ in a n -dimensional phase-space [5,31]. In Figure 2.1, we present a pictorial representation of the connection by comparing a macroscopically

driven process in the $P - V$ phase-diagram with a phase-space interpretation between a pair of arbitrary micro-states. The pair (p_i, q_i) here denote the momenta and position of any arbitrary particle in the system. The distribution of the micro-states can be defined by a function (centered at $\langle E \rangle$), say $f(H - \langle E \rangle)$ then the total number of micro-states is given by,

$$Z = \frac{1}{h^n C} \int \dots \int dp_1 \dots dq_n f(H - \langle E \rangle) \quad (2.1)$$

The constant, C takes care of the double counting of states while h is the Planck's constant [32]. The total number micro-states, Z is also known as the partition function. Although, the micro-canonical ensemble sets the stage for a one-to-one correspondence between a phase-space description of matter and statistical interpretation of energy states, it however is not a physically realistic system. If a system is allowed to be driven in such a way that energy can penetrate through the system's boundary thus resulting in work generation, we have a system with closed boundaries (closed to exchange particles). Such a system is known as a canonical ensemble in the language of statistical mechanics [30]. The distribution of micro-states in a canonical ensemble follows a distinctive distribution, the Boltzmann distribution such that the probability, ρ_i of finding a micro-state with an arbitrary energy, e_i is given by,

$$\rho_i = \frac{1}{Z} e^{-\beta e_i}, \quad Z = \sum_i e^{-\beta e_i} \quad \text{with} \quad \beta = 1/k_B T \quad (2.2)$$

The canonical partition function is denoted above by Z also known as the trace of the density matrix in quantum statistical mechanics [28]. The canonical description of a thermodynamic system allows us to define measurable ensemble averages of physical variables, energy functions and the inter-relationships between them. In

an equilibrium process it is assumed that the system is driven from one equilibrium state to another equilibrium state quasi-statically. The free-energy of a canonical ensemble is given by, $F = -k_B T \ln Z$ and the first law can be written as,

$$F = \langle E \rangle - TS, \quad S = -\frac{\partial F}{\partial T} = -k_B \langle \log \rho \rangle \quad (2.3)$$

Generally speaking, any fluctuation in an extensive variable, X in a canonical ensemble can be quantified by considering its conjugate intensive pair, Y . Let us imagine a scenario where the temperature is fixed however the energy of the system fluctuates. Since, energy is extensive, and temperature intensive we can compute the mean energy of the system by,

$$\langle X \rangle = \pm \frac{1}{\beta} \frac{\partial \ln Z}{\partial Y} \quad (2.4)$$

The fluctuation in X is then expressed by the variance in the distribution of X , $\langle (\Delta x)^2 \rangle = \langle (X - \langle X \rangle)^2 \rangle$ and

$$\langle (\Delta x)^2 \rangle = \frac{1}{\beta} \frac{\partial \langle X \rangle}{\partial Y} = \frac{1}{\beta} \frac{\partial^2 \ln Z}{\partial Y^2} \quad (2.5)$$

The fluctuations arising in a system at equilibrium are due momentum exchange through collisions which are purely random in nature [28]. Therefore, the standard deviation in X decays as $\langle \Delta X \rangle / \sqrt{n}$, where n is the size of the system. In the thermodynamic limit, $n \rightarrow \infty$ one recovers the central limit theorem [33]. At this point, it is imperative to note one key aspect for a system at equilibrium: *symmetry*. Since, the collisions are completely random, the system is spatially homogeneous ($q \rightarrow -q$); and since a thermodynamic process is quasi-static in nature the system is also temporally homogeneous ($t \rightarrow -t; \dot{q} \rightarrow -\dot{q}$). In Figure 2.2, we present

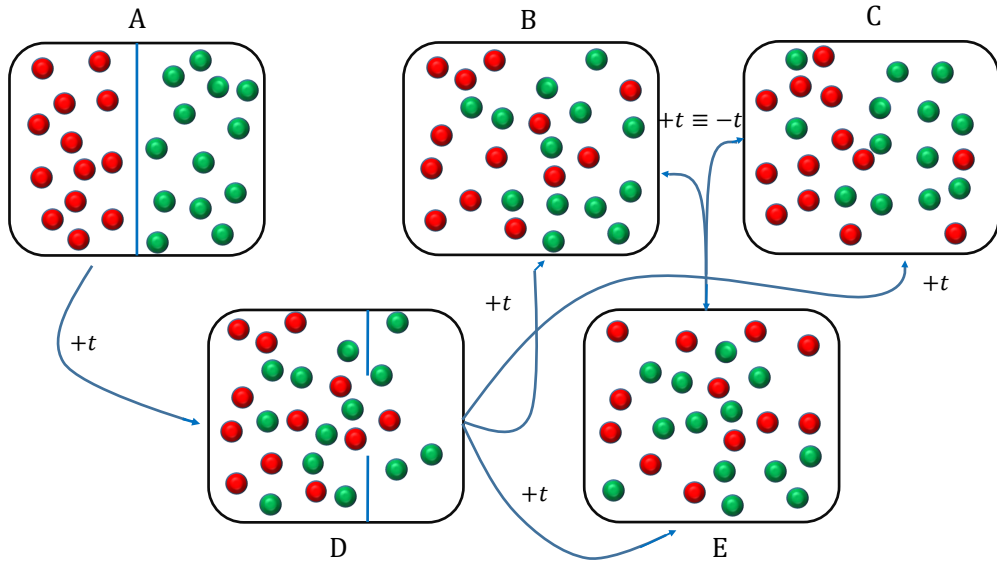


Figure 2.2: Figure depicts space and time-reversal symmetry in a system at equilibrium when subjected to a quasi-static process of mixing. Two types of particles (red and green) are allowed to mix once the partition is quasi-statically removed ($A \rightarrow D$). As the system goes through the states B , C , and E it is not only impossible to distinguish between the states but it is also equally impossible to predict the chronology of the events (temporal ordering of states).

pictorially a mixing of two types of particles (red and green) once the partition separating them is removed quasi-statically ($A \rightarrow D$). As the system goes through the states B , C , and E it is not only impossible to distinguish between the states but it is also equally impossible to predict the chronology of the states.

In the context of non-equilibrium thermodynamics, studying the fluctuations of thermodynamic observables in a system allows one to not only predict how far a system has been driven out-of-equilibrium but also estimate the non-equilibrium work done as the system is driven between two non-equilibrium states. In the following section we discuss some of the key ideas in this context, like the general class of fluctuation-dissipation theorems and the case of local equilibrium in non-equilibrium thermodynamics.

2.2 Non-equilibrium Thermodynamics

Non-equilibrium thermodynamics deals with systems that are not at equilibrium. As these systems are open to the surrounding media, they allow for external flows and fluxes to cross the system boundary and allow them to be driven out-of-equilibrium. Therefore, non-equilibrium thermodynamics is mainly concerned with transport processes, flows and fluxes. If we look around, we will find that we surround ourselves with systems which are thermodynamically open as they are constantly being fed with energy. Numerous examples of such actively driven systems include self-assembly in biological systems, reaction-diffusion process in chemical and ecological sciences, thermal-convective phenomena in fluid dynamics, geophysical and atmospheric sciences, fracture propagation in material sciences to name a few [2, 15, 16, 34–36]. The unifying theme across all of the above examples, from nanoscale to macroscale, is the staggering complexity that emerges spontaneously. Typically, far-from-equilibrium thermodynamics is treated as a natural extension of equilibrium thermodynamics [13, 37]. Although given the wide spectrum of phenomena and the inherent complexity associated with them, equilibrium thermodynamics becomes insufficient in explaining the underlying dynamics anymore. Successful modelling of non-equilibrium phenomena therefore primarily relies on its degree of closeness to its equilibrium counterpart, while extrapolating the thermodynamic variables used to quantify the system if it were in thermodynamic equilibrium. Some of the recent approaches include modeling non-equilibrium phenomena through stochastic Langevin dynamics (Wiener processes) or considering the statistical evolution of the time-dependent probability density function using the Fokker-Planck equation [34, 38]. However, in reality a simple theoretical Carnot engine, C that exchanges heat between two reservoirs maintained at different temperatures and

generates work, becomes incredibly difficult to visualize in practice, see Figure 2.3a. Even in order to maintain the heat baths at a constant temperature, a steady heat influx is mandatory. Thus, a practical Carnot engine, C' no longer remains as efficient as a theoretical Carnot engine, and its efficiency is now expressed as a function of steady-state non-equilibrium temperature of the baths and subsequent far-from-equilibrium correction, as shown in Figure 2.3b [3, 4]. Moreover, unlike equilibrium thermodynamics time-reversal symmetry is broken in the case of systems that are driven out-of-equilibrium. Therefore, non-equilibrium processes are entropy producing processes that follow irreversible trajectories in the phase-space. This leads to the objection that it should not be possible to formulate irreversible processes from time-symmetric dynamics, also known as the Loschmidt's paradox [5, 31, 39, 40]. Therefore, two special scenarios are explored in the subsequent sections where we discuss how macroscopic irreversibility appears naturally in systems that obey time reversible microscopic dynamics [37, 41, 42].

2.2.1 The Non-equilibrium Steady-state

A non-equilibrium steady-state is a self-sustaining steady-state which is achieved when the system has been driven and is constantly being kept at an out-of-equilibrium state. Standard examples include, bio-chemical reactions, material transport, cell signalling, turbulence in thermo-fluid media etc. The presence of a driving field implies that the system should be open to flows and currents. Therefore, thermodynamically open systems fall in this category. Classical thermodynamics allows us to quantify energy balance and material transport in open systems as they are excited. A typical example of an open system is shown in Figure 2.4. As thermal fluxes cross the system boundary, the system dissipates this flow of energy through it by generating entropy. Since, the system boundary does not move, net work done by

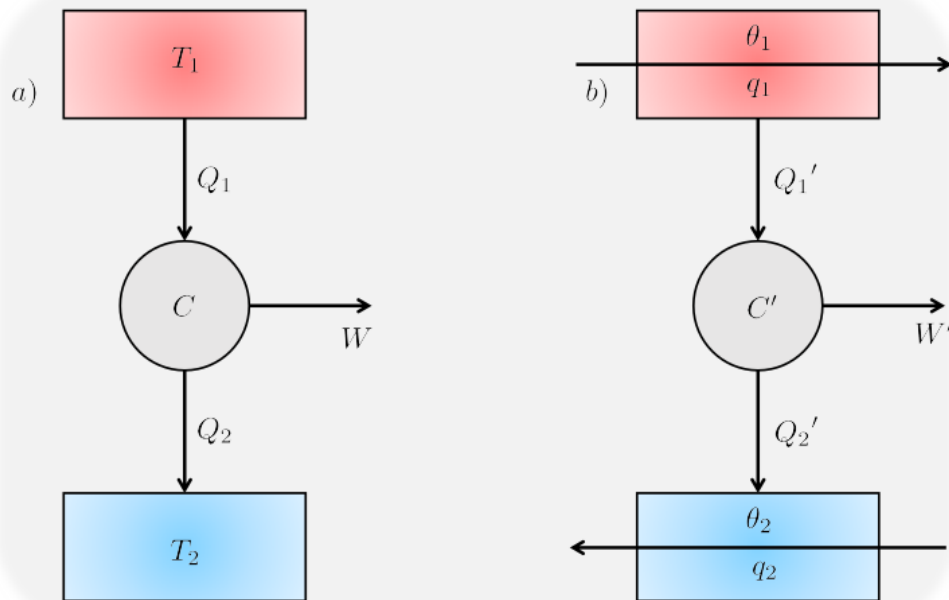


Figure 2.3: a) Figure shows a theoretical Carnot engine, C , operating between the thermal reservoirs T_1 and T_2 ($T_1 > T_2$). It derives heat Q_1 from the reservoir kept at T_1 , rejects heat, Q_2 into the reservoir kept at T_2 while performing work, W . b) Figure shows a practical Carnot engine, C' , operating between two thermal reservoirs θ_1 and θ_2 kept at a steady-state by the constant heat influxes, q_1 and q_2 . It derives heat Q'_1 from the reservoir kept at θ_1 , rejects heat, Q'_2 into the reservoir kept at θ_2 while performing work, W' ($W' < W$) [4].

the system is zero. The first law is preserved and in conjunction with the second law the total entropy generated is balanced by the net energy flux. A thermodynamic analysis as such, is reserved for either quasi-equilibrium or steady-state processes. Under such conditions, the system can be described like any other system which is at thermal equilibrium with its surroundings [11, 27, 32, 43, 44]. Since, an equilibrium state is often described as a special case of steady-state non-equilibrium thermodynamics. Therefore, using the right definitions of the thermodynamic variables and driving terms one can formulate the thermodynamics of non-equilibrium steady-states identically under the framework of equilibrium thermodynamics. One way is to generalize the Onsager-Machlup path integral approach for systems in

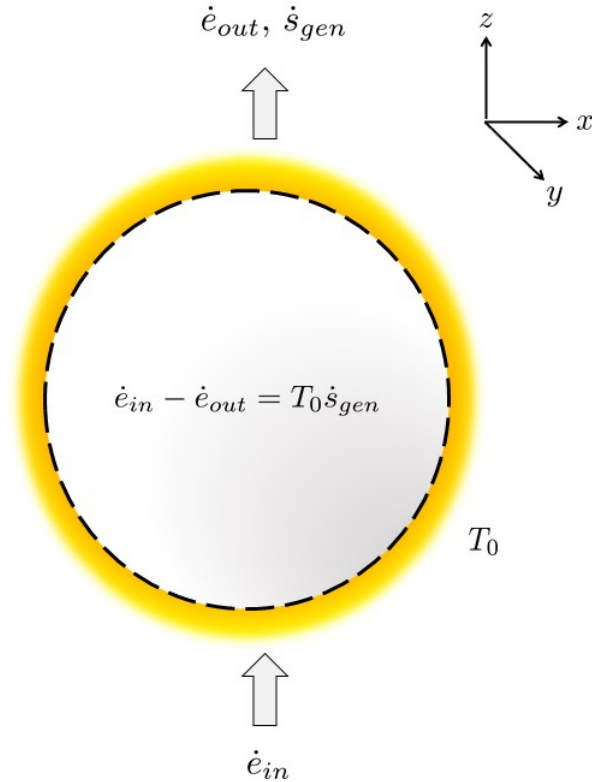


Figure 2.4: Figure shows a typical open thermodynamic system (canonical ensemble), for example, a plate with a thin film of fluid when heated from the bottom along z -axis. The rate of change in the energy (\dot{e}) of the system is balanced by the entropy (\dot{s}_{gen}) generated by it. As the system boundary does not move, the work done by the system is zero. T_0 is the temperature of the surrounding.

an equilibrium state. The Onsager–Machlup function describes the dynamics of a continuous stochastic process by predicting the most probable path between a two metastable states [45, 46]. For a stochastic process, X_t the Onsager–Machlup function is effectively a stochastic Lagrangian function $L(q(t), \dot{q}(t))$ such that,

$$\frac{\rho(|X_t - q_1(t)| \leq \epsilon)}{\rho(|X_t - q_2(t)| \leq \epsilon)} \rightarrow \exp\left(-\int_0^T dt L(q_1, \dot{q}_1) + \int_0^T dt L(q_2, \dot{q}_2)\right) \quad \forall t \in [0, T] \quad (2.6)$$

In the above equation, if q_1 represents one trajectory (smooth and differentiable) and q_2 the other in the generalized phase–space coordinates then the Onsager–Machlup approach allows us to understand the stochastic evolution of the system

macroscopically as the stochastic process, X_t converges to either of the curves at all times for $\epsilon \rightarrow 0$. The Lagrangian contains in itself trajectory-dependent entropy and non-equilibrium work terms. The Onsager–Machlup integral can be extended to understand the nature of non-equilibrium fluctuations and how they dominate the direction of microscopic evolution of the system in the context of entropy production. The second law when proposed in terms of path probabilities assumes the form, $\sigma(\langle q(t) \rangle, \langle \dot{q}(t) \rangle) \geq 0$ where σ denotes the rate of entropy production. The fluctuation theorem embodies in itself the rate of entropy production in order to dictate the directionality of a process in the thermodynamic phase-space [45–47].

$$\frac{\rho_{i \rightarrow j}}{\rho_{j \rightarrow i}} = \exp(\sigma t) \quad (2.7)$$

In the above equation, the ratio of $\rho_{i \rightarrow j}$ to $\rho_{j \rightarrow i}$ is the relative probability that the entropy of a system which is currently away from thermodynamic equilibrium will increase or decrease over a given amount of time if it is driven from a state i to j (i to j denotes forward direction and j to i denotes reverse). In simple terms, if i to j is an entropy producing trajectory then according to Equation 2.7, the probability that the system follows the trajectory that takes it from j to i decreases exponentially as the entropy production along that trajectory is opposite to that dictated by the second law of thermodynamics. Equation 2.7 can be rewritten to include the effects of non-equilibrium work, $W_{i \rightarrow j}$ between a pair of states with free-energy difference ΔF ,

$$\frac{\rho_{i \rightarrow j}}{\rho_{j \rightarrow i}} = \exp[\beta(W_{i \rightarrow j} - \Delta F)] \quad (2.8)$$

Equation 2.8 is also known as the Crook’s fluctuation theorem [42, 48]. Given the general nature of irreversibility in thermodynamics, the free energy difference $\Delta F = F_j - F_i$ between states i and j is connected to the work done, W on the system

through the inequality, $\Delta F \leq W$. The equality holds for the case of quasi-static processes, however Jarzynski showed that no matter how fast the system is driven between the states the ensemble average of the work applied on the system is equal to the free-energy difference between the states, or $\langle \exp(-\beta W) \rangle = \exp(-\Delta F)$ [48, 49]. The second law of thermodynamics is statistical in nature, and the fluctuation theorem allows one to quantitatively predict the possibility that entropy might decrease in an isolated system.

2.2.2 The Case of Local Equilibrium

An approach based on the local equilibrium hypothesis formulates a macroscopic system as a collection of ‘cells’ (domains) in which rules of classical equilibrium thermodynamics are fulfilled to good approximation. This particular viewpoint dates several decades back when Milne, from an astrophysical perspective defined local thermodynamic equilibrium in a local ‘cell’. He proposed the condition that the ‘cell’ will continue to be at local thermodynamic equilibrium as long as it macroscopically absorbs and spontaneously emits radiation as if it were in radiative equilibrium in a cavity at the temperature of the matter of the ‘cell’ [50]. If these ‘cells’ are well-defined, then they allow for transport of matter and energy in between them. This however has to follow under the strict constraint that the flows and currents between the ‘cells’ do not disturb the respective individual local thermodynamic equilibria with respect to the intensive variables. Therefore, one can think of two ‘relaxation times’ that are separated by order of magnitude: the longer relaxation time responsible for the macroscopic evolution of the system and the shorter relaxation time responsible for local equilibration for a single. If these two relaxation times are not well separated, then the classical non-equilibrium thermodynamical concept of local thermodynamic equilibrium loses its meaning [35, 37, 43, 51–54]. If

the notion of local equilibrium holds, one can propose a formalism that describe the equality of certain ratios between flows and forces in thermodynamic systems when driven out-of-equilibrium, also known as the Onsager reciprocal relations [55-57].

$$\vec{J}_\alpha = \sum_{\beta} L_{\alpha\beta} \nabla f_\beta \quad (2.9)$$

Here, \vec{J}_α is a current vector and f_β represent thermodynamic forces. In a simple fluid system that allows diffusion (ρ) and heat transport (u), f_β takes the form $f_u = (1/T)$ and $f_\rho = (-\mu/T)$, and the matrix, $L_{\alpha\beta}$ is the Onsager matrix of transport coefficients. It is a matrix of phenomenological coefficients which is positive semi-definite (in agreement with the second law), and symmetric ($L_{\alpha\beta} = L_{\beta\alpha}$) when time-reversal symmetry is preserved. Onsager's approach makes it possible for us to study the thermodynamics of irreversible processes, such as chemical kinetics, diffusion, conduction of heat etc. by considering linear approximations near equilibrium as it follows from the local equilibrium hypothesis and is closely connected to the principle of detailed balance.

Chapter 3

A Prototypical Complex System

Complex systems are systems that are composed of numerous components or parts which interact with each other in a way that often gives rise to non-trivial emergent properties. The interactions between the parts is non-linear, thus small changes in physical interactions or stimuli can lead to significant changes in response/feedback. The presence of a feedback loop implies that these systems are adaptive and they operate at far-from-equilibrium conditions. Due to the presence of emergent properties and rich collective interaction, these systems are difficult to model as the macroscopic evolution of the system can not be predicted by simply observing the microscopic behavior of its building blocks. Therefore, complex systems science is an inter-disciplinary area of research overarching the natural and exact sciences mostly applicable to the physical, biological and bio-chemical world to data-driven social sciences which involves society, social networks and urban landscape [58–63].

3.1 Self-organization and the Origin of Order

The intersection of complex systems science and non-equilibrium thermodynamics gives rise to a rich field of exploration that encompasses many fascinating systems

and real-life phenomena, all of which contribute to the diversity and complexity in the world around us. The connection between the two is not new, the idea that order can emerge through fluctuations has been long studied by Prigogine [64, 65]. The key aspect about the process of self-organization is that it is a process where external control is absent, the effect of the environment is minimal, and the development of new complex structures takes place primarily in and through the system itself [12, 66, 67]. Due to emergence of order, the entropy of a self-organizing system also decreases. However, in order to maintain its structure it must dissipate or export entropy to its surroundings, as noted by von Foerster and Prigogine [35, 64, 66]. In fact, Prigogine called systems which continuously export entropy in order to maintain their order, dissipative structures. Several model systems that have been actively studied to understand the spontaneous emergence of order include, clustering of bacterial colonies and self-assembly in actomyosin motility assays, phase ordering in liquid crystals, synchronization of Kuramoto oscillators, oscillatory behaviors in reaction-diffusion systems such as the Belousov-Zhabotinsky reaction, or turbulence and pattern formation in thermal-convective systems like the Rayleigh-Bénard convection [15, 16, 68-72]. In an attempt to predict the steady-state dynamics and structures of such systems as they are driven out-of-equilibrium, ideas concerning energy dissipation and entropy production extremal principles have been proposed [34, 41, 73]. Primarily these ideas are based on Onsager's definition of thermodynamics forces, $f \propto \nabla T$ and are applicable in the scenarios where local equilibrium is maintained. Further, as Prigogine and Glansdorff note these principles apply only to systems that can be described by known thermodynamical variables in which dissipative processes dominate iff large deviations from statistical equilibrium are excluded [35, 64]. However, as Kondepudi and many others note, there is no general rule that provides an extremum principle that governs the evolution of a

far-from-equilibrium system to a steady-state [73, 74].

Certain dynamical systems can evolve towards an attractor or a critical point purely through self-organization. This property is known as self-organized criticality, where the macroscopic behavior of the system displays spatio-temporal scale-invariance, a characteristic feature of a phase-transition. Self-organized criticality is observed in systems with strong non-linear interactions while being slowly driven out-of-equilibrium. Bak, Tang and Wiesenfeld using cellular automaton in 1987 showed that complexity is an emergent property which arises from local spontaneous interactions between ‘agents’ [75, 76]. They also noted that several characteristic features of this emergent complexity, such as scale-invariant behavior, fractal geometry, pink ($1/f$) noise and power-laws that could be linked to critical-point phenomena in the larger scheme of things. These observations by Bak *et. al.* paved the way for numerous exciting areas of research in complex systems science over the decades such as, scale-free networks in the context of societal connections and infrastructures (like, transportation, energy distribution, internet etc.), studying the nature of fluctuations in financial markets (econophysics), statistical distribution of earthquake sizes (Gutenberg–Richter law), landscape formation. forest fires, neuronal avalanches in the cerebral cortex, spreading of epidemics (contagions and rumor) etc. [58, 60, 62, 73, 77, 78].

3.2 The Rayleigh–Bénard Convection

The Rayleigh–Bénard convection holds a place of special interest in the scientific community [15, 70, 79]. It is one of the oldest and most widely used canonical examples to study pattern formation and emergent behavior [1, 12, 15, 71]. When a thin film of liquid is heated, the competing forces between viscosity and buoyancy gives

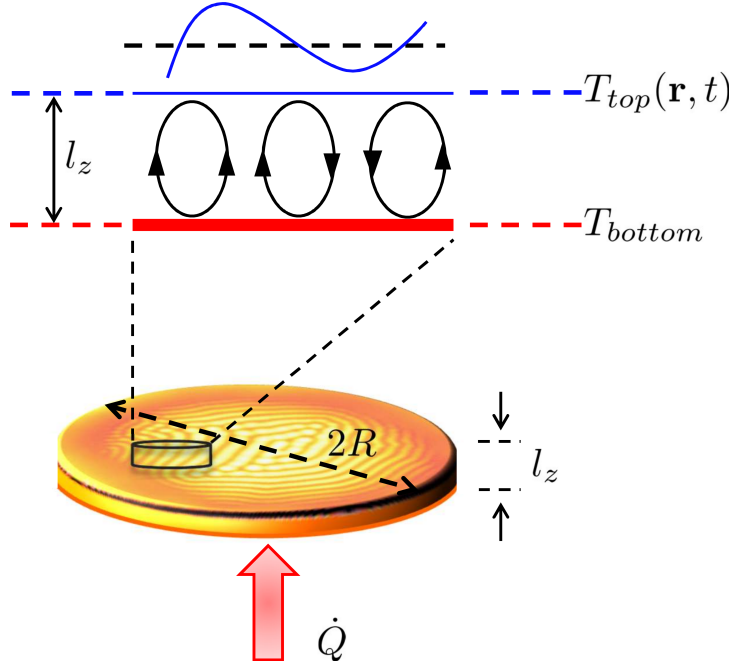


Figure 3.1: Cartoon illustrates the experimental configuration of the current study. The Rayleigh–Bénard system at steady–state is set up by heating a thin film of viscous liquid from the bottom (\dot{Q}). The temperature difference between T_{bottom} and T_{top} gives rise to convection rolls. While at steady–state, T_{bottom} is constant, real–time thermal imaging of the top layer is performed to extract the spatial and temporal distribution of T_{top} . The line cut of the thermal profile $T_{top}(\mathbf{r}, t)$ is also shown [6].

rise to convective instabilities. This convective instability creates a spatio–temporal non–uniform thermal distribution on the surface of the fluid film (see Figure 3.1). The advantage of this system lies in its simplicity, wherein a dimensionless quantity, the Rayleigh number (Ra), determines the onset of convective cell patterns,

$$Ra = \frac{g\beta l_z^3}{\nu\alpha}(T_{bottom} - T_{top}) \quad (3.1)$$

In the above equation, l_z denotes fluid film thickness, ν kinematic viscosity, α thermal diffusivity, β compressibility, and g acceleration due to gravity. The critical Rayleigh number of 1708 marks the onset of convection for a no–slip boundary

condition was obtained by Jeffreys in 1929 [15, 71, 80]. Under the approximations of an ideal incompressible fluid that is thermally driven one can write the following set of equations also known as the Boussinesq approximations,

$$\begin{aligned} \frac{\partial \rho}{\partial t} + \nabla \cdot (\rho \vec{u}) &= 0 \\ \frac{\partial \vec{u}}{\partial t} + (\vec{u} \cdot \nabla) \vec{u} &= -\frac{1}{\rho} \nabla p + \nu \nabla \cdot (\nabla \cdot \vec{u}) - g\beta\Delta T \\ \frac{\partial T}{\partial t} + \vec{u} \cdot \nabla T &= \alpha \nabla^2 T + \frac{\vec{J}}{\rho c_P} \end{aligned} \quad (3.2)$$

For a packet of fluid with local convective velocity, \vec{u} incompressibility implies, $\nabla \cdot \vec{u} = 0$; the density is assumed to vary linearly with temperature, $\rho = \rho_0(1 - \beta\Delta T)$, and the specific heat of the fluid is denoted by c_P .

3.3 Perspectives from Fluid Mechanics

Due to its conceptual richness and an easy experimental methodology, the Rayleigh–Bénard convection remains one of the most actively and extensively studied physical systems. The dynamics of a Rayleigh–Bénard convection system connects fundamental ideas from both thermodynamics and fluid mechanics [15, 69, 71, 79, 81, 82]. It is in fact one of the simplest complex systems’ that can be easily recreated in a laboratory with minimal efforts. One can find numerous studies on the empirical relationships between the various dimensionless numbers (specially, Nusselt number (Nu), Reynolds number (Re), Prandtl number (Pr) and Rayleigh number (Ra)) under conditions of laminar and turbulent flows [83, 84]. The process of heat transfer specially in a turbulent convection over the years have resulted in the development of many state-of-the-art temperature measurement techniques which were tested on the Rayleigh–Bénard convection system [85–87]. In this relation, numer-

ous boundary–layer studies have been carried out to estimate the effect of geometry on the efficiency of convective heat transfer and on the role of plumes. Similarly, numerous studies on calorimetric measurements of thermal fluctuations under turbulent flow conditions have played an important role in our general understanding in the process of convection cell formation [65, 88–93].

Furthermore, the onset of convection cell patterns in relation to thermal and hydrodynamic boundary layer models is an active area of interest in the fluid mechanics community, especially in understanding the phenomena of turbulence. Turbulence, although quite ubiquitous in nature, still remains one of the many unsolved problems in physics today. Not only as a tabletop experiment, but also through numerical simulations, the Rayleigh–Bénard convection cell system serves as a very convenient prototypical model that has provided insights into the physics and hydrodynamics of turbulence. Noteworthy among them are studies on the effects of rotation and magnetic fields on Rayleigh–Bénard convection cells, turbulent convection at very high Rayleigh numbers with cryogenic *He* gas as the working fluid to probe velocity and thermal statistics, and measurements of the mean temperature and variance profile as a function of boundary layer thickness [81, 94–97]. Although, the current state of the art experimental setups, data logging techniques, numerical and mechanistic simulations have provided numerous critical insights about the fluid mechanical aspects, a lot of the thermodynamical interpretations still remain unresolved [84, 86, 89, 90, 93, 95, 98, 99].

3.4 Experimental Methodology

In this work, we primarily focus on the non–turbulent Rayleigh–Bénard convection as a prototype for a far–from–equilibrium system that exhibits emergent order. It

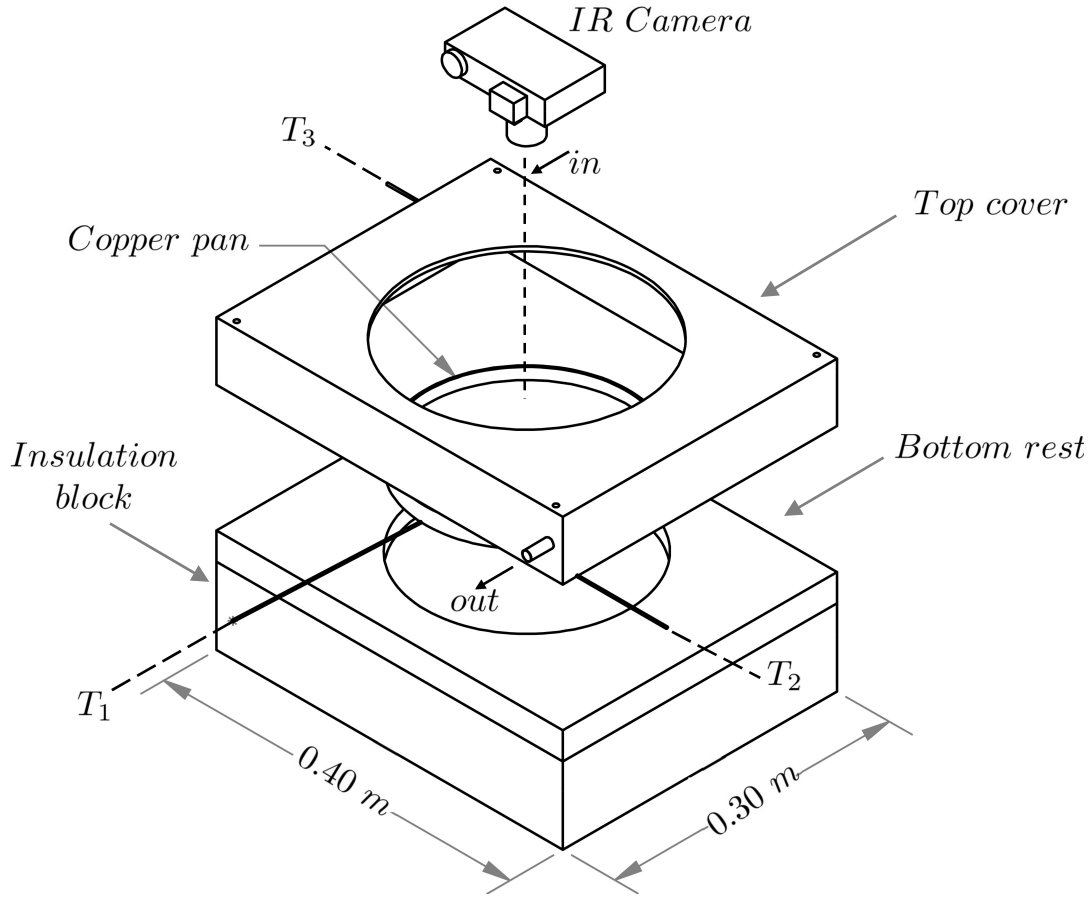


Figure 3.2: Figure illustrates the experimental setup with the copper pan ($2R = 0.225\text{ m}$), the three thermocouples (T_1, T_2, T_3), inlet and outlet ducts for the forced convective heat transfer, and the infra-red camera for real-time thermal imaging. The inlet and the outlet ducts are present on the top cover and the copper pan sits on a wooden bottom rest and a polyurethane foam foundation which acts as an insulator [6].

should be noted that our study of the Rayleigh-Bénard convection is motivated *solely* from a thermodynamic point of view and not from a fluid mechanics perspective. To elaborate, we focus on broad questions such as, can multiple local equilibrium states coexist in an otherwise far-from-equilibrium system, or how the statistical mechanics of a far-from-equilibrium system differs from that of a system at equilibrium? What are the limitations of the local equilibrium hypothesis, or under what conditions do thermal gradients in a system dominate and allow for

the spontaneous emergence of ordered structures [4, 15, 22, 37, 98–101]? While we experimentally explore the far-from-equilibrium behavior of temperature, these results sheds light on the fundamental questions mentioned above. These questions, answers to which are yet unknown or inconclusive, are important for the broad scientific community, but are also of significant general interest.

In Figure 3.2 and Figure 3.3 we illustrate the experimental setup in detail. The top cover is made up of wood and has inlet and outlet ducts for forced convective heat transfer. The two thermocouples T_2 and T_3 measure the temperature of the incoming and outgoing gas respectively. The bottom rest, also made up of wood has a cavity with a recess on which the copper pan sits snugly. The wooden base rests on top of a block of polyurethane foam. A resistance heater is attached to the base of the copper pan and the thermocouple, T_1 (also connected to the base of the copper pan) measures the bottom temperature of the pan, T_{bottom} (see Figure 3.1). An infra-red camera (with a precision $\sim 10^{-3}K$), placed concentrically above the copper pan captures the real-time thermal images from a height ($\geq 0.7 m$). Each thermal image has its own temperature scale. In order to calibrate the infra-red camera with the base thermocouple (T_1), the empty copper pan is heated and the temperature of five randomly chosen points on the copper pan are recorded at different power settings of the resistance heater at steady-state. The thermocouple temperature recorded by T_1 is then compared with the infra-red camera recorded temperature for the five spots. The thermocouple data can be viewed in the NI Signal Express software while the infra-red camera data is viewed in the FLIR software. The FLIR software allows remote accessibility like, real-time display, region/point selection and spatial statistics. In Figure 3.4, we present the calibration curves for the five spots comparing the infra-red camera-recorded temperature with the base thermocouple temperature. The calibration error thus estimated is used to adjust

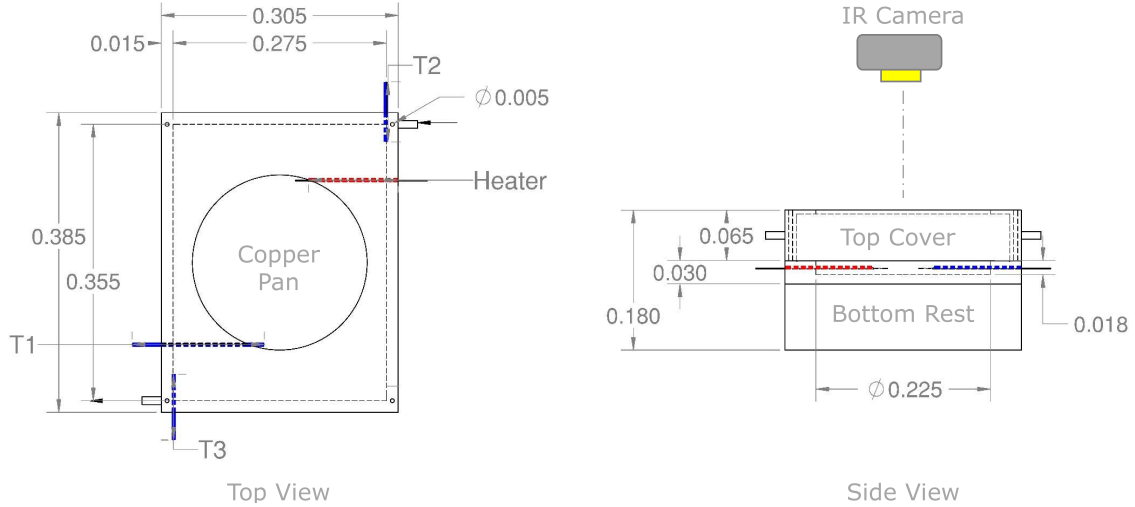


Figure 3.3: Figure shows Rayleigh–Bénard Convection setup: Top View (left) and Side View (right). All dimensions are in meters. The three thermocouples used to record the temperature of the pan, the inlet and the outlet of the heat–exchanger are denoted in blue (T_1 , T_2 and T_3). The heater attached to the bottom of the copper pan is denoted in red. The thermal images are recorded from the top using an infra–red camera [7].

the infra–red camera temperature scale in accordance with the base thermocouple. A thin layer of silicone oil ($l_z = 4.7 - 5.0 \text{ mm}$) is heated in the copper pan whose average diameter is 0.225 m . Due to small varying thickness of the base of the copper pan, the film thickness and the surface temperature of the top is averaged over the entire exposed area. The system is heated by regulating the power input through the heater. The resistance of the electric heater is $37.5 \pm 0.5 \Omega$. At a specific power, the system is let to evolve over time such that the mean bulk–temperature stops fluctuating. Once the system reaches a steady–state (after approximately two hours), the mean temperature of the top surface is denoted by T_{top} (see Figure 3.1).

The thermal and material properties of the oil is outlined in Table 3.1. A sample of the raw images that were recorded by the infra red–camera are shown in Figures 3.5a and 3.5b. These raw images (I), in grey–scale are then converted into a matrix of temperature, where each entry of the matrix element (I_{ij}) corresponds

Table 3.1: Table outlines thermal and material properties of the silicone oil sample that was used to perform the current study [10]. The units for viscosity (ν) is cSt , for density (ρ) kg/m^3 , for thermal conductivity (k) $W/m - K$, for specific heat ($c_{p_{oil}}$) ($J/kg - K$), for thermal diffusivity (α) m^2/s , and for thermal compressibility (β_T) m^2/N .

<i>Viscosity</i>	<i>Density</i>	<i>Conductivity</i>	<i>Sp. Heat</i>	<i>Diffusivity</i>	<i>Compressibility</i>
ν	ρ	k	$c_{p_{oil}}$	α	β_T
150	970	0.16	1500	1.099×10^{-7}	9.5×10^{-4}

to the temperature of each pixel (T_{ij}) on the image. The infra-red camera detects radiation emitted from an object and converts it into bits. Thus, every pixel has an allocated bit value between 0 and 255. The bit value determines the intensity of the pixel with 0 being the ‘coldest’ pixel in the image and 255 being the most intense or the ‘hottest’. The FLIR T62101, used in this study has a resolution of 320×240

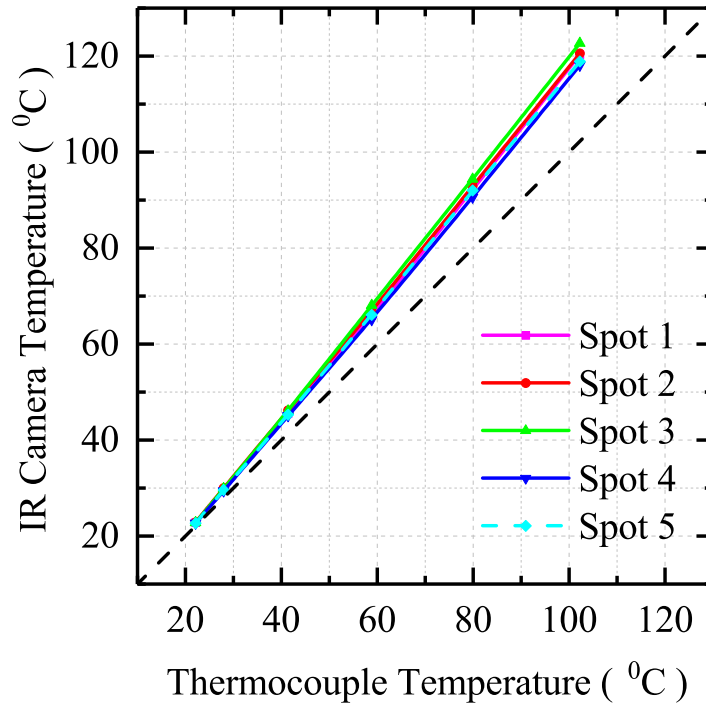


Figure 3.4: Figure shows the steady-state relationship between the infra-red camera recorded temperature and the base thermocouple temperature at different power settings for the five randomly chosen spots on the empty copper pan [7].

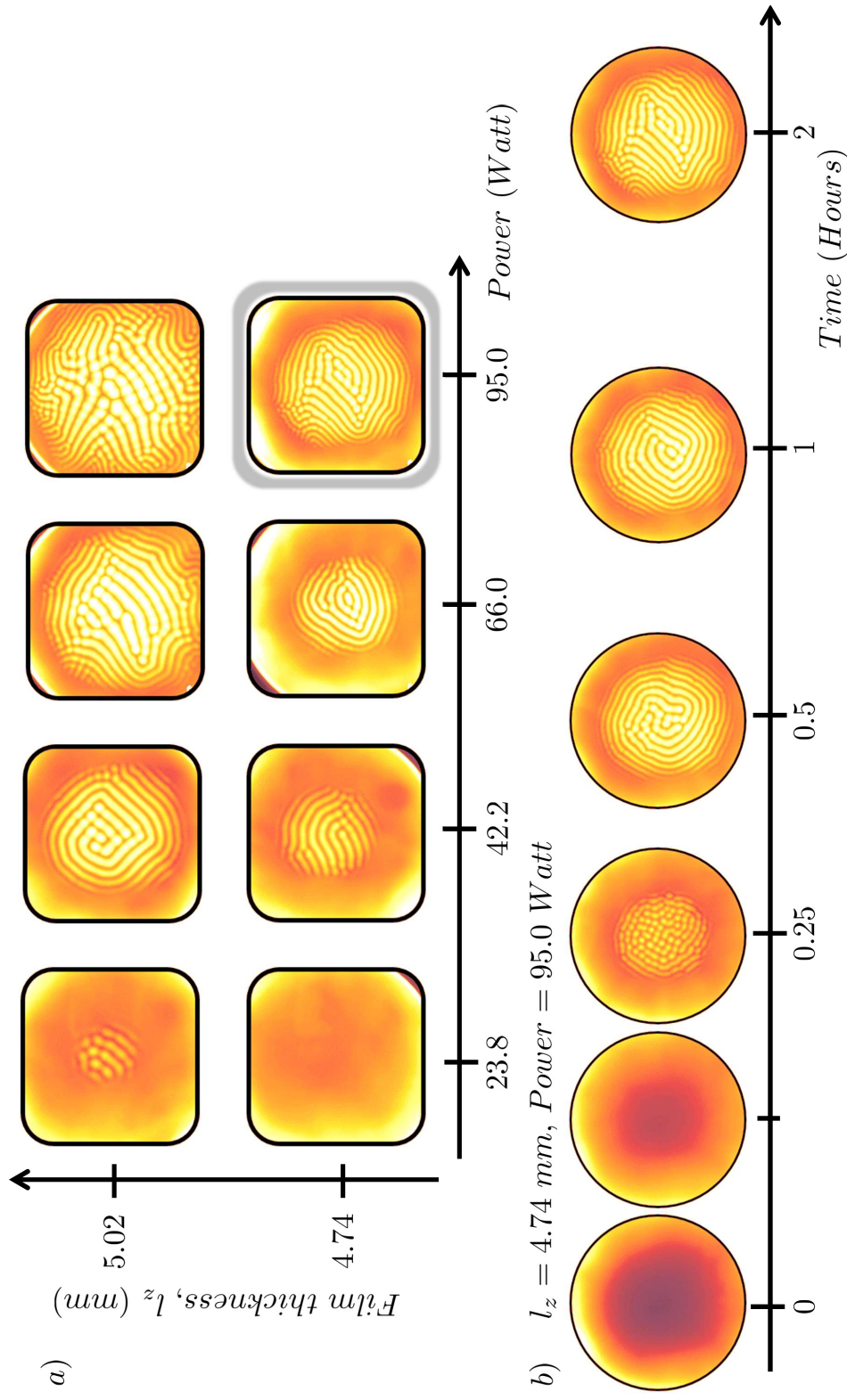


Figure 3.5: a) Figure shows steady-state thermal images recorded for two thickness, $l_z = 4.74$ mm and 5.02 mm at various powers. b) Figure shows the time-evolution of the $l_z = 4.74$ mm at 95.0 W over a period of two hours. Note that the shown images are logarithmically placed in time [6].

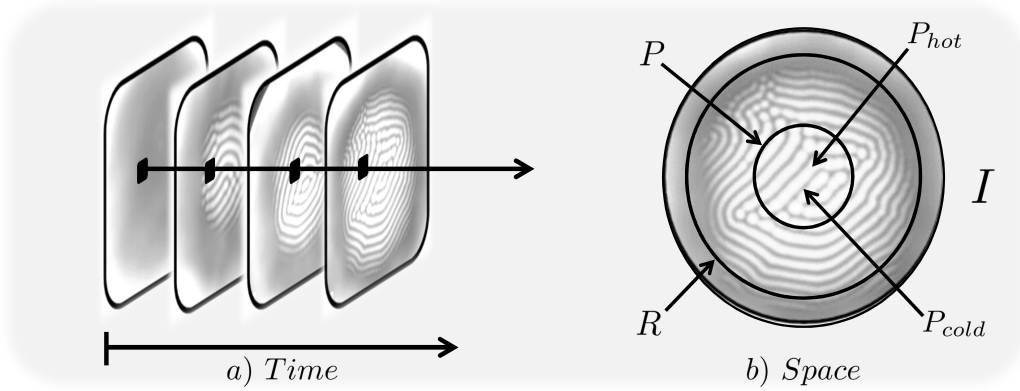


Figure 3.6: a) Figure illustrates the temporal analysis of an arbitrary region of interest on the images as a function time as the system evolves from room temperature equilibrium to an out-of-equilibrium steady-state. b) Figure shows the regions of interest for the spatial analysis on the steady-state image of a Rayleigh-Bénard convection. The complete image is denoted by I , the annular region without any structures by R , the circle at the center by P , the upward (bright spots) and downward plumes (dark spots) by P_{hot} and P_{cold} respectively [6, 7].

pixels (= 76,800 pixels) with a sensitivity less than 0.045°C . Therefore, every image (I) is a $M \times N$ 2D array of 320×240 elements with 256 bit values distributed in between them. Each of these bit values can be converted to respective temperature values through a linear interpolation as shown in the equation below,

$$\text{Temp } (^{\circ}\text{C}) = \frac{\text{Max Temp } (^{\circ}\text{C}) - \text{Min Temp } (^{\circ}\text{C})}{255 - 0} \times \text{bit} + \text{Min Temp } (^{\circ}\text{C}) \quad (3.3)$$

These images are then statistically analyzed both spatially and temporally. In Figure 3.6 we depict the two types of analysis that are performed on these images. In Figure 3.6a, we perform a temporal analysis of the images as the system evolves to a steady-state. A region of interest at the center is chosen and is then followed in time. The statistics that are obtained, are then analyzed as a function of time or are averaged over time. In Figure 3.6b, we spatially analyze the steady-state images as obtained from the thermal camera. The analysis of this type gives us insights about the spatial aspects of the system once steady-state has been achieved and

structures have emerged. The two primary regions of interest in this type of analysis are the patterned region, P and the non-patterned region (or the ring region) R . Within the patterned region, P , the brighter spots represent upward plumes and are denoted by P_{hot} , while the darker spots represent downward plumes, and are denoted by P_{cold} [6, 7].

3.5 Results and Discussion

In this section, we discuss the key results from our experimental study on the non-turbulent Rayleigh-Bénard system at steady-state both in space and time domain.

3.5.1 Temporal Analysis

In Figure 3.7 we plot the mean of the top temperature (left axis) and its standard deviation (right axis) as a function of time when the silicone oil sample is heated. The sample, initially at room temperature is driven out-of-equilibrium by the application of a constant heating power. Once the system reaches a steady-state, the heating power is switched off and system gradually relaxes back to room temperature. The top temperature mean and standard deviation as a function of time for the cooling process is plotted in Figure 3.8. The mean temperature of an arbitrary region of interest on the image, $\langle T \rangle = \frac{1}{N} \sum_{i,j \in I} T_{ij}$ and the standard deviation, $\sigma_T = \sqrt{\frac{\sum_{i,j \in I} (T_{ij} - \langle T \rangle)^2}{N-1}}$ are calculated from the image matrix (I_{ij}). We observe from Figures 3.7 and 3.8 that the mean temperature follows a typical heat-conduction trend for heating as the system achieves ostensibly a new high-temperature equilibrium (non-equilibrium steady-state) as well as on cooling toward the original room temperature equilibrium state. The maximum temperature reached by each sample at steady-state increases as expected with increasing power based on the

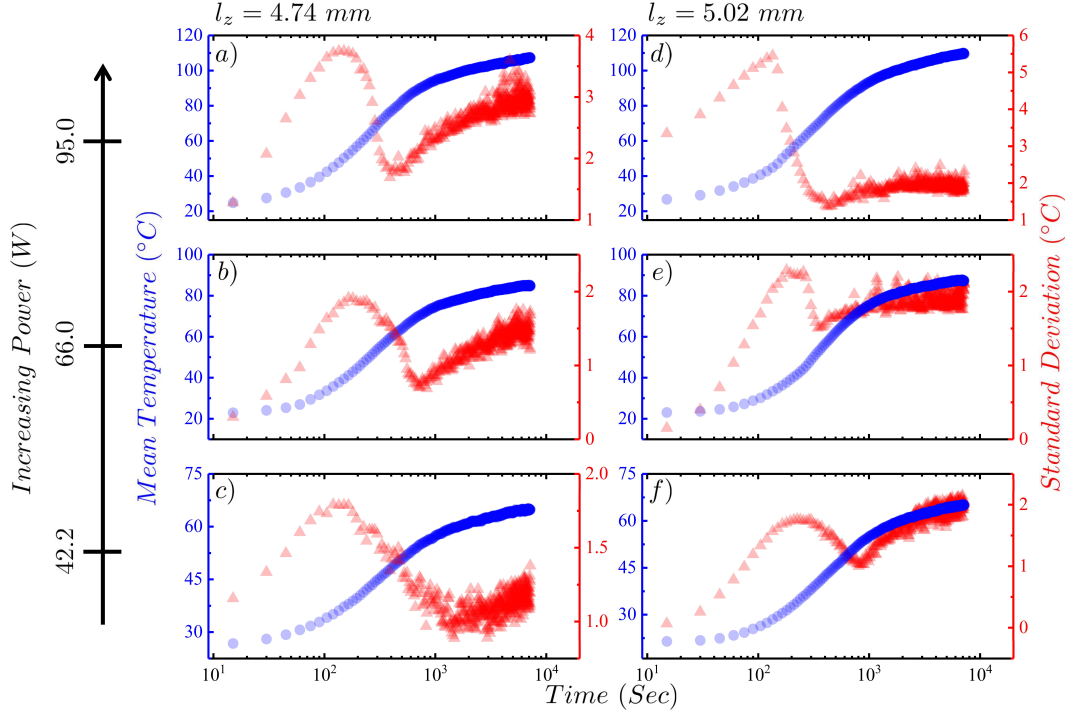


Figure 3.7: Figure shows on a semi-log scale the temperature mean and standard deviation as a function of time of the top of the silicone oil film as it responds to the applied heating power until steady-state is reached for various values of input power. The left axis corresponds to the temperature mean in degrees Celsius (solid blue circles) and the right axis corresponds to the standard deviation (solid red triangles). Plots *a*, *c*, *e* show heating profiles for a film thickness of $l_z = 4.74 \text{ mm}$, and plots *b*, *d*, *f* for $l_z = 5.02 \text{ mm}$. Note that the applied heating power in Watts are labeled by the far left y -axis [6].

heat capacity for each film [6]. The plots for the standard deviation in temperature as a function of time, however, show a markedly different trend during both heating and cooling processes as can be seen from Figures 3.7 and 3.8, respectively. The standard deviation, a measure of the distribution width and is related to the temperature fluctuations in the system, generally increases with increasing temperature. Although an increasing trend in standard deviation as a function of time is observed on heating as expected since the temperature is increasing, this trend is broken at a point in time when the first hints of convection cells appear $t \approx 200$ seconds, where σ_T begins to decrease. This decrease in σ_T continues as the convection cells

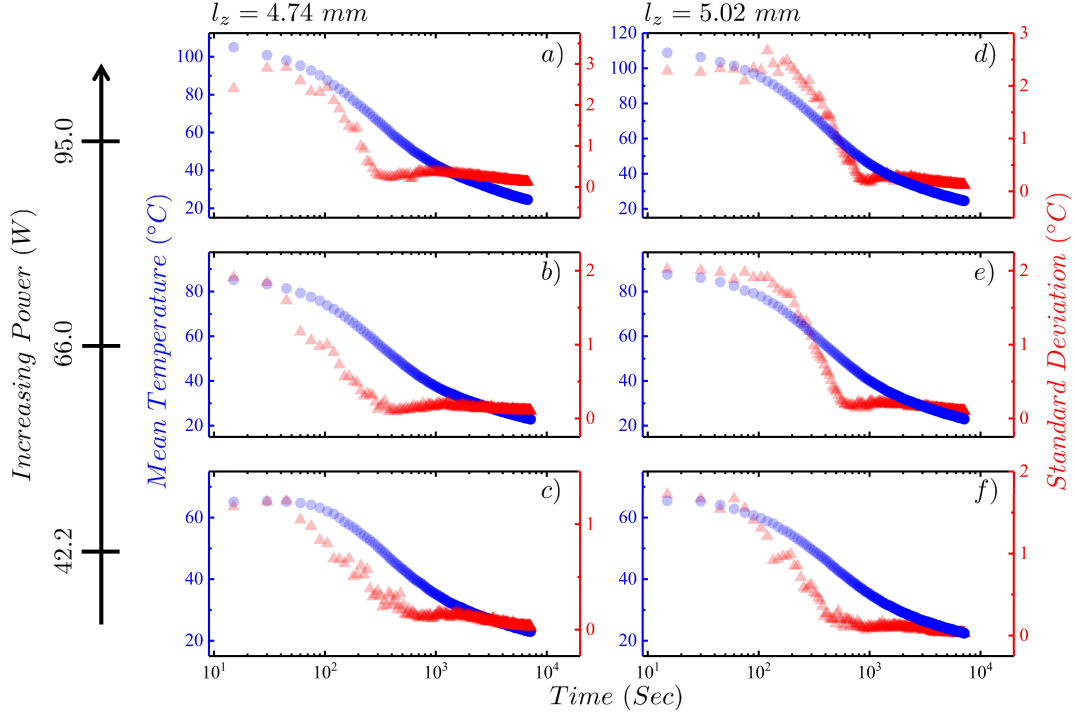


Figure 3.8: Figure shows on a semi-log scale the temperature mean and standard deviation as a function of time of the top surface of the silicone oil film as it relaxes to room temperature after the applied heating power is removed. The left axis corresponds to the temperature mean in degrees Celsius (solid blue circles) and the right axis corresponds to the standard deviation (solid red triangles). Plots *a*, *c*, *e* show cooling profiles for the film thickness of $l_z = 4.74 \text{ mm}$, and plots *b*, *d*, *f* for $l_z = 5.02 \text{ mm}$. Note that the applied heating power in Watts are labeled by the far left y -axis [6].

grow until they reach their maximum extent over the film, which is not the entire film area due to the side heating produced by the cu walls. Once the convection cell pattern has stabilized, σ_T reaches a minimum at $t \approx 900$ seconds after which it begins to increase again and only flattens as the mean temperature stabilizes. For cooling, after the heating power is removed, both the $\langle T \rangle$ and σ_T begin to decrease with σ_T decreasing more rapidly as time progresses until the last vestiges of any cell pattern disappears after which the decrease in σ_T abruptly slows and flattens as $\langle T \rangle$ returns to room temperature. Over regions of the film where the temperature appears uniform, σ_T is dominated by the spatial thermal fluctuations of the film

but when convection cells are apparent σ_T contains additional contributions due to thermal gradients across the film [6].

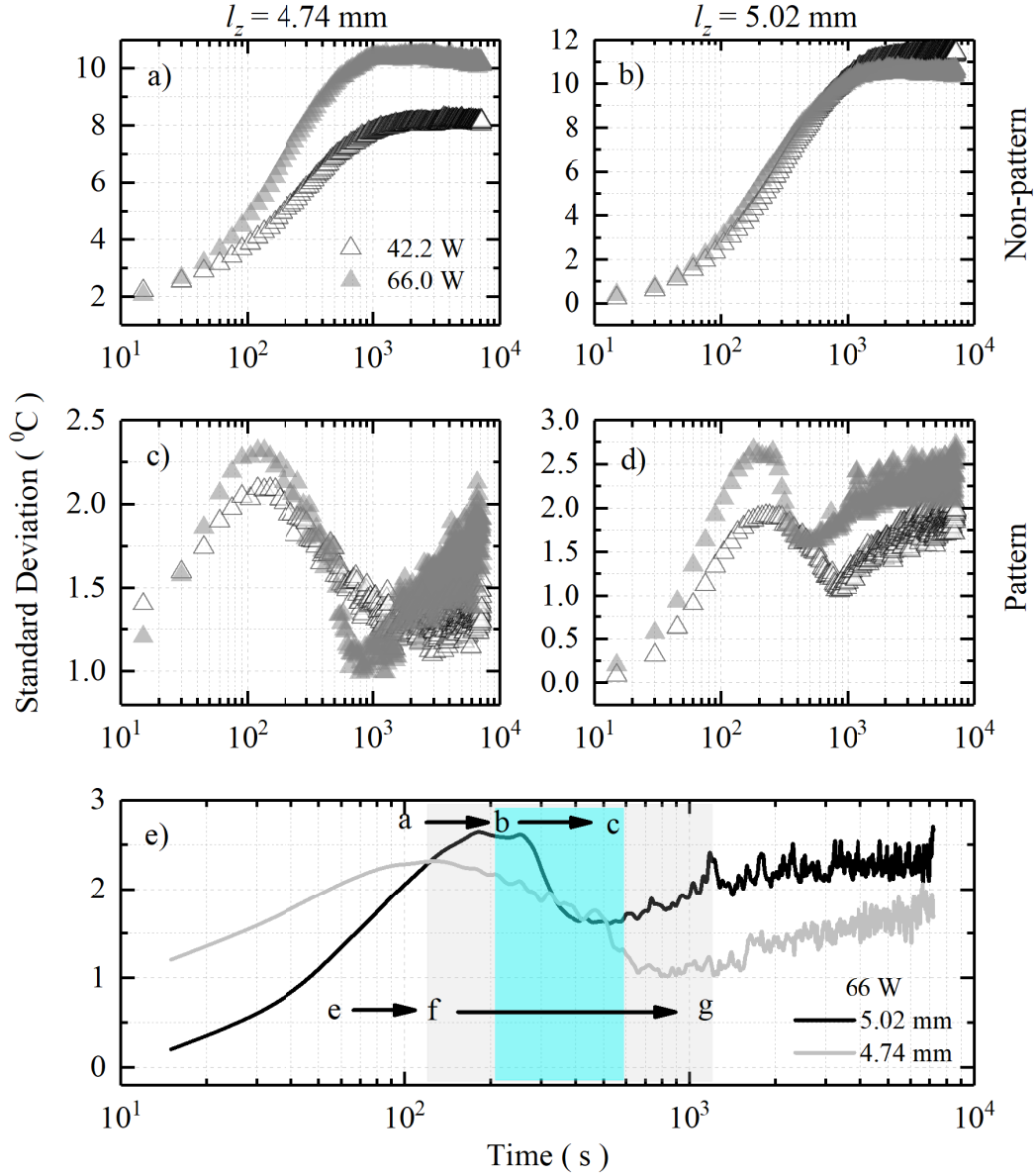


Figure 3.9: a), b) Figure shows the functional relationship between the standard deviation of the temperature for the non-pattern region with time as the Rayleigh-Bénard system evolves from a room temperature equilibrium to an out-of-equilibrium steady-state for $l_z = 4.74$ mm and 5.02 mm at 42.2 W and 66 W. In c) and d) the data is shown for the pattern region. In e) a comparison is done between the two thickness at 66 W with the time windows identified: cyan for 5.02 mm and light grey for 4.74 mm [7].

In Figure 3.9, we take our statistical analysis a step further by plotting the standard deviation of the temperature as a function of time by isolating the pattern and non-pattern regions for the two thicknesses at 42.2 W and 66 W . We can see contrasting trends between Figure 3.9a and 3.9b. In Figure 3.9a and 3.9b, the standard deviation increases with time till saturation as the system reaches a steady-state. Whereas, in the case of the pattern region in Figure 3.9c and 3.9d, the standard deviation first shows a decline when the pattern starts to form but is not yet visible, followed by a dip at the point a stable visible pattern starts emerging (similar to Figure 3.7). We further illustrate this in Figure 3.9e, where we compare the temporal evolution of the standard deviation of the temperature for the two thicknesses at 66 W . The shaded boxes in the plot identify the time windows when the standard deviation starts to decline and then increasing again. With increasing power we can observe that the standard deviation of the temperature grows in time and the time window for the standard deviation shortens as $Ra \sim \Delta T$. For a thicker fluid film the time window is observed to be shorter as, $Ra \sim l^3$. Thus, a critical local Rayleigh number is achieved faster. One can also identify the beginning and the ending of the time window with the thermal image snapshot labels from Figure 3.9. The window in cyan identifies the transition from $b \rightarrow c$ for 5.02 mm , whereas the window in light grey identifies the transition from $f \rightarrow g$ for 4.74 mm . The images a and e are equilibrium snapshots (at $t = 0$) taken for both the thicknesses respectively [7].

Figure 3.10 presents the time-averaged scaled thermal variation at steady-state over a region of the film. This scaled thermal variation is calculated by the determining the difference between the temperature of a given pixel from $\langle T \rangle$ of the region of interest then scaled by the same mean, $\delta T^* = \frac{T_{ij} - \langle T \rangle}{\langle T \rangle}$. Once at steady-state, a series of images (a movie) is recorded at 30 frames/sec for 15 minutes. A fixed region

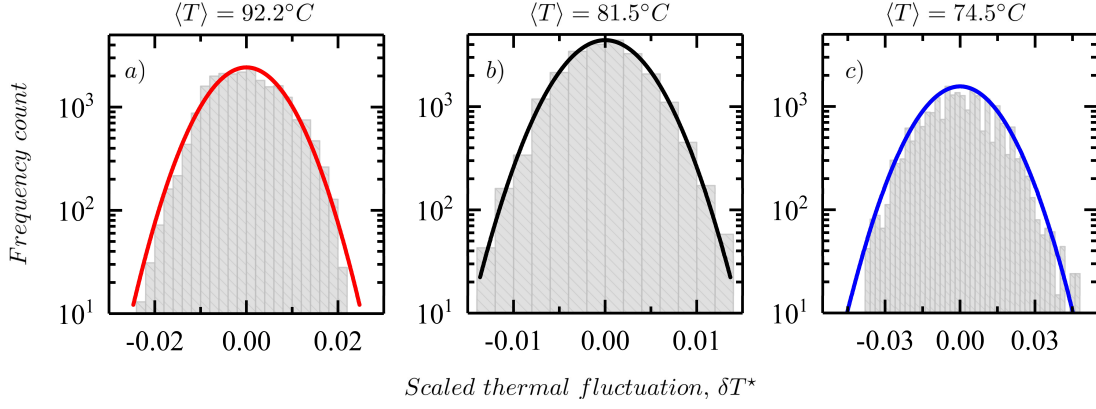


Figure 3.10: Figure shows the histograms for the scaled-thermal fluctuations averaged over time after the system has reached a steady-state on a semi-logarithmic scale. The panels a) denote the hot regions (P_{hot}), b) the entire region (P), and c) the cold regions (P_{cold}). The mean temperature, $\langle T \rangle$ (in $^{\circ}C$) of the various regions of interest are also denoted. The histograms are fitted with normal distribution functions all centered at zero [6].

of interest is then identified on the image, either one near the edge exhibiting no pattern or one over a hot or cold part of a convection cell, and δT^* is then averaged over 27,000 frames,

$$\delta T^* = \frac{1}{T} \int_0^T \delta T^*(t) dt \quad (3.4)$$

In Figure 3.10a and 3.10c, the time-averaged distributions for the upward (hot) and downward (cold) plumes denoted by, P_{hot} and P_{cold} respectively, are shown. Figure 3.10b presents the time-averaged distribution for the entire patterned region, P . Each of these three histograms are fitted with a normal distribution function centered at zero. The plots in Figure 3.10 are shown in a semi-logarithmic scale to highlight the behavior in the tails where deviations from the fit would be most apparent. For the histogram statistics on the hot regions in Figure 3.10a, the normal curve describes the data very well over the entire range. However, in the cold regions shown in Figure 3.10c, the normal curve does not reproduce the data, especially in the tails, as well and would suggest the possible presence of higher moments to the

distribution. The combined distribution is dominated by the hot regions and so does not reveal the deviations from normal as well. As the chosen hot and cold regions do not contain the pattern, they are not influenced by the thermal gradients across a cell therefore, the statistics therein measure pure thermal fluctuations; while the distribution over the whole pattern contains both gradients and fluctuations. Normal distributions imply that the fluctuations are essentially random in nature and that this indicates equilibrium-type fluctuations, which supports the notion that the individual hot and cool regions are each equilibrium-like domains but at different mean temperatures that *coexist* in a steady-state.

3.5.2 Spatial Analysis

In Figure 3.11, the space-averaged scaled-thermal variation density from the steady-state images are plotted. A steady-state image is chosen in which structures are clearly visible. The two regions of interest, the patterned region (P) and the annular non-patterned region (R) are chosen. A measure, μ is defined over the collection of pixel-points in P and R such that,

$$\delta T^* = \frac{1}{\mu(P)} \int_{\mu} \delta T^*(P). \quad (3.5)$$

The left panels (a and c) in Figure 3.11, report the histograms and the kernel density estimates for the patterned region for the two thicknesses. The salient feature of the plots is the presence of a bimodal behavior. For the same sample under same physical conditions, when a non-patterned region is chosen (right panels, b and d), the histograms of the fluctuations are well fitted by a Gaussian distribution function. This bimodal result of the patterned region has two important aspects: i) the ergodicity is clearly broken, and ii) the ergodicity is broken *spatially* (or the

spatially-symmetry is broken). It is interesting to note that a similar bimodal distribution of local thermal fluctuations was reported earlier, but in a very different context [82, 89]. In the convective cell region (P), the distribution contains both gradient and fluctuation contributions to the temperature spatial variation while the hot or cool or ring regions (i.e. chosen regions without a pattern) have a normal distribution. Of course, the emergence of these modes can be attributed to the steady-state patterns of convective instabilities arising due to the upward and downward drafts [15, 17, 71]. As seen in Figure 3.11b and 3.11d, the peaks in the distribution are equidistant from the origin with a local minima close to the origin [6, 7]. It is clear by now that the thermal profile of the top layer of the fluid film is non-uniform. In order to visualize the modulation in the temperature as a function of distance several line cuts are performed on the thermal images. These line cuts are constructed from the image matrix by choosing 1D arrays of row/column data. In Figure 3.12, we plot spatially averaged thermal profiles along six horizontal line cuts aligned parallel to each other. As expected, the mean temperature in Figure 3.12a is greater than the mean temperature in 3.12b. The modulation in the thermal profiles describe the thermal-field heterogeneity. The flatness of the thermal profile allows us to identify spatial correlation lengths of thermal fluctuations in the system. On comparing Figure 3.12a and 3.12b, it can be observed that at higher power (66 W) the thermal profiles tend to be more uniform over longer length-scales than at lower power (42.2 W). There are two reasons for this observation. One, at lower power the pattern occupies a smaller area about the center while the majority of the peripheral region being ‘cooler’ thus implying more thermal heterogeneity as one approaches the periphery from the center, and two, at lower power the emergent patterns are not fully developed yet and hence randomly oriented. Thus, the modulation is uneven and hence chaotic. At higher power, the emergent patterns are fully developed

and exhibit a closed packing thus being more homogeneous. In order to reconstruct the complete geometry of the thermal field we need to extract the thermal profile and integrate over the whole region. In order to execute this, thermal profiles of normalized integrated intensities around concentric circles are plotted as a function of distance from a point in the image. This point of reference is defined by the center of the rectangle that bounds the region of interest. The position of this point

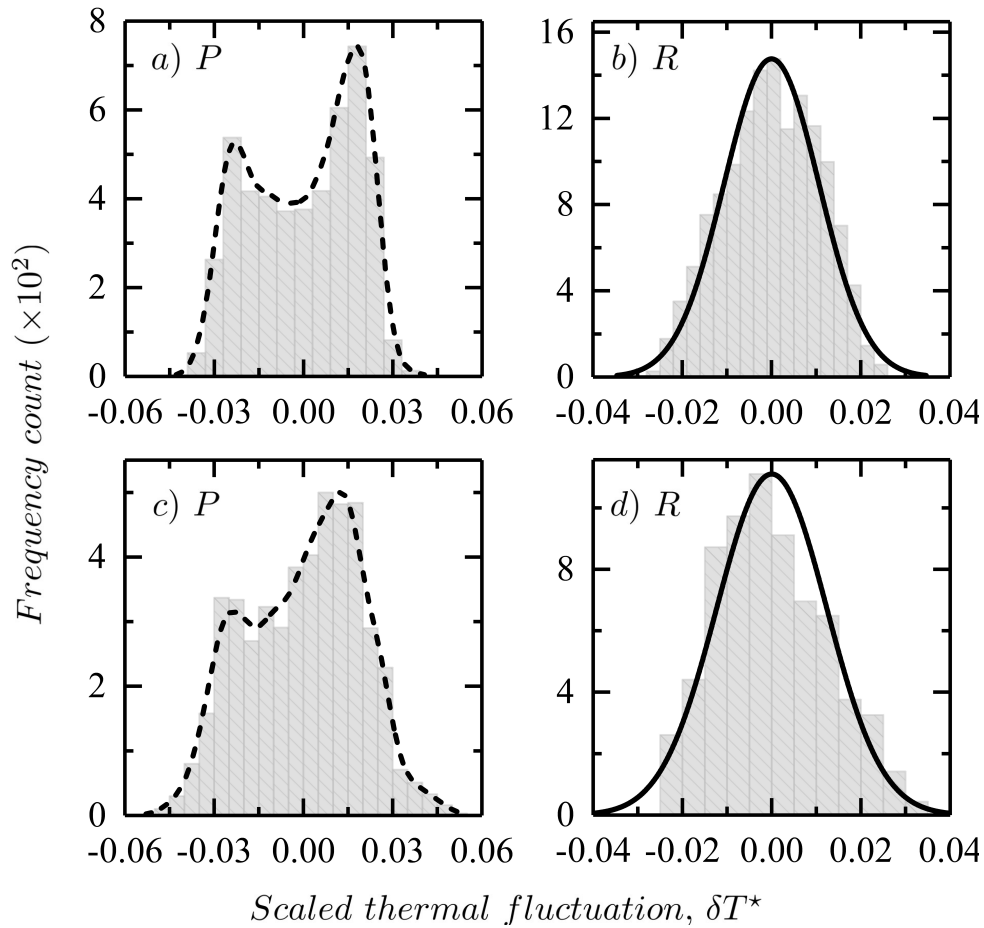


Figure 3.11: Figure shows the histograms for the scaled-thermal fluctuations averaged in space after the system has reached a steady-state. The top panel shows the distributions for $l_z = 4.74$ mm and the bottom panel for $l_z = 5.02$ mm. Panels a) and c) plots the scaled-fluctuation frequency counts for the patterned region, P with a kernel density estimate (dashed). Panels b) and d) plot the scaled-fluctuation frequency counts for the non-patterned annular region, R with a normal curve fit centered at zero (solid) [6].

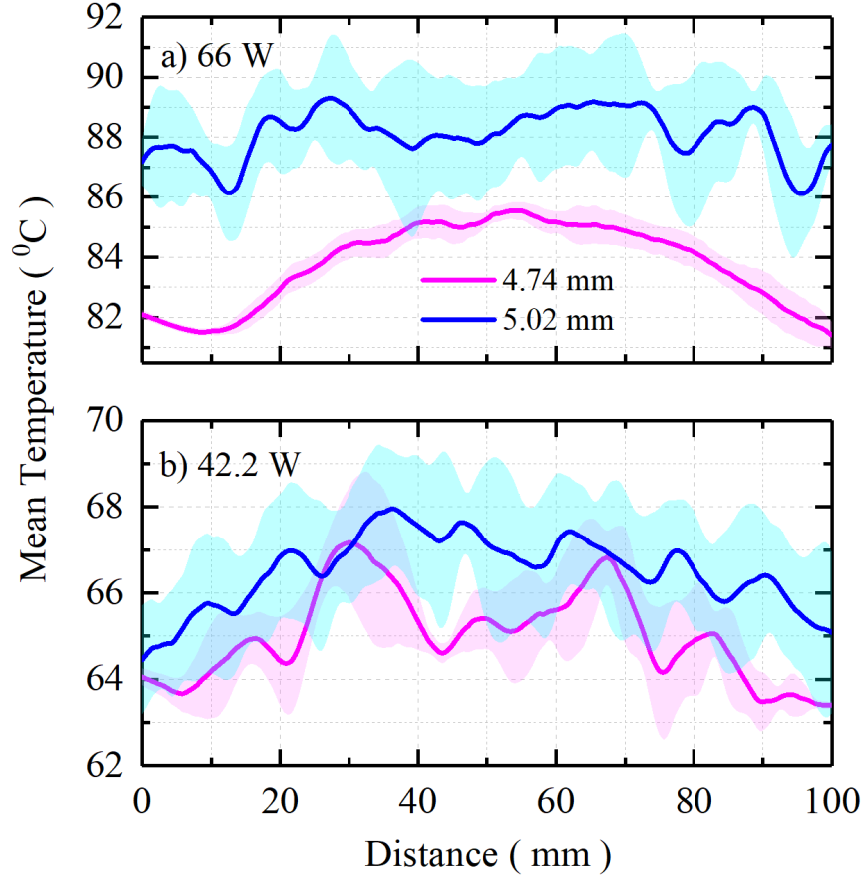


Figure 3.12: a) Figure shows the mean thermal profiles of six spatially averaged horizontal lines for $L_z = 5.02 \text{ mm}$ (blue) and 4.74 mm (magenta) at 66 W . b) Figure shows the mean thermal profiles of six spatially averaged horizontal lines for $L_z = 5.02 \text{ mm}$ (blue) and 4.74 mm (magenta) at 42.2 W . The shaded bands about the mean thermal profiles represent the standard deviation [7].

can be modified by user defined commands. The temperature at any given distance from this point represents the sum of the pixel values around a circle, whose radius is the distance from the point. The integrated intensity is then divided by the number of pixels in the circle thus yielding normalized density values. This profile is plotted as a function of distance by defining a starting and an integration angle to perform a radial averaging. The radial averaging allows us to identify the distance between subsequent maxima and minima on the thermal field [6–8]. However, to extract meaningful length–scales from the entire thermal profile we need a more

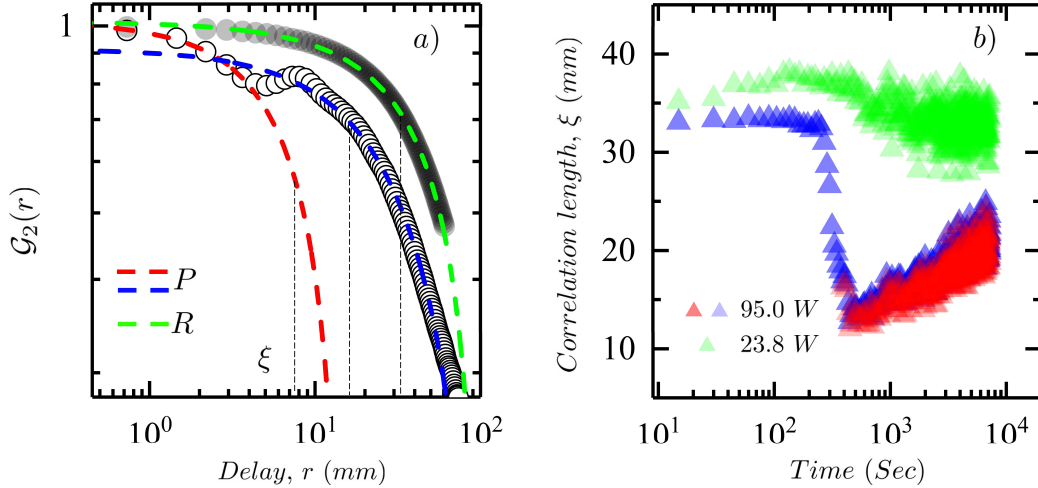


Figure 3.13: a) Figure shows the two–point autocorrelation function, \mathcal{G}_2 as function of distance, r with exponential fits, $\mathcal{G}_2(r) \sim \exp(-\frac{r}{\xi})$ where ξ is the correlation length on a log–log scale. The data shown in grey filled–circles with a single fit is for the non–patterned region of interest (R), whereas the data shown in white–filled circles with two fits is for the region of interest that shows emergent structures (P). The shown analysis is run on a steady–state image for a 4.74 mm , 95 W sample at steady–state. b) Figure shows the time–dependence of the correlation length for a 4.74 mm sample at 23.8 W (green triangles) and 95 W (red and blue triangles) as it evolves from room–temperature equilibrium to an out–of–equilibrium steady–state on a semilog scale [6–8].

sophisticated technique. Therefore, we employ a spatial two–point autocorrelation to extract useful information about the emergent length scales from the system. It is done by comparing the frequencies of values in the temperature matrix, and then finding the most dominant frequencies. In this case, the autocorrelation function analyzes the 2D temperature profile matrix and finds correlations based on length, at an arbitrary delay, r away from each element in the matrix. The program is written following the Weiner–Khinchin theorem which relates the autocorrelation function to the power spectral density via the Fourier transform [8, 102]. The 2D spatial autocorrelation is executed using Python’s numpy library. We make use of its 2D fast Fourier transform and its complex conjugate functions, `fft.fft2` and `conj`. The matrix is normalized to a range of values $\{0, 1\}$. Numpy provides an-

other useful function called `fft.fftshift` which moves the zero coordinate to the center of the domain. Implementing this outputs a much smoother autocorrelation function as output. In order to convert the 2D autocorrelation function into a 1D radius based autocorrelation, all the elements inside the circle of arbitrary radius r around the center of the matrix are averaged and the normalized $\mathcal{G}_2(r)$ is plotted as a function of this delay. In Figure 3.13, the pattern of convective cells were characterized spatially by a tracking typical length-scales that emerge in the patterns as the system evolves on heating to an out-of-equilibrium steady-state. Length-scales were extracted from each image using a spatial two-point autocorrelation function, \mathcal{G}_2 , analysis on the thermal images. The spatial correlation function is defined as, $\mathcal{G}_2(r) = \langle T(R) \cdot T(R+r) \rangle - \langle T(R) \rangle \langle T(R+r) \rangle$, where $T(R)$ represents the temperature at an arbitrary location on the image, R , and $T(R+r)$, the temperature at a distance, r from R . A typical two-point autocorrelation function is shown in Figure 3.13a for a patterned and non-patterned image, P and R . The white filled-circles show the correlation data for the non-patterned region, R , described by a single exponential decay fit of the form, $\mathcal{G}_2(r) = C_1 \exp(-\frac{r}{\xi}) + C_0$. A correlation length (ξ) of 33 mm is estimated from the exponential fit for the 4.75 mm sample at 95 W in the non-patterned region, R . Whereas, for the patterned region, P , two correlation lengths are obtained, $\xi = 18.5$ mm and 9.3 mm. These lengths characterize the average length and width of the observed structures that appear worm-like in nature. Smaller correlation lengths imply increased heterogeneity, the thermal surface of the film becomes progressively structured in time. This is clearly visible from the thermal images shown in Figure 3.5b [6-8]. In particular, it was observed in Figure 3.13 that there are atleast two dominant length-scales. When the Rayleigh-Bénard system is at room temperature equilibrium, it is thermodynamically homogeneous over large length-scales. Once, visible patterns emerge due

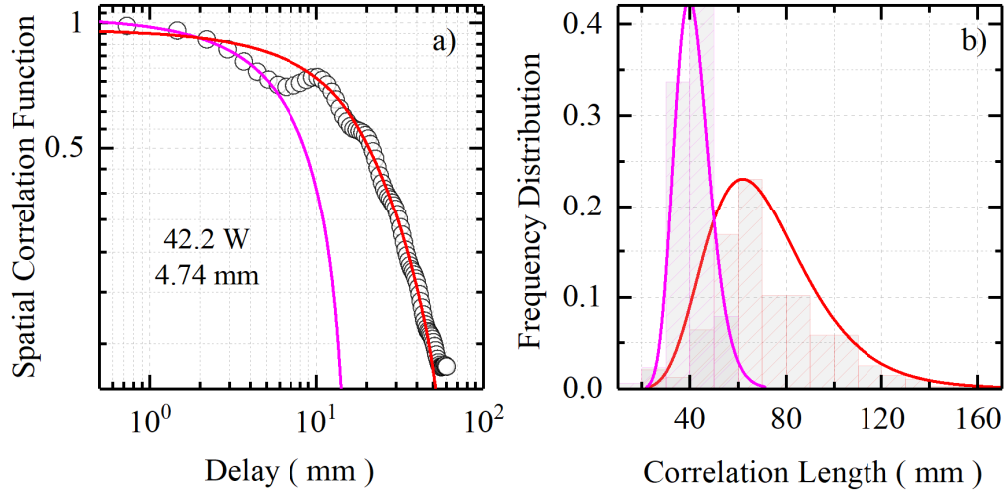


Figure 3.14: a) Figure shows the spatial autocorrelation data along with exponential fits for 4.74 mm sample at steady-state. b) Figure shows the distribution of the two correlation lengths as the 4.74 mm sample evolves into an out-of-equilibrium steady-state from room temperature equilibrium. The two distribution functions: normal (in magenta) and lognormal (in red) are also shown in the figure [6–8].

to the system being driven out-of-equilibrium, finer length-scales start emerging on top of the intrinsic larger length-scale, as shown in Figure 3.13 and 3.14a. A question that naturally follows is how these typical length-scales are distributed (in time) as the system evolves from a room temperature equilibrium to an out-of-equilibrium steady-state. The spatial autocorrelation script is implemented on all the 481 temperature matrices (or snapshots of the thermal images) while simultaneously fitting the spatial correlation data with exponential fits. The first data point of the spatial correlation dataset is always equal to one hence this point acts as an anchor for the first exponential fit. In order to obtain the second characteristic length, a search algorithm is implemented on the spatial correlation dataset to search for a local minima followed by a local maxima. The local maxima acts as the anchor for the second exponential fit. It is also made sure that the second exponential fit undercuts the first exponential fit. The correlation length from the first exponential fit gives an estimate of the finer length-scales whereas, the second

exponential fit gives an estimate of the larger (equilibrium or close to equilibrium) length scales in the system. The frequency histograms are then plotted as shown in Figure 3.14b. It is interesting to note that the larger length scales are lognormally distributed thus implying a positive skewness. Therefore, as the system ages (driven to a steady-state) finer length-scales emerge and a symmetrical normal distribution shifts towards the left. To put things into perspective of the system's physical dimension, the smallest length-scale is estimated to be never less than 20 *mm* and the largest length-scale is never greater than 120 *mm* which is slightly greater than the radius of the copper pan [7, 8].

Chapter 4

Theoretical Formalism of a Complex System

Traditionally, science has followed a reductionist approach, where a system that is composed of numerous interacting parts is assumed to behave the way its individual constituents would behave if those interactions were absent. The origins of this approach lies in the mechanistic viewpoint of this universe. Surely, it has proven to be successful in helping us understand better the universe, yet it falters time and again in providing an explanation for the ubiquitous emergent complexity around us. Therefore, in the context of complex systems science it is rightly said that ‘a (complex) system is always greater than the sum of its parts’. As discussed in the previous sections, interpreting complexity from a mechanistic view point is a difficult subject, but a subject of great general interest. Therefore, in this context, one must first identify the physical concepts/laws/principles that are of paramount importance. Our experimental studies have provided us a basis to identify some of these underlying concepts in order to build a theory.

4.1 Broken Symmetries

Symmetry breaking is one of the most important phenomena in the study of complex systems' science. The process of symmetry breaking involves driving a system from a state of random disorder (symmetry) to a state of order during pattern formation (symmetry-breaking) [17, 75]. In deeper sense, symmetries in a system is directly related to conservation laws, also known as Noether's theorem [5, 39]. For example, time-reversal symmetry implies conservation of energy, while translational and rotational invariance imply conservation of momenta, linear and angular. In the Rayleigh-Bénard system we observe symmetry breaking as a result of pattern formation. In Figure 4.1a, we show the histogram distribution when our region of interest falls over the patterns in the thermal images. We identify the two peaks and perform two independent Gaussian fits, $\mathcal{N}(\mu_k, \sigma_k^2)$ on the data: $\mathcal{N}(89.25 \pm 0.089, 1.25)$ for the 'hot' region (in red) and $\mathcal{N}(86.21 \pm 0.13, 1.24)$ for the 'cold' region (in blue). The shaded region enclosing both the Gaussian fits is a cumulative fit function. We have shown in the earlier section that a kernel density estimate provides a better description of the shape of the frequency data, $\hat{f}(T) = \frac{1}{nh} \sum_i K(\frac{T-T_i}{h})$. However, a kernel smoothing with Gaussian kernels ($K(\cdot)$) does not present any intuitive understanding of the physics beyond the shape of the estimate function. We identify the point where the two independent Gaussian fits intersect each other. We set the temperature at the point of intersection of the two curves as a threshold (T_{th}) to slice the frequency data into two regimes: 'hot' and 'cold'. Two independent 1D arrays are created and the temperature frequency data is binned accordingly: if $T_i \leq T_{th}$ then the list of all T_i is in 'cold' region and if $T_i > T_{th}$ then the list of all T_i is in 'hot' region. We look at their independent statistics in Figure 4.1b and 4.1c. The histograms are clearly normally distributed with $\mathcal{N}(89.48, 0.64)$ for the isolated

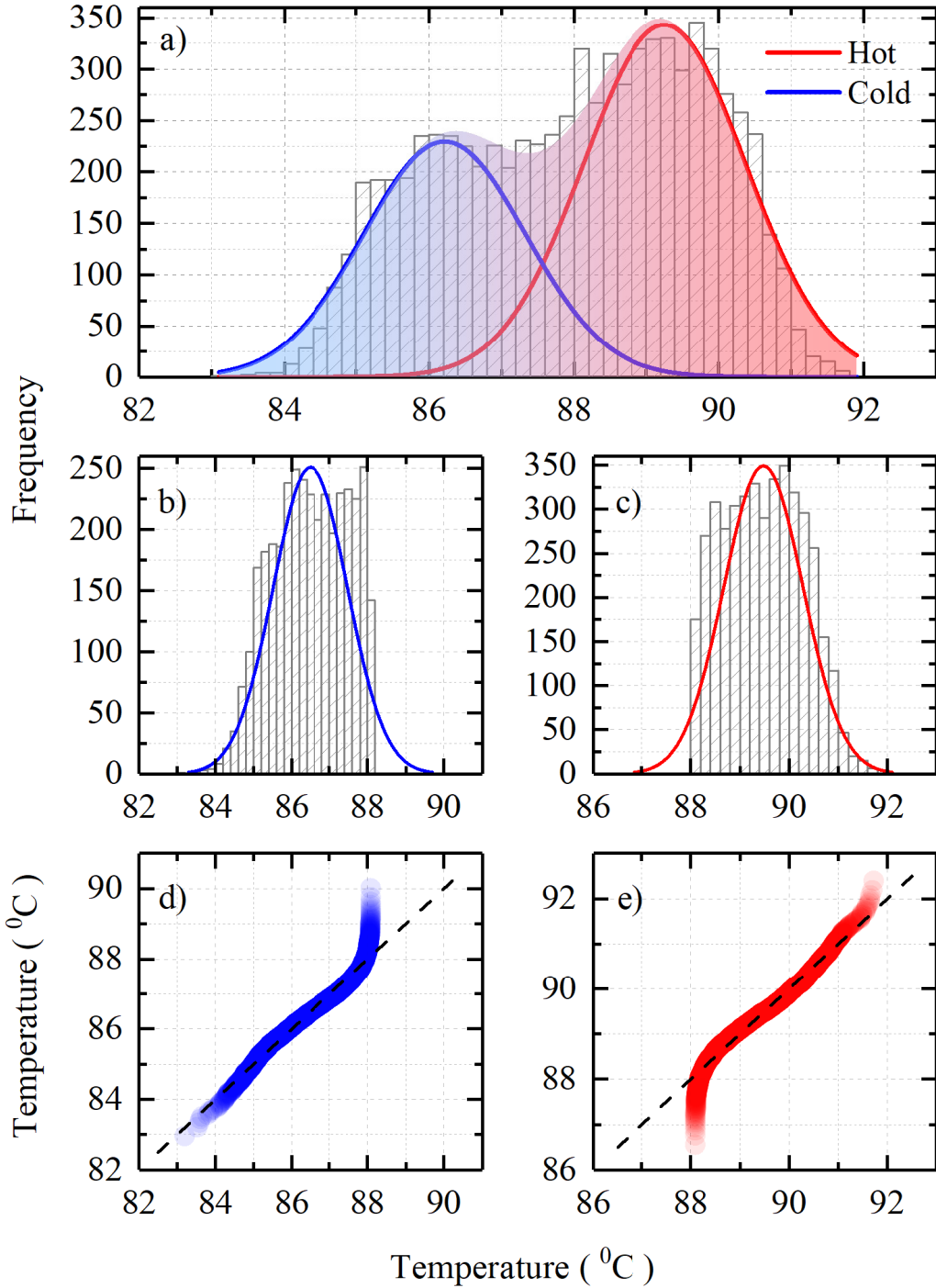


Figure 4.1: a) Figure shows a bimodal distribution of the temperature frequency distribution over a region of pattern. Two independent Gaussian fits are performed which are identified as 'hot' (in red) and 'cold' (in blue). The shaded region is the cumulative function obtained from the two independent fits. In b) and c) a threshold temperature, T_{th} is used to slice the data into two separate 1D arrays and their frequency histograms are plotted with the respective Gaussian fit functions. The normality is further tested in d) and e) by plotting the respective Q-Q plots at 95% CI [7].

‘hot’ region and $\mathcal{N}(86.49, 0.96)$ for the isolated ‘cold’ region. One can see that the descriptive statistics of the isolated regions is well within one standard deviation of the continuous region with 95% CI. To further elucidate the normal behavior we show the Q–Q plots for the isolated regions in Figure 4.1d and 4.1e. One can clearly note that at $T_i \sim T_{th}$ the curves depart from normality whereas everywhere else they are in agreement with the normal nature of the frequency distribution. We consider this result important, as it allows for the coexistence of multiple ‘equilibrium–like’ domains in an out–of–equilibrium steady–state system [4, 6]. Likewise, the temporal statistics from the fluctuation distribution are plotted in Figure 4.2. The time–series data is shown in Figure 4.2a. To obtain robust temporal statistics, regions of interest were selected on the thermal images and were spatially averaged across frames. In Figure 4.2b, 4.2c, and 4.2d we plot the frequency histograms for the ‘hot’ (in red), ‘cold’ (in blue) and the whole region (in light grey). These histograms are clearly normally distributed: $\mathcal{N}(90.16 \pm 0.0036, 0.30)$ (red), $\mathcal{N}(72.91 \pm 0.007, 1.36)$ (blue) and $\mathcal{N}(81.47, 0.11)$ all at 95% CI. The statistical mean of the whole region is found to be very close to the average of the statistical means of the respective ‘hot’ and the ‘cold’ regions. To further ascertain the normality of the frequency histograms, Q–Q plots are shown for the each of the regions of interest in Figure 4.2e, 4.2f, and 4.2g. The descriptive statistics presented above show that the spatial symmetry is broken as patterns emerge while temporal symmetry is preserved, thus the energy of the system is conserved. One may argue that the system is dissipative, and therefore the Hamiltonian can not be explicitly written and extremal principles can not be applied. However, one can supersede these criticisms under certain constraints: when the local equilibrium hypothesis holds true and large deviations from equilibrium are excluded, extremal principles can be applied to a dissipative system [35]. Therefore, in this regard the non–turbulent Rayleigh–Bénard system is of special interest to

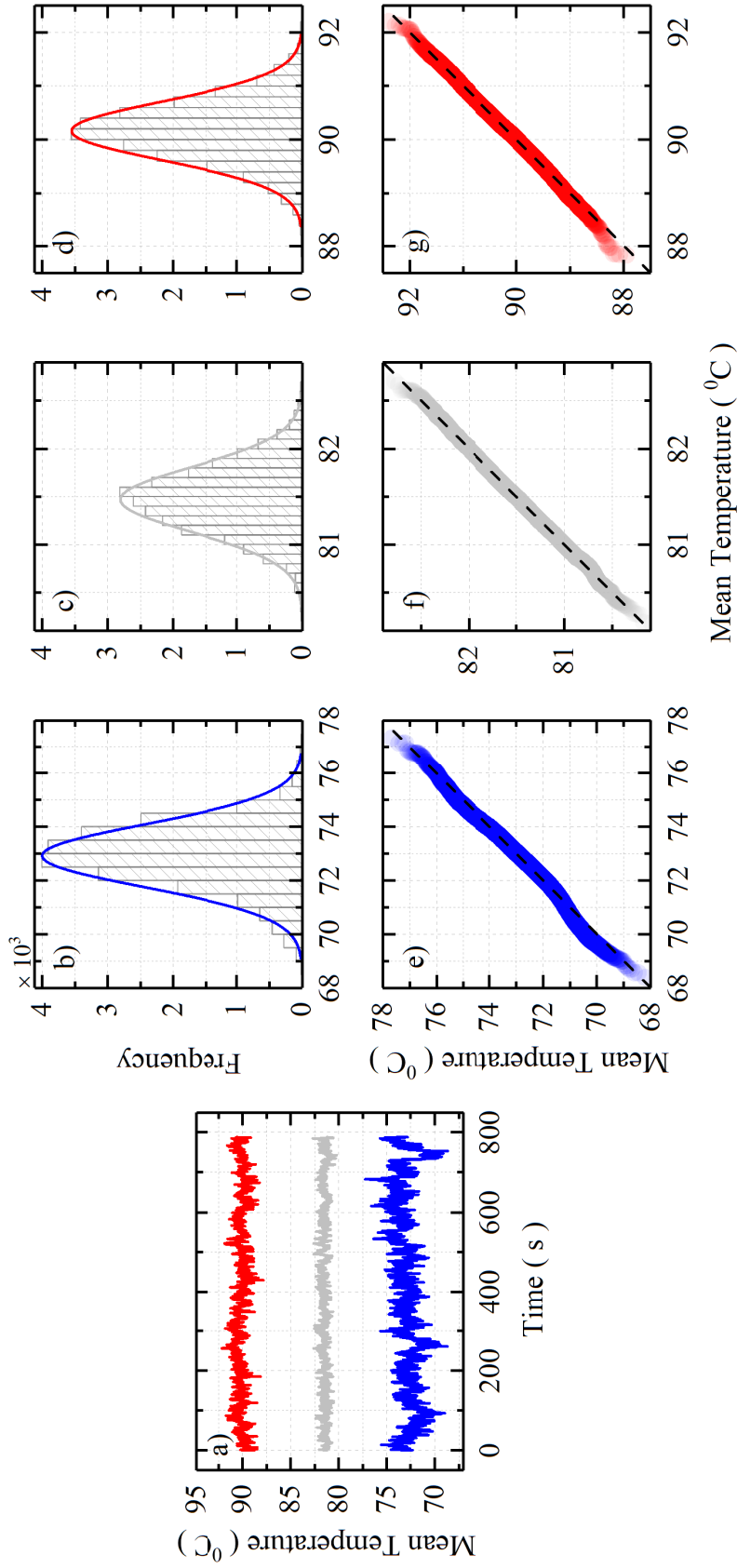


Figure 4.2: a) Figure shows the spatially averaged temperature in different regions of interest as a function of time in a time-series plot. In b), c), and d) the time-series data is plotted as frequency histograms for 'cold' (in blue), whole (in light grey), and 'hot' (in red) regions respectively. In e), f), and g) the Q-Q plots are shown for each case to test for normality [7].

Table 4.1: Table shows the calorimetric data from the steady-state images at different powers for the two thickness ($l_z = 4.74 \text{ mm}$ and 5.02 mm). The numbers listed in the first column denote the specified points in the plots shown in Figure 4.3. The top temperature (T_{top}) is recorded by the thermal camera, bottom temperature (T_{bottom}) by the thermocouple T_2 , the hot and cold spot temperatures ($T_{P_{hot}}$ and $T_{P_{cold}}$) are obtained by spatially averaging regions of interest (P_{hot} and P_{cold}) from the thermal images, conduction temperature (T_{cond}) is calculated from Equation 4.1, and the Rayleigh Number ($Ra = \frac{g\beta l_z^3}{\nu\alpha}(T_{bottom} - T_{top})$) from the listed values in Table 3.1 [6].

l_z (mm)	#	Power (W)	T_{top} ($^{\circ}C$)	$T_{P_{hot}}$ ($^{\circ}C$)	$T_{P_{cold}}$ ($^{\circ}C$)	T_{bottom} ($^{\circ}C$)	T_{cond} ($^{\circ}C$)	Rayleigh Number Ra
4.74	1	23.8	39.4	--	--	53.2	46.8	831
	2	42.2	48.4	61.5	54.8	71.7	61.7	1410
	3	66	59.9	78.2	69.7	89.5	76.1	1790
	4	95	70.9	100.9	91.1	115	96.4	2670
	5	130	89.8	124.8	114.1	147	122.2	3464
5.02	1	10.5	30.3	--	--	37.9	34.5	535
	2	23.8	38.1	43.1	39.7	53.4	46.9	1080
	3	42.2	47.2	63.5	56.7	70.9	60.9	1670
	4	66	58.8	84.4	73.6	91.8	77.7	2330
	5	95	73.1	101.3	90.1	115	96.4	2960

derive insights about far-from-equilibrium thermodynamics, and quantify pattern formation in complex systems based on our basic understanding of thermodynamics.

We ask ourselves a not so obvious question, what would have been the theoretical temperature of the top surface of the fluid film if the mechanism of heat transport had been through pure conduction? In order to calculate the theoretical conductive temperature, T_{cond} , the steady-state heat conduction equation is used along with the available calorimetry data from Tables 3.1 and 4.1,

$$\dot{Q} = \frac{(m_{Cu}c_{pCu} + m_{oil}c_{p_{oil}})(T_{bottom} - T_{top})}{2 \times 60 \times 60} = -kA\nabla T = -kA\left(\frac{T_{cond} - T_{bottom}}{l_z}\right), \quad (4.1)$$

Here, A is the area of the copper pan, the material properties are given in Table 3.1, and the measured temperature values of the theoretical expected temper-

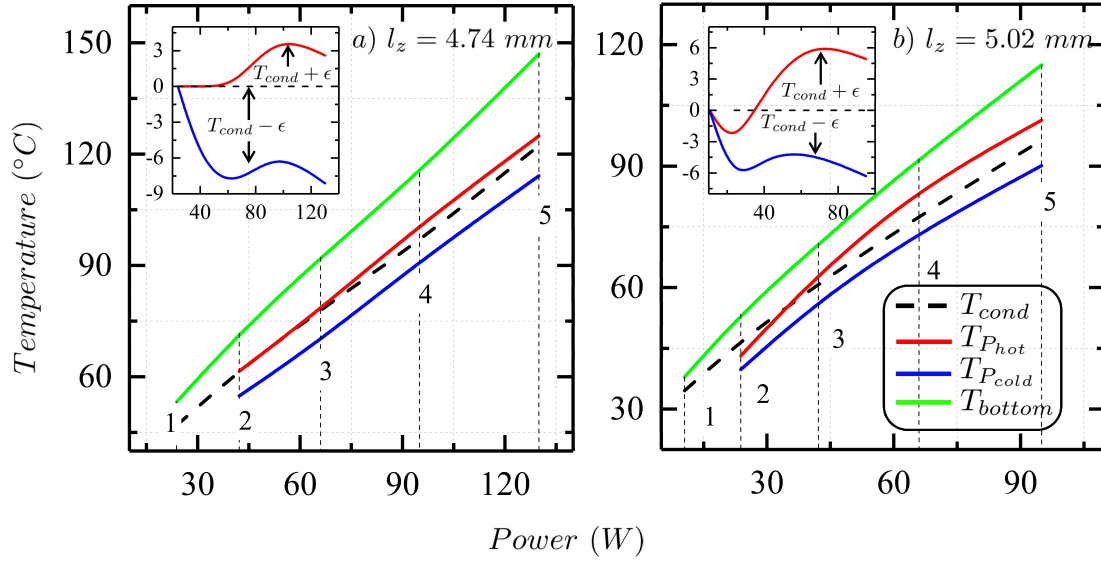


Figure 4.3: Figure shows the temperature plots ($T_{P_{hot}}$, $T_{P_{cold}}$, T_{cond} and T_{bottom}) for the steady-state images at different values of input power for a) $l_z = 4.74 \text{ mm}$ and b) $l_z = 5.02 \text{ mm}$. The inset plots capture the variation in the plume temperatures ($T_{P_{hot}}$ and $T_{P_{cold}}$) about the theoretical conduction temperature (T_{cond}) as a function of power. For details about the specific points denoted in the plots, refer Table 4.1. Also, note that ϵ is arbitrary [6].

ature (T_{cond}) and the temperature of the upward and downward drafts ($T_{P_{hot}}$ and $T_{P_{cold}}$) from Table 4.1. The resulting values of all the temperatures are listed for both the thicknesses in Table 4.1 and plotted as a function of applied power in Figure 4.3. The critical Rayleigh number for structures to emerge is 1708 and for experiments beyond this critical value (see Table 4.1 last column, after third row), the theoretical conduction temperature is close to the weighted average of the hot and cold plume temperatures denoted by, $T_{P_{hot}}$ and $T_{P_{cold}}$. In the inset of Figure 4.3, the variance of the plume temperatures about the conduction temperature ($T_{cond} + \epsilon$ and $T_{cond} - \epsilon$) as a function of the applied power is shown. Interestingly, the nature of this variation does not follow a linear relationship, but rather oscillates above and below T_{cond} almost anti-symmetrically. Although macroscopically the system is at steady-state, the regions in space corresponding to P_{hot} and P_{cold} can be realized

as localized heat baths with equilibrium-like statistics confined within them. The dissipation from the equilibrium fluctuations within these localized regions manifests as a spatial variation of the temperature manifold, the curvature of which indicates how far one is from the equilibrium state, T_{cond} (see Figure 4.3). The upward and downward drafts at these localized regions perform internal work to maintain the convection (structure and internal gradients) while resisting spontaneous equilibration. An intuitive understanding of this mechanism is the bifurcation of the theoretical conduction temperature beyond the critical Rayleigh number (see Figure 4.3). Therefore, in order to interpret temperature far-from-equilibrium we must consider, temperature not as state variable but as a functional on the energy landscape [4]. This energy landscape consists of local equilibrium-like points (domains), and within each of these regions the macroscopic equilibrium thermodynamics ideally holds true. A theory that would encompass this idea must have to preserve the first law while modifying it to include the emergence of internal gradients [3, 6–8, 21, 22, 78, 101, 103, 104].

4.2 Foundations of a Theory

The definition of temperature like any other state variable in non-equilibrium thermodynamics remains a subject of great difficulty even to this day [43, 105]. As the Rayleigh-Bénard system is driven, the emergent complexity observed on the top layer of the fluid film are observed to be stable thermal gradients which last as long as the system is driven, and disappear the moment the power is switched off. For every ‘hot’ spot (plume), it is observed that there exist a ‘cold’ spot (plume). We describe this through an illustration in Figure 4.4. The collection of all the ‘hot’ domains (ε_i) signify local order in the medium whereas the collection of ‘cold’ domains

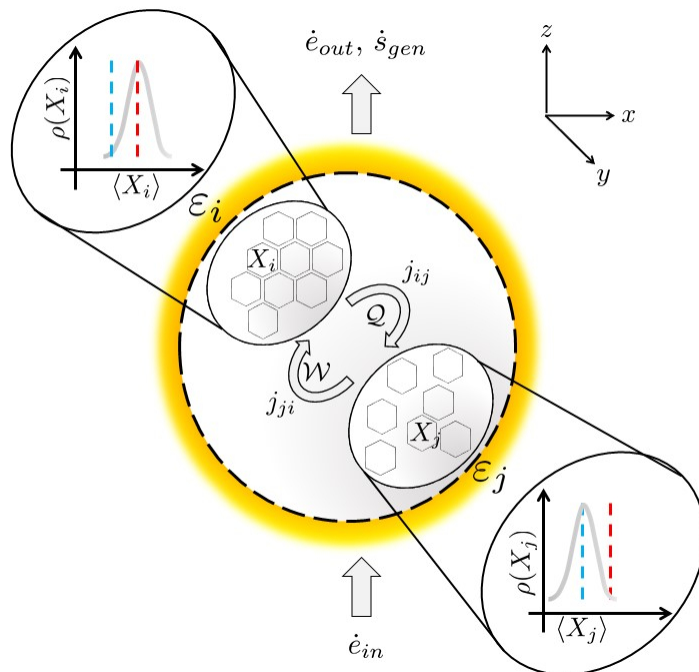


Figure 4.4: Figure shows a typical Rayleigh–Bénard convection with emergent order. When the fluid film is heated from the bottom (z -axis), regions of order (ε_i) and disorder (ε_j) emerge on the top-layer of the fluid film (xy -plane). The presence of the internal gradients leads to internal currents, j_{ji} that converts heat (\mathcal{Q}) into work (\mathcal{W}), and j_{ij} dissipates order back to disorder. These local internal fluxes exist because the system as a whole is driven far-from-equilibrium, and one exists as long as the other does hence, $j_{ij} = -j_{ji}$. The distribution ($\rho(X)$) in the insets represent the statistical distribution of the temperature in the domains ε_i and ε_j . Since, local equilibrium hypothesis holds true, one can see that the distribution is normal and centered around the mean, $\langle X \rangle$.

(ε_j) act as local sinks. At steady-state, the thermal fluctuations in these localized domains are studied [6, 7, 42]. We have seen in the earlier sections, that it is both surprising and remarkable that the descriptive statistics obtained from these locally distributed regions of stable-in-time thermal gradients exhibit equilibrium-like fluctuations while spatially coexisting in a far-from-equilibrium state. The partitioning of the total internal energy of the system into entropic part (disorder) and coherent work (order), as shown in Figure 4.3, is maintained by the flow of internal currents, $j_{ij} \propto (\langle X_i \rangle - \langle X_j \rangle)$ and $j_{ij} = -j_{ji}$ (note that $X = \text{temperature}$). These internal cur-

rents dictate the time-scale responsible for local equilibration of these domains, and is much faster than the macroscopic evolution of the system at steady-state [6, 7]. As these two relaxation times differ significantly, and the statistical results from the domains show normal trends one can readily conclude that the local equilibrium hypothesis holds true in this scenario [35, 37, 43, 51–54].

Therefore, we can envision a manifold on which the temperature scalar is embedded, the curvature of this manifold indicates how far one is from an equilibrium state [3, 4, 6]. This idea, as we shall see in the next sections, is extended to derive an equation of state for a driven far-from-equilibrium system from the first principles.

4.3 Thermodynamic Lagrangian

Let Ω , a finite thermodynamic system with a well-defined boundary, $\partial\Omega$ be driven by an external field. The system is free to exchange heat with its surroundings. In a convective system like the Rayleigh–Bénard, the spatial dependence of temperature can be effectively computed using the Navier–Stokes equation with Boussinesq approximation [54, 79]. As temperature is our thermodynamic observable (X), it will have well defined values at each point in space (x_μ) inside the system (and on the system boundary), and therefore can be expressed as a tuple (X, x_μ) . In a simple Rayleigh–Bénard setup (as in our case [6, 7]), the system is excited by actively driving it along one axis say, z -axis while structures emerge on the plane orthogonal to the axis of the driving field, the xy -plane. Therefore, we constrain the index, μ to take only the following values, $\mu = (-t, x, y)$. In a two-dimensional \mathbb{R}^2 space, we can construct arbitrary sequences of temperature values corresponding to real coordinates in space, $\{X_k\}$ bounded above and below by the finite boundary values, $X_{min} \leq \{X_k\} \leq X_{max}$. The boundary values for the system, X_{min} and X_{max} are

determined by the bath and the driving field. For a system which is thermodynamically homogeneous, this sequence is convergent, $|X_i - X_j| < \epsilon$ where X_i and X_j belong to the sequence $\{X_k\}$. For large N , this sequence converges to the canonical temperature of the system, or $\lim_{k \rightarrow N} \{X_k\} \rightarrow \langle X \rangle$ (Central Limit Theorem). In a system that has been driven out-of-equilibrium one can only comment on the convergence and boundedness of the sequence, $\{X_k\}$ under special circumstances. One such situation arises when the local equilibrium hypothesis is satisfied. For example, in a non-turbulent Rayleigh-Bénard system at steady-state ($Ra \lesssim 10^4$), emergent behavior is manifested as structural ordering in form of patterns of varying complexity. For low Rayleigh numbers these patterns are stable in time as the fluid flow is non-turbulent. Under this circumstance one can conclusively state domain-wise convergence of sub-sequences of $\{X_k\}$. A domain, $\varepsilon_i \subseteq \Omega$ consists of a tuple $(\{X_{i_k}\}, x_\mu) \forall x_\mu \in \varepsilon_i \subseteq \Omega$ (at steady-state one can ignore the time component). The elements of the sub-sequence $\{X_{i_k}\}$ can either be experimentally measured through real-time infra-red imaging, through thermal probes that flow with the convection currents or computationally through the simulation of the Navier-Stokes equation with the Boussinesq approximation [54, 65, 86, 93, 98, 99, 106]. We saw in the earlier sections that the two well-defined domains – ‘hot-spots’ and ‘cold-spots’ – were observed to follow normal distributions. Therefore, one can conclusively state that, $\{X_{i_k}\}_{\varepsilon_i} \rightarrow \langle X_i \rangle$ where the sub-sequence $\{X_{i_k}\}$ of the sequence $\{X_k\}$ converges to the domain mean, $\langle X_i \rangle$ for large $n \in \varepsilon_i \subseteq \Omega$ [4, 6, 7]. Under the circumstances when the Rayleigh-Bénard system is driven in the turbulent regime ($Ra \gtrsim 10^5$), due to dominating dissipative effects sequences as such, of velocities and temperature will not converge with the system mean and hence these structures are not stable in time rather they are strongly time-dependent and often chaotic [86, 99]. As Chandrasekhar notes, the symmetry-breaking instabilities in a Rayleigh-Bénard

convection is maintained through the interplay between the kinetic energy dissipated through viscosity and internal energy released due to buoyancy [94]. The kinetic energy dissipated due to fluid friction is the incoherent part while the buoyancy manifested internal energy comes at the expense of moving a volume of fluid through a convective cycle, therefore being coherent in nature. Thus, the driving potential bifurcates the internal energy of the system into coherent and incoherent parts (see Figures 4.3 and 4.4). Under the condition that the local equilibrium hypothesis holds, we can define a thermodynamic Lagrangian density, \mathcal{L}_T for such a system as the difference between the incoherent heat ($\mathcal{Q} = T\mathcal{S}$) and emergent work (\mathcal{W}).

$$\mathcal{L}_T = \mathcal{Q} - \mathcal{W} = T\mathcal{S} - \mathcal{W} \quad (4.2)$$

Similarly, we can define the Hamiltonian density, \mathcal{H} as the sum total of the incoherent and coherent parts due to the driving field:

$$\mathcal{H} = \mathcal{Q} + \mathcal{W} = T\mathcal{S} + \mathcal{W} \quad (4.3)$$

Both the Lagrangian and Hamiltonian densities are extensive properties and can be expressed as functions of the intensive variables, X (where X denotes the class of intensive thermodynamic variables, $X = (P, T, \mu, \dots)$). This definition of the thermodynamic Lagrangian is in-line with many previous authors [25, 107, 108]. Based on our discussion above, we can assign a mathematical structure to our thermodynamic system. As each point in the system can be expressed as a tuple, (X, x_μ) we can define a functional dependence of X on the space-time coordinates, $X : x_\mu \in \Omega \rightarrow \{X_k\} \in \mathbb{R}$ or $X = X(x_\mu) \forall x_\mu \in \Omega$. Due to finiteness of the system the function X can be non-arguably assumed to be continuous, or C^0 , and for the sake of generality, we assume that X is analytic and hence C^∞ continuous.

Therefore, the Lagrangian density in Equation 4.2 can be rewritten as,

$$\mathcal{L}_T(X, \partial_\mu X) = \mathcal{Q}(X, \partial_\mu X) - \mathcal{W}(X, \partial_\mu X) = T\mathcal{S}(X, \partial_\mu X) - \mathcal{W}(X, \partial_\mu X) \quad (4.4)$$

As temperature is our thermodynamic observable (X), the system has well-defined boundary conditions, $T_{top} \leq X \leq T_{bottom}$ and we can expand X as an analytic function (in one dimension) in the neighborhood of an arbitrary point in space, $T_{top} \leq X(x) = \sum_{k=0}^{\infty} a_k(x - x_k)^k \leq T_{bottom} < \infty$. If we refer to Figure 4.4, we will note that the locally coexisting equilibrium-like domains are denoted by $(\varepsilon_i, \varepsilon_j)$. As these regions are equilibrium-like domains, they are bounded, and one can mathematically view them as compact subsets of the system, $\varepsilon_i, \varepsilon_j \subseteq \Omega$ where sub-sequences of $\{X_k\}$ converge. These compact subsets consist of sequences of space-time coordinates and sub-sequences of $\{X_k\}$, such that $(\{X_{i_k}\}, \{x_\mu\}) \in \varepsilon_i \subseteq \Omega$ and $\xi_T \leq \{x_\mu\} \leq \ell_\mu$. The bounds on the size of the set is defined by the thermal correlation length at equilibrium ξ_T and emergent characteristic length ℓ_μ whereas from Central Limit Theorem, $\{X_{i_k}\} \rightarrow \langle X_i \rangle$ for large n . For such compact sets $(\varepsilon_i, \varepsilon_j)$ in which sub-sequences $(\{X_{i_k}\}, \{X_{j_k}\})$ converge to $(\langle X_i \rangle, \langle X_j \rangle)$ we can define a functional, \mathcal{S} such that, $\mathcal{S} : (\varepsilon_i, \varepsilon_j) \subseteq \Omega \rightarrow (\langle X_i \rangle, \langle X_j \rangle) \in \{X_k\}$. This functional traces trajectories on the thermodynamic manifold which connects one locally equilibrated region to the other in a driven system. This functional thus takes on the role of action and is expressed as,

$$\mathcal{S}[X] = \int d^3x_\mu \mathcal{L}_T(X, \partial_\mu X) \quad (4.5)$$

4.4 Equation of State with Emergent Order

On minimizing the action functional from Equation 2.2, $\delta\mathcal{S}[x] \rightarrow 0$ we obtain the Euler–Lagrange equation,

$$\frac{\partial\mathcal{L}_T}{\partial X} - \partial_\mu\left(\frac{\partial\mathcal{L}_T}{\partial(\partial_\mu X)}\right) = 0 \quad (4.6)$$

For the case, $x_\mu = (-t, x)$ with $c = 1$, and the Lagrangian density, $\mathcal{L}_T = \mathcal{L}_T(X, \partial_x X, \partial_t X)$,

$$\frac{\partial\mathcal{L}_T}{\partial X} = \frac{d}{dx}\left(\frac{\partial\mathcal{L}_T}{\partial(\partial_x X)}\right) = \frac{d}{dt}\left(\frac{\partial\mathcal{L}_T}{\partial(\partial_t X)}\right) \quad (4.7)$$

On solving Equation 4.7 for the spatial and the temporal case independently we have the following set of equations of motion,

$$\delta\mathcal{Q} - \delta\mathcal{W} = \frac{d}{dx}\left(\frac{\partial\mathcal{Q}}{\partial(\partial_x X)} - \frac{\partial\mathcal{W}}{\partial(\partial_x X)}\right)dX = \frac{d}{dt}\left(\frac{\partial\mathcal{Q}}{\partial(\partial_t X)} - \frac{\partial\mathcal{W}}{\partial(\partial_t X)}\right)dX \quad (4.8)$$

We substitute the spatial and temporal derivatives of X in the above equation by the functions, $\partial_x X = f(X_i, X_j; x)$ and $\partial_t X = g(X_i, X_j; t)$. These functions, $f(\cdot)$ and $g(\cdot)$ denote the spatio–temporal gradients along paths that connect two local equilibrium–like domains, $(\varepsilon_i, \varepsilon_j)$ with the mean values of the fluctuating intensive variables as, $(\langle X_i \rangle, \langle X_j \rangle)$. Substituting the functional form of the gradients into Equation 4.8 we have,

$$\delta\mathcal{Q} - \delta\mathcal{W} = \partial_x\left(\frac{\partial\mathcal{Q}}{\partial f} - \frac{\partial\mathcal{W}}{\partial f}\right)dX = \partial_t\left(\frac{\partial\mathcal{Q}}{\partial g} - \frac{\partial\mathcal{W}}{\partial g}\right)dX \quad (4.9)$$

Using the chain rule,

$$\delta\mathcal{Q} - \delta\mathcal{W} = \partial_x\left(\left(\frac{\partial\mathcal{Q}}{\partial x} - \frac{\partial\mathcal{W}}{\partial x}\right) \times \frac{\partial x}{\partial f}\right)dX = \partial_t\left(\left(\frac{\partial\mathcal{Q}}{\partial t} - \frac{\partial\mathcal{W}}{\partial t}\right) \times \frac{\partial t}{\partial g}\right)dX \quad (4.10)$$

As $f = \partial_x X$ and $g = \partial_t X$ therefore, $\partial f / \partial x = \partial_x^2 X$ and $\partial g / \partial t = \partial_t^2 X$. For a driven system that gives rise to emergent structures which are stable, Chandrasekhar points out that the gradient of the intensive scalar assumes a minima [94]. Therefore, the second derivative of the intensive variable vanishes, and Equation 4.10 becomes undefined. In order to proceed further, we treat the problem differently by exploiting the mathematical structure of the underlying coordinate system. The functions that define the manifold are analytic, and as our system is finite, these functions are bounded by well defined boundary conditions. As discussed earlier, the system is heated at the base and convection patterns emerge on the top layer of the fluid film. We can define a metric connecting any two points in the space (on the top layer of the fluid film) as our underlying vector space has a well defined norm, $\|x_\mu\| \geq 0$, and a complete normed vector space is a Banach space (as sequences converge). Our coordinate system is therefore, a Banach space in \mathbb{R}^2 [109]. The partial derivatives of \mathcal{Q} and \mathcal{W} with respect to the functions $f(\cdot)$ and $g(\cdot)$ can then be expressed as Fréchet derivatives, or $\partial \mathcal{Q} / \partial f = \delta \mathcal{Q} / \delta f$ and $\partial \mathcal{Q} / \partial g = \delta \mathcal{Q} / \delta g$ [109, 110]. Rewriting Equation 4.10 below,

$$\delta \mathcal{Q} - \delta \mathcal{W} = \partial_x \left(\frac{\delta \mathcal{Q}}{\delta f} - \frac{\delta \mathcal{W}}{\delta f} \right) dX = \partial_t \left(\frac{\delta \mathcal{Q}}{\delta g} - \frac{\delta \mathcal{W}}{\delta g} \right) dX \quad (4.11)$$

The variation of a function can be expressed as, $\delta f(X_i, X_j; x) = \epsilon \eta(X_i, X_j; x)$ and $\delta g(X_i, X_j; t) = \epsilon \eta'(X_i, X_j; t)$ where ϵ is infinitesimal and $(\eta(\cdot), \eta'(\cdot))$ are arbitrary functions. Also, note that $\partial_x(\delta \mathcal{Q}) = \int \partial_x(\partial \mathcal{Q} / \partial x) dx = \delta(\partial_x \mathcal{Q})$. Upon rearranging, Equation 4.11 takes the form,

$$\delta \mathcal{Q} - \delta \mathcal{W} = \delta(\partial_x \mathcal{Q} - \partial_x \mathcal{W}) \frac{dX}{\epsilon \eta(x)} = \delta(\partial_t \mathcal{Q} - \partial_t \mathcal{W}) \frac{dX}{\epsilon \eta'(t)} \quad (4.12)$$

Since X is analytic, the functions, $f(\cdot)$ and $g(\cdot)$ are also analytic. Therefore the functions, $\eta(x)$ and $\eta'(t)$ can be expanded as infinite series in the neighborhood of some arbitrary point, $x_0 \in \varepsilon_i$ at time, t_0 or $(x_0, t_0) \rightarrow (x_0 \pm h; t_0 \pm k)$, such that $\eta(X_i, X_j; x) = \sum_{k=0}^{\infty} c_k(x - x_0)^k$ and $\eta'(X_i, X_j; t) = \sum_{k=0}^{\infty} c'_k(t - t_0)^k$. One of the useful properties of Banach space that can be exploited is that, Cauchy sequences always converge in a Banach space to a well defined limit. As the system is finite, the Taylor series is a bounded Cauchy-type sequence which converges within the neighborhood of (x_0, t_0) . For the linear approximation, $\eta(X_i, X_j; x) = c_0 + c_1(x - x_0)$ and $\eta'(X_i, X_j; t) = c'_0 + c'_1(t - t_0)$. On multiplying the infinitesimal quantity, ϵ and rewriting Equation 4.12,

$$\delta \mathcal{Q} - \delta \mathcal{W} = \delta(\partial_x \mathcal{Q} - \partial_x \mathcal{W}) \frac{dX}{\epsilon(c_0 + c_1(x - x_0))} = \delta(\partial_t \mathcal{Q} - \partial_t \mathcal{W}) \frac{dX}{\epsilon(c'_0 + c'_1(t - t_0))} \quad (4.13)$$

Since, ϵ is infinitesimal, the pair $(\epsilon c_0, \epsilon c'_0) \rightarrow 0$, while $\epsilon(x - x_0) \rightarrow dx$, and $\epsilon(t - t_0) \rightarrow dt$ (from the definition of calculus). Equation 4.13 therefore becomes,

$$\delta \mathcal{Q} - \delta \mathcal{W} = \delta(\partial_x \mathcal{Q} - \partial_x \mathcal{W}) \frac{dX}{dx} c_1^{-1} = \delta(\partial_t \mathcal{Q} - \partial_t \mathcal{W}) \frac{dX}{dt} c'_1{}^{-1} \quad (4.14)$$

This leads us to the one-dimensional derivative of the intensive variable, $dX/dx = f(X_i, X_j; x)$ and $dX/dt = g(X_i, X_j; t)$. Since, $f(\cdot)$ and $g(\cdot)$ are both analytic, we can expand them as an infinite series in the neighborhood of $(x_0 \pm h; t_0 \pm k)$. Therefore, $f(X_i, X_j; x) = \sum_{k=0}^{\infty} \alpha_k(x - x_0)^k$ and $g(X_i, X_j; t) = \sum_{k=0}^{\infty} \alpha'_k(t - t_0)^k$. Using first-order linear approximation for $f(\cdot)$ and $g(\cdot)$ we rewrite Equation 4.14 as,

$$\delta \mathcal{Q} - \delta \mathcal{W} = \delta(\partial_x \mathcal{Q} - \partial_x \mathcal{W}) \left(\frac{\alpha_0 + \alpha_1(x - x_0)}{c_1} \right) = \delta(\partial_t \mathcal{Q} - \partial_t \mathcal{W}) \left(\frac{\alpha'_0 + \alpha'_1(t - t_0)}{c'_1} \right) \quad (4.15)$$

The constant, $|\alpha_0/c_1|$ has the dimension of length (ℓ) and the constant, $|\alpha'_0/c'_1|$ the dimension of time (τ). Whereas, the constants, $|\alpha_1/c_1| = k$ and $|\alpha'_1/c'_1| = k'$ are dimensionless scaling coefficients. Also, $\delta(\partial_x \mathcal{Q})(x - x_0) = \partial_x(\delta \mathcal{Q})(x - x_0)$. As, $|x - x_0| < \epsilon$ one can write $\partial_x(\delta \mathcal{Q})(x - x_0) = \partial_x(\delta \mathcal{Q})\delta x = \delta(\delta \mathcal{Q})$. Rearranging Equation 4.15 and substituting the characteristic constants, (ℓ, τ) we get,

$$(\delta \mathcal{Q} + k\delta(\delta \mathcal{Q})) - (\delta \mathcal{W} + k'\delta(\delta \mathcal{W})) + \delta(\ell\partial_x \mathcal{Q} + \tau\partial_t \mathcal{Q}) - \delta(\ell\partial_x \mathcal{W} + \tau\partial_t \mathcal{W}) = 0 \quad (4.16)$$

Equation 4.16 lays out the one-dimensional equation of state for a driven system far-from-equilibrium with emergent scales, (ℓ, τ) when the local equilibrium hypothesis holds true. At steady-state, the time-dependence goes away and the equation of state then follows as,

$$(\delta \mathcal{Q} - \delta \mathcal{W}) + (k\delta^2 \mathcal{Q} - k'\delta^2 \mathcal{W}) + \ell\delta(\partial_x \mathcal{Q} - \partial_x \mathcal{W}) = 0 \quad (4.17)$$

At equilibrium, the system is thermodynamically homogeneous therefore not only the gradients vanish, but the pair of constants (k, k') also become irrelevant as they originate from the series expansion of the gradients. Therefore, $\delta \mathcal{Q} - \delta \mathcal{W} = 0$, and one recovers the first law of thermodynamics from Equation 4.17 at thermodynamic equilibrium.

Chapter 5

Future Directions

The results presented in this paper and the nature of our theoretical formalism allows us to draw connections to other stochastic systems. In this chapter, we first extend our theoretical discussions in relation to the geometry of the spatio-temporal fluctuations in equilibrium and out-of-equilibrium scenarios. Following which, we ponder on the connections between time, Loschmidt's paradox and thermodynamics. Finally, we look for connections between our results presented in this work with stochastic simulations on driven coupled systems and turbulent convection.

5.1 Further Theoretical Considerations

Since, \mathcal{Q} and \mathcal{W} are path dependent one can also express Equation 4.17 in integral form. Therefore, rewriting Equation 4.17 as,

$$\int dx(\nabla\mathcal{Q}-\nabla\mathcal{W})+\delta\int dx(k\nabla\mathcal{Q}-k'\nabla\mathcal{W})+\ell\int dx\nabla\cdot(\nabla\mathcal{Q}-\nabla\mathcal{W})+\tau\int dt(\ddot{\mathcal{Q}}-\ddot{\mathcal{W}}) = 0 \quad (5.1)$$

If we consider a circulation of the fluid volume during convection, the first two integrals vanish as \mathcal{Q} and \mathcal{W} are path-dependent. Therefore, Equation 5.1 can be

rewritten after making the substitution, $\ell/\tau = u$ as,

$$u \int dx \nabla \cdot (\nabla \mathcal{Q} - \nabla \mathcal{W}) + \int dt (\ddot{\mathcal{Q}} - \ddot{\mathcal{W}}) = 0 \quad (5.2)$$

At steady-state, the time-dependence goes away and we are left with the following form,

$$u \int dx \nabla \cdot (\nabla \mathcal{Q} - \nabla \mathcal{W}) = \int dx \int dV \nabla \cdot u (\nabla \mathcal{Q} - \nabla \mathcal{W}) = 0 \quad (5.3)$$

Using Gauss theorem, one can transform the volume integral in Equation 5.3 into a surface integral over the boundary of the volume element.

$$\int dV \nabla \cdot u (\nabla \mathcal{Q} - \nabla \mathcal{W}) = \int ds (\nabla \mathcal{Q} - \nabla \mathcal{W}) \cdot u \hat{\mathbf{n}} \quad (5.4)$$

Since, the right-hand side of Equation 5.3 is zero, $(\nabla \mathcal{Q} - \nabla \mathcal{W}) \cdot \vec{u} = 0$. If one computes the gradients, $\nabla \mathcal{Q}$ and $\nabla \mathcal{W}$ on the top layer of the fluid-film, say the xy -plane, the velocity, \vec{u} then has to be directed perpendicular to them along the z -axis as they are mutually orthogonal to one another. Therefore, the velocity vector, \vec{u} is the fluid flow velocity between the system boundaries, bottom to top and vice-versa. Also, in order for an incompressible fluid to preserve continuity, $\nabla \cdot \vec{u} = 0$. One can develop these ideas in fluid mechanics to extend one's understanding about angular momentum and rotational effects in fluid-flow by defining for example, vorticity $\vec{\omega} = \nabla \times \vec{u}$. Let us consider Equation 5.2 at steady-state,

$$u \int dx \nabla \cdot (\nabla \mathcal{Q} - \nabla \mathcal{W}) = 0 \quad (5.5)$$

Both, u and $\nabla \cdot (\nabla \mathcal{Q} - \nabla \mathcal{W})$ are scalars and $|u| \neq 0$ therefore, from Equation 5.5 one can conclude that $\nabla \cdot (\nabla \mathcal{Q} - \nabla \mathcal{W}) = \nabla^2 \mathcal{Q} - \nabla^2 \mathcal{W} = 0$. Substituting $\mathcal{Q} = TS$ and $\mathcal{W} = \phi$ and expressing the Laplacian in a generic form of second-order derivatives

and rearranging the terms we have,

$$-\partial_\mu\partial_\nu S + \frac{1}{T}\partial_\mu\partial_\nu\phi = 0 \quad (5.6)$$

The quantity, $-\partial_\mu\partial_\nu S$ has long been known as the Ruppeiner metric, $g_{\mu\nu}^R$ which is the negative Hessian of the entropy function [42, 111]. It is a symmetric tensor, the elements of which can be used to determine distance between two equilibrium states, $ds^2 = g_{\mu\nu}^R dx^\mu dx^\nu$. The other quantity, $\partial_\mu\partial_\nu\phi$ is known as the Weinhold metric, $g_{\mu\nu}^W$, and one can relate both as follows,

$$ds_R^2 = \frac{1}{T} ds_W^2 \quad (5.7)$$

Being able to define a metric allows one to imagine the thermodynamic phase-space as a geometric entity. If one intends to understand how the surface profile appears or how far one equilibrium domain (source) is from the other (sink) one uses the metric to quantify the undulations on the manifold. The greater the curvature of the temperature manifold, the further one is away from equilibrium. As a trivial case, we expect a flat manifold for a system at thermal equilibrium.

5.2 Equilibrium Thermodynamics: Extended Discussion

The Hamiltonian of a system is related to its Lagrangian by the following Legendre transformation, $p\dot{q} - H(p, q) = L(q, \dot{q})$. The Maupertuis' action or abbreviated action is given by,

$$\mathcal{S}_0 = \int p dq \quad \text{and} \quad \frac{\partial \mathcal{S}_0}{\partial t} = p\dot{q} \quad (5.8)$$

Substituting Equation 5.8 into the Legendre form we have,

$$\frac{\partial \mathcal{S}_0}{\partial t} = L(q, \dot{q}) + H(p, q) \quad \text{and} \quad \int_{q_1}^{q_2} d\mathcal{S}_0 = \int_{t_1}^{t_2} dt(L + H) \quad (5.9)$$

For a system at equilibrium the Hamiltonian, $H(p, q)$ is the total energy of the system and it is conserved in time ($q(t_1) = q_1$ and $q(t_2) = q_2$). The two action functionals are therefore equal to each other,

$$\mathcal{S}(q, \dot{q}) = \int_{t_1}^{t_2} dt L \equiv \mathcal{S}_0 \quad (5.10)$$

If a system is quasi-statically driven from a state $q(t_1)$ to $q(t_2)$ then the spatially averaged momenta of the system's micro-states can be written as,

$$\langle p \rangle_q = \frac{\int_{q_1}^{q_2} p dq}{\int_{q_1}^{q_2} dq} \quad (5.11)$$

Substituting Equation 5.8 in the above equation and rearranging the terms, $\Delta q \langle p \rangle_q = \mathcal{S}_0$, where $\Delta q = q_2 - q_1$. The action functional and the Hamiltonian are connected to each other by the Hamilton–Jacobi equation,

$$\frac{\partial S(q, \dot{q})}{\partial t} + H(p, q) = 0 \quad (5.12)$$

If the system goes through a (reversible) cyclic process, $q(t_1) = q(t_2)$ then from the first law of thermodynamics we have, $\delta Q = \delta W$. Substituting the Hamiltonian $H(p, q)$ by Q and cycle time t by τ we can rewrite Equation 5.12 as,

$$\frac{\partial S(q, \dot{q})}{\partial t} + H(p, q) \Rightarrow \mathcal{S}_0 + \tau Q = 0 \quad (5.13)$$

From the equipartition theorem we know, $Q = nfk_B T$ where n is the number of particles, f the degree of freedom, k_B the Boltzmann's constant and T the canonical temperature [30]. Therefore,

$$\mathcal{S}_0 + \tau Q = \mathcal{S}_0 + \tau(nfk_B T) \quad \text{or} \quad T = -\frac{\omega \mathcal{S}_0}{nfk_B} = -\frac{\langle \vec{p} \rangle_q \cdot \vec{u}}{nfk_B} \quad (5.14)$$

In the above equation, the cycle frequency $\omega = 1/\tau$ and $\vec{u} = \Delta q/\Delta t$ [22, 24, 104]. Let us consider a simple example where a piston compresses a gas confined inside a cylinder quasi-statically and then allows it to expand. The process is cyclic as $q(t_1) = q(t_2)$, and the micro-states (e_i) distributed inside the piston-cylinder system is given by the Boltzmann's distribution, $\rho(e_i) = \exp(-\beta e_i)/Z$. The inverse temperature, $\beta = 1/k_B T = nf / (\langle \vec{p} \rangle_q \cdot \vec{u})$ from Equation 5.14. The work done by the piston-cylinder during compression is given by,

$$W = -P\Delta V = -\int_1^2 P dV = -\frac{1}{A} \int_1^2 \dot{p}(A dq) = -\vec{u} \int_1^2 dp \quad (5.15)$$

From the ideal gas equation we have, $P\Delta V = nfk_B \Delta T$. Therefore, Equation 5.15 can be written as, $nfk_B \Delta T = -\vec{u} \Delta p$ which further reduces for to $\langle T \rangle = (\vec{u} \cdot \langle p \rangle_q) / nfk_B$ where $\langle T \rangle$ is the canonical temperature of the piston-cylinder system [112].

5.3 Ising Model, Kuramoto Oscillators, and Turbulent Convection

We look for connections between the Rayleigh-Bénard convection system, the two-dimensional square-lattice Ising model and the Kuramoto model as these systems

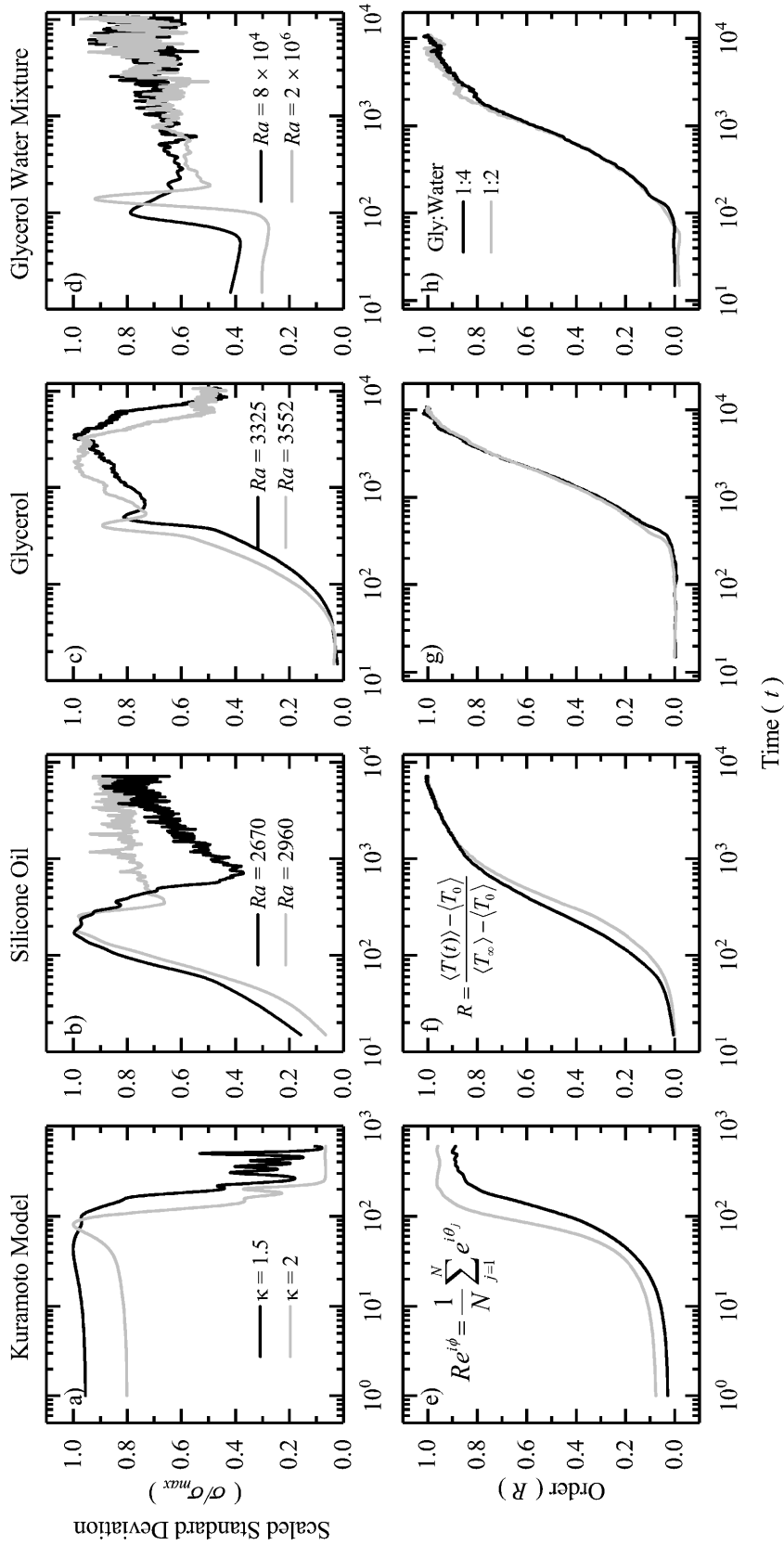


Figure 5.1: a) Figure shows the scaled standard deviation (σ/σ_{max}) of the angular frequency as a function of time (log-scale) in a two-dimensional Kuramoto system on a lattice for different coupling strengths (κ). b) - d) Figures show scaled standard deviation of the temperature as a function of time (log-scale) for different fluid samples in a Rayleigh-Bénard convection system. Note that the Rayleigh number (Ra) changes from non-turbulent to turbulent. e) - h) Figures show the evolution of the order parameter (R) as a function of time (log-scale) for the four systems [9].

when driven out-of-equilibrium give rise to emergent spatio-temporal order through self-organization [8,9]. A common feature of these systems is that the entities that self-assemble are coupled to one another in some way, either through local interactions or through a continuous media [113,114]. Therefore, the general nature of non-equilibrium fluctuations of the intrinsic variables in these systems are found to follow similar trends as order emerges. In Figure 5.1, we plot the scaled standard deviation of the intrinsic variable and emergent order as a function of time for the Kuramoto system and the Rayleigh-Bénard convection. The intrinsic variable in the Kuramoto system is the angular frequency of the oscillators (ω_i) which collapses to a common frequency (Ω) as the system achieves synchronization. Similarly, in the Rayleigh-Bénard system spatially-averaged temperature ($\langle T(t) \rangle$) plays the same role. As the system approaches a steady-state, $\langle T(t) \rangle \rightarrow \langle T_\infty \rangle$, where $\langle T_\infty \rangle$ is the spatially-averaged steady-state temperature of the system. In Figure 5.1a, we plot the scaled standard deviation for the Kuramoto model as a function of time for two values of the coupling strength, $\kappa = 1.5$ and $\kappa = 2$. It is evident from the theory and the plot in Figure 5.1e that order emerges faster ($R \rightarrow 1$) in the case of higher coupling strength. At time-step, $t = 100$ one can observe that at least more than half of the oscillators present in the system are synchronized (from Figure 5.1e) and therefore one observes a sharp decline in the scaled standard deviation plot in Figure 5.1a. Later one can notice that as $t \geq 110$ there is a sudden spike in the standard deviation as order increases further. The reason for this could be attributed to a mixture of synchronized and unsynchronized oscillators as $R < 1$. As time progresses, the natural frequencies of all the oscillators approach closer to mean-field common frequency. However, due to their equally random phase orientations, some of the oscillators reach the common frequency and lock themselves in that state earlier than the other. A situation like this although reduces the standard deviation when com-

pared to the randomized initial state it however increases the standard deviation at an instant when these two groups of oscillators start oscillating simultaneously, one with low fluctuations and the other with higher fluctuations. As one would expect, this scenario appears to last longer in the case of lower coupling strength among the oscillators because of more unsynchronized oscillators than synchronized ones at any given instant in time. Following our results from the Kuramoto system we look at the Rayleigh–Bénard convection in the remaining panels of Figure 5.1. We show results from three different fluid samples: silicone oil, glycerol and glycerol–water mixture (1 : 4 and 1 : 2 by volume). The three fluid samples allow us to explore a wide range of Rayleigh numbers. There is no well–defined order parameter in a Rayleigh–Bénard system, therefore we define one based on the thermal profile at steady–state as,

$$R = \frac{\langle T(t) \rangle - \langle T_0 \rangle}{\langle T_\infty \rangle - \langle T_0 \rangle}, \text{ such that } 0 \leq R \leq 1, \text{ when } \langle T_0 \rangle \leq \langle T(t) \rangle \leq \langle T_\infty \rangle \quad (5.16)$$

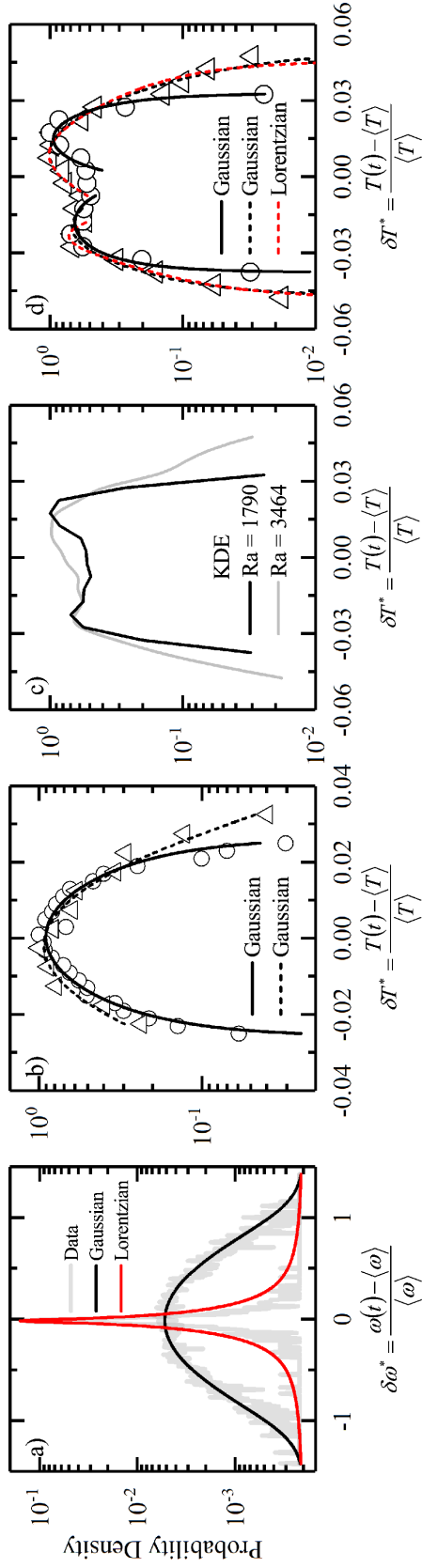
Here, $\langle T(t) \rangle$ represents spatially–averaged temperature at any instant in time, $\langle T_0 \rangle$ represents spatially–averaged temperature at initial equilibrium state (room temperature) and $\langle T_\infty \rangle$ represents spatially–averaged temperature at a non–equilibrium steady–state. For each of the fluid samples we look at the scaled standard deviation plots as order emerges. In the case of silicone oil sample, the fluid being more stable due to its high viscosity, $\nu = 150 \text{ cSt}$ and low Rayleigh numbers we see a decline in the fluctuations in Figure 5.1b. This decline can be mapped to the first instance when convection cells start to appear in the system. The fluctuation reaches a minima when a number of cells have fully formed and nucleated at the center of the copper pan. As the system has not yet reached a steady–state for atleast another $\sim 10^3$ time–steps (see Figure 5.1f) the temperature keeps on rising and hence, the

standard-deviation. With Rayleigh numbers being almost in a similar range, we see a different characteristic with glycerol as our working fluid. Glycerol being a much lighter fluid with viscosity atleast a magnitude lower than silicone oil first nucleates into convection cells which remain stable for sometime, but quickly divides into smaller cells. This two-step nucleation results into two regions of decline in the standard deviation plot as shown in Figure 5.1c. In Figure 5.1d, we look at thermal fluctuations in glycerol-water mixtures. The standard-deviation appears to decline much faster and earlier than the earlier plots (at around time-step, $t = 10^2$), but it lasts for a much shorter duration. The reason for this appears to be lower viscosities ($\sim 10^{-2} cSt$) and higher Rayleigh numbers for the glycerol-water mixtures. Therefore, nucleation not only happens early but also spreads at a faster rate throughout the pan. Following which, they break down into smaller and smaller domains which dissipate heat rather chaotically as the system enters a turbulent regime. One can observe this from the amount of noise in the standard deviation plots, the magnitude of which keeps on increasing with time. Moreover, the system also does not reach a steady-state as one can see in Figure 5.1h, where the order as a function of time seems to be monotonic near $R = 1$ rather than being asymptotic [9, 113].

The similarities between the Kuramoto model and the Rayleigh-Bénard convection are striking. If the extent of synchronization in the Kuramoto model is considered as a measure of order then the Rayleigh-Bénard convection also shows similar trends as it reaches a non-equilibrium steady-state. Since, matter does not leave the system, the continuity equation is preserved. At room temperature equilibrium state, the velocity vectors are randomly oriented, therefore the net directional component of the velocity field cancels itself out. While, a steady-state leads to a well-defined (and directed) velocity field which transports heat from the bottom of the copper pan (hot) to the top layer of the fluid film (cold). Therefore,

emergent order in the Rayleigh–Bénard system corresponds to synchronization of the frequencies of individual convection cells as the system reaches a steady–state temperature. Thus, $\omega = d\theta/dt = 2u_\infty/l$ where $l/2$ is the half thickness of the fluid film and the steady-state velocity, $\vec{u}_\infty \propto \nabla T$ where ∇T is the thermal gradient across the fluid film thickness. In Figure 5.2, we plot the probability densities of the scaled fluctuation of the intensive variables for the initial randomized state and compare them with the final synchronized state for the Kuramoto model and the Rayleigh–Bénard system. Fluctuation in the Kuramoto system is measured by the deviation of the natural frequency of an oscillator from the mean frequency of the system, $\delta\omega = \omega(t) - \langle\omega\rangle$. This deviation in the natural frequencies of the oscillator is scaled by the mean frequency of the system, which we define as scaled fluctuation for the Kuramoto system, $\delta\omega^* = \delta\omega/\langle\omega\rangle$. Once the oscillators are fully synchronized, $\langle\omega\rangle \rightarrow \Omega$. Similarly, in the Rayleigh–Bénard convection we define thermal fluctuation as $\delta T = T(t) - \langle T \rangle$, and $\delta T^* = \delta T/\langle T \rangle$. At room–temperature equilibrium, $\langle T \rangle \rightarrow T_0$ and at steady–state, $\langle T \rangle \rightarrow T_\infty$. As an equilibrium state corresponds to symmetry conservation, one expects to obtain normal fluctuations in the initial state. In Figure 5.2a and 5.2b, we plot the scaled fluctuation distribution for the Kuramoto oscillators and the Rayleigh–Bénard convection respectively in their initial state. We can clearly see that the data obeys very well with the Gaussian fits centered around the origin. For the final fully synchronized state of the oscillators one would expect that a probability density function which would take the form of a delta function sharply centered at the origin such that,

$$\delta(x) = \begin{cases} 0 & x \neq 0 \\ \infty & x = 0 \end{cases} \quad \text{and} \quad \int_{-\epsilon}^{+\epsilon} dx \delta(x) = 1 \quad \text{if} \quad 0 \in [-\epsilon, +\epsilon] \quad (5.17)$$



Scaled Fluctuations

Figure 5.2: a) Figure shows the probability density functions (log-scale) for the scaled angular frequency fluctuation ($\delta\omega^*$). The initial randomized state data is fit with a Gaussian (in black) and the final state data is fit with a Lorentzian (in red). b) Figure shows the probability density functions (log-scale) for the scaled thermal fluctuation (δT^*) for two different fluid samples at room temperature along with respective Gaussian fits. c) Figure shows the probability density functions (log-scale) for the scaled thermal fluctuation for two different fluid samples at steady-state along with kernel density estimates (KDE). Note that in the final state the two samples correspond to two separate Rayleigh numbers. d) Figure shows the probability density functions (log-scale) for the scaled thermal fluctuation for two different fluid samples at steady-state along with respective Gaussian (in black) and Lorentzian (in red) tails. The absence of sufficient data points prevent us from fitting the final state data of the $Ra = 1790$ sample with a Lorentzian function [9].

Note that in the above equation, $x = \delta\omega^*$. A realistic approximation to such a distribution when there are tails in the data is a Lorentzian function,

$$\delta(x) = \lim_{\epsilon \rightarrow 0} \frac{1}{\pi} \frac{\epsilon}{x^2 + \epsilon^2} \quad (5.18)$$

Therefore, a Lorentzian function of the form as shown in Equation 5.18 when fitted to the Kuramoto data for the final synchronized state, and we get a very good agreement between the fit and the data as seen from Figure 5.2a. The tail present in the data is captured by the functional part which decays as, $1/x^2$ in the neighborhood of $0 \in [-\epsilon, +\epsilon]$. In the case of the Rayleigh–Bénard convection we cannot expect to see a single sharply peaked distribution centered around the origin for the scaled thermal fluctuations. As we can see from Figure 5.2c and 5.2d, the data shows the presence of two peaks (or bimodality). In Figure 5.2c, we plot the kernel density estimates to determine the shape of the probability density function for the two experimental trials with different Rayleigh numbers. In Figure 5.2d, we proceed to fit the data piece–wise. We choose individual tails and fit them with a pair of Gaussian fit functions (in black) and then with a pair of Lorentzian fit functions (in red). As we can see from our plots in Figure 5.2d, both Gaussian and Lorentzian fits superimpose over one another. The difference between the center of the two peaks is about 0.04 units with one peaking in the positive domain and the other in the negative. Therefore, one peak signifies the contribution of the upward plumes and the other of the the downward plumes. We are still unsure of the fact that how the fit functions from the two tails merge into one another. This is in agreement with our previous discussions on the bimodal nature of the thermal fluctuations in the Rayleig–Bénard system [4, 6, 7].

To conclude, in the mean–field Kuramoto model the final synchronous state

being unique allows for the existence of a sharply peaked delta-type distribution, which in reality is best illustrated by a Lorentzian fit. In the case of a non-turbulent Rayleigh-Bénard convection at steady-state we find that there exist two possible states due to the existence of spatial thermal gradients which are stable in time. These stable spatial gradients lead to the emergence of two local equilibrium-like regions, fluctuations within which can be best represented by respective Gaussian distributions [6,7].

Chapter 6

Discussion and Conclusion

The lack of a theoretical framework makes systems that are out-of-equilibrium difficult to study. However, the Rayleigh–Bénard convection, with controllable system variables and access to all measurable quantities is an attractive platform to shed light that may guide theoretical development. In this study, the Rayleigh–Bénard system is used as a prototype to gain insights about far-from-equilibrium thermodynamics. Equilibrium behavior is typically easy to visualize, as at equilibrium, all macroscopic thermodynamic variables collapse into fixed points in phase-space [27, 30, 32]. Temperature, which plays a key role in equilibrium thermodynamics, is often quoted as a bad thermodynamic variable to characterize far-from-equilibrium systems, and hence should not be used to describe out-of-equilibrium behavior. This notion is technically sound, as macroscopic variables when far-from-equilibrium are constantly changing in time and no descriptive state-function can possibly be written. Although, when deviations are linear and relatively small, the equilibrium description can be extended under the claims of local equilibrium hypothesis. Nevertheless, even after 200 years of effort, a general theory of far-from-equilibrium thermodynamics is currently missing, and is still quoted as “work

in progress” [37, 100]. The argument against the use of temperature as a measure to theorize far-from-equilibrium thermodynamics although logically valid does not provide a way to solve this long-standing problem. This work seeks to provide experimental observations to stimulate theoretical progress.

A remarkable observation from our analysis of the steady-state thermal images is that local equilibrium-like regions appear to spatially coexist in an out-of-equilibrium system driven presumably by the partitioning of the heat energy flow into entropic and coherent work (the convection circulation). The system is therefore non-ergodic as a whole, but is ergodic in equilibrium-like sub-regions that do not exhibit a pattern in time, but not over the entire film. Since, time translation symmetry is preserved, any macroscopic description of the system should be found to conserve energy (or have applicable the first law of thermodynamics). As translation symmetry is broken over the whole film, there must exist internal gradients of temperature between adjacent regions, the internal coherent work that drives the convective flow of fluid is also maintaining these internal temperature gradients. The second law is well preserved for the macroscopic description of the system, locally however it gets violated due to the emergence of structures and internal gradients [11, 14, 26, 29, 57, 115, 116]. The translation symmetry, thus broken can possibly explain the peculiar nature of the standard deviation plots during heating and cooling. As the system is heated, local equilibrium-like regions start to emerge which causes the system to start getting correlated. As the correlations get stronger, the system starts behaving as collections of local equilibrium-like domains. As the fluctuations between these domains get stronger they start dominating the fluctuations elsewhere which gives rise to Casimir like effect [117–121]. Due to the finite size of the system these effects propagate at a much faster rate than mere thermal diffusion. This is readily observed in the sudden decline of the standard deviation

during heating. While cooling, the domains disintegrate and the system becomes weakly correlated, thus the strong fluctuations almost immediately disappear.

Moving on to the theoretical ideas presented in this paper, we attempt to derive a thermodynamic equation of state from a first principles consideration. The coordinate basis that describes the system is endowed with a metric and therefore can be described as a metric space. Since, each point in the metric space has a well-defined temperature associated with it, one can describe the temperature as a continuous bounded function inside the system which maps each point in space (\mathbb{R}^3) to the real field (\mathbb{R}). We can comment on the mathematical nature of the temperature function with a considerable degree of certainty because of the experimental evidence present before us. Our derivation thus rests on these crucial mathematical properties of sets and subsets of the state scalar such as, continuity and compactness. A scenario where a sequence of the state-scalar fails converge, such as in a turbulent flow system the current version of the theory will lose its significance. In our proposed formalism, the thermodynamic Lagrangian density involves two components, the internal work or the coherent part which gives rise to emergent order, and the internal dissipation or the incoherent part which acts as the internal sink. The salient feature of our theory is the description of the thermodynamic Lagrangian in terms of a scalar-field unlike the conventional description based on coordinates and velocities [22, 23, 25, 107, 122–126]. On minimizing the action functional on this scalar manifold one determines the ‘trajectory’ that connects the local equilibrium-like domains in space. The equation of motion actually describes the equation of state for the system as it is driven out-of-equilibrium. In Equation 4.17, we present the thermodynamic equation of state with small perturbations as a function of the scalar-field and its gradients. One can see clearly that the characteristic constants, (ℓ, τ) emerge as a consequence (than a parameter) from our derivation. These con-

stants will have contextual significance. For example, if the characteristic length is fluid thickness and characteristic time, the time it takes to complete a circulation, then we have a convective flow velocity, \vec{u} . For an incompressible fluid the continuity equation yields, $\nabla \cdot \vec{u} = 0$. One can extend these ideas more specifically to the Rayleigh–Bénard system by defining not one, but two thermodynamic scalars to describe the mathematical nature of the manifold, X^α and X^β . If we consider the equation of state as derived in Equation 4.17 in some more detail. The heat and the work differentials can be expressed in terms of the intensive variables of the system. Since, $\delta Q \propto (\langle X_i^\alpha \rangle - \langle X_j^\alpha \rangle)$ and $j_{ij} \propto (\langle X_i^\alpha \rangle - \langle X_j^\alpha \rangle)$, we can state that $\delta Q \propto j_{ij}$. The proportionality constant gives the values for the transport coefficients during reciprocal flows. Also, for a viscous fluid media one can express the work differential as, $\delta W = X_{ij}^\beta d\epsilon_{ij} + \rho(\vec{u} \cdot \vec{u})$ where X_{ij}^β is a second rank stress tensor and ϵ_{ij} a second rank strain tensor. In case of pure compression (or expansion) one takes the trace of the stress tensor. Thus, $\delta W = -X^\beta \delta_{ij} d\epsilon_{ij} + \rho(\vec{u} \cdot \vec{u}) = -X^\beta + \rho(\vec{u} \cdot \vec{u})$. To be able to derive the equation of state that includes a combination of intensive state variable is a significant challenge.

In conclusion, our experimental study on the Rayleigh–Bénard convection system along with our field–theoretic formalism provides a novel way to understand pattern formation in complex systems that have been driven out–of–equilibrium.

Bibliography

- [1] Heinrich M Jaeger and Andrea J Liu. Far-from-equilibrium physics: An overview. *arXiv:1009.4874*, 2010.
- [2] National Research Council et al. *Condensed-matter and materials physics: The science of the world around us*. National Academies Press, 2007.
- [3] Mohan Srinivasarao, Germano S Iannacchione, and Atul N Parikh. Biologically inspired far-from-equilibrium materials. *MRS Bulletin*, 44(2):91–95, 2019.
- [4] Atanu Chatterjee and Germano Iannacchione. The many faces of far-from-equilibrium thermodynamics: Deterministic chaos, randomness, or emergent order? *MRS Bulletin*, 44(2):130–133, 2019.
- [5] Herbert Goldstein. *Classical mechanics*. Pearson Education India, 2011.
- [6] Atanu Chatterjee, Yash Yadati, Nicholas Mears, and Germano Iannacchione. Coexisting ordered states, local equilibrium-like domains, and broken ergodicity in a non-turbulent rayleigh-bénard convection at steady-state. *Scientific reports*, 9(1):10615, 2019.
- [7] Yash Yadati, Nicholas Mears, and Atanu Chatterjee. Spatio-temporal characterization of thermal fluctuations in a non-turbulent rayleigh-bénard convec-

- tion at steady state. *Physica A: Statistical Mechanics and its Applications*, page 123867, 2019.
- [8] Nicholas Emerson Mears. Stochastic simulations of far-from-equilibrium thermodynamics. 2019.
- [9] Atanu Chatterjee, Nicholas Mears, Yash Yadati, and Germano S Iannacchione. An overview of emergent order in far-from-equilibrium driven systems: From kuramoto oscillators to rayleigh–bénard convection. *Entropy*, 22(5):561, 2020.
- [10] Shin Etsu Silicone-Global. <http://www.shinetsusilicone-global.com/catalog/>.
- [11] Alfred Wehrl. General properties of entropy. *Reviews of Modern Physics*, 50(2):221, 1978.
- [12] Francis Heylighen et al. The science of self-organization and adaptivity. *The encyclopedia of life support systems*, 5(3):253–280, 2001.
- [13] Elliott H Lieb and Jakob Yngvason. The physics and mathematics of the second law of thermodynamics. *Physics Reports*, 310(1):1–96, 1999.
- [14] Leonid M Martyushev and Vladimir D Seleznev. Maximum entropy production principle in physics, chemistry and biology. *Physics reports*, 426(1):1–45, 2006.
- [15] Mark C Cross and Pierre C Hohenberg. Pattern formation outside of equilibrium. *Reviews of modern physics*, 65(3):851, 1993.
- [16] L Huber, R Suzuki, T Krüger, E Frey, and AR Bausch. Emergence of coexisting ordered states in active matter systems. *Science*, 361(6399):255–258, 2018.

- [17] Gregoire Nicolis. Self-organization in nonequilibrium systems. *Dissipative Structures to Order through Fluctuations*, pages 339–426, 1977.
- [18] Georgi Yordanov Georgiev, Atanu Chatterjee, and Germano Iannacchione. Exponential self-organization and moore?s law: Measures and mechanisms. *Complexity*, 2017, 2017.
- [19] Georgi Georgiev, Michael Daly, Erin Gombos, Amrit Vinod, and Gajinder Hoonjan. Increase of organization in complex systems. *World Academy of Science, Engineering and Technology: International Journal of Mathematical and Computational Sciences*, 6(11):1477, 2012.
- [20] Georgi Yordanov Georgiev, Tommi Aho, Juha Kesseli, Olli Yli-Harja, and Stuart A Kauffman. Action and power efficiency in self-organization: The case for growth efficiency as a cellular objective in escherichia coli. In *Evolution, Development and Complexity*, pages 229–244. Springer, 2019.
- [21] Georgi Georgiev and Iskren Georgiev. The least action and the metric of an organized system. *Open systems & information dynamics*, 9(4):371, 2002.
- [22] Atanu Chatterjee. Thermodynamics of action and organization in a system. *Complexity*, 21(S1):307–317, 2016.
- [23] Umberto Lucia. Probability, ergodicity, irreversibility and dynamical systems. 464(2093):1089–1104, 2008.
- [24] Umberto Lucia. Stationary open systems: A brief review on contemporary theories on irreversibility. *Physica A: Statistical Mechanics and its Applications*, 392(5):1051–1062, 2013.

- [25] Umberto Lucia. Maximum or minimum entropy generation for open systems? *Physica A: Statistical Mechanics and its Applications*, 391(12):3392–3398, 2012.
- [26] Elliott H Lieb and Jakob Yngvason. A guide to entropy and the second law of thermodynamics. pages 353–363, 1998.
- [27] Rudolf Clausius. Über eine veränderte form des zweiten hauptsatzes der mechanischen wärmetheorie. *Annalen der Physik*, 169(12):481–506, 1854.
- [28] Richard P Feynman, Robert B Leighton, and Matthew Sands. *The Feynman lectures on physics, Vol. I: The new millennium edition: mainly mechanics, radiation, and heat*, volume 1. Basic books, 2011.
- [29] Richard C Tolman and Paul C Fine. On the irreversible production of entropy. *Reviews of Modern Physics*, 20(1):51, 1948.
- [30] Josiah Willard Gibbs. *The scientific papers of J. Willard Gibbs*, volume 1. Longmans, Green and Company, 1906.
- [31] Joseph Louis Lagrange. *Mécanique analytique*, volume 1. Mallet-Bachelier, 1853.
- [32] Max Planck. *Treatise on thermodynamics*. Courier Corporation, 2013.
- [33] George D Birkhoff. Proof of the ergodic theorem. *Proceedings of the National Academy of Sciences*, 17(12):656–660, 1931.
- [34] Giovanni Gallavotti. Nonequilibrium thermodynamics. *arXiv:1901.08821*, 2019.
- [35] Paul Glansdorff and Ilya Prigogine. *Thermodynamic theory of structure, stability and fluctuations*, volume 306. Wiley-Interscience New York, 1971.

- [36] Atanu Chatterjee, Georgi Georgiev, and Germano Iannacchione. Aging and efficiency in living systems: Complexity, adaptation and self-organization. *Mechanisms of Ageing and Development*, 163:2–7, 2017.
- [37] José MG Vilar and JM Rubi. Thermodynamics “beyond” local equilibrium. *Proceedings of the National Academy of Sciences*, 98(20):11081–11084, 2001.
- [38] Juan A Acebrón, Luis L Bonilla, Conrad J Pérez Vicente, Félix Ritort, and Renato Spigler. The kuramoto model: A simple paradigm for synchronization phenomena. *Reviews of modern physics*, 77(1):137, 2005.
- [39] Lev Davidovich Landau and Evgenii Mikhailovich Lifshitz. *Course of theoretical physics*. Elsevier, 2013.
- [40] Walter T Grandy Jr. *Entropy and the time evolution of macroscopic systems*, volume 10. Oxford University Press on Demand, 2008.
- [41] Giovanni Gallavotti. Ergodicity: a historical perspective. equilibrium and nonequilibrium. *The European Physical Journal H*, 41(3):181–259, Sep 2016.
- [42] Gavin E Crooks. Measuring thermodynamic length. *Physical Review Letters*, 99(10):100602, 2007.
- [43] Istvan Gyarmati et al. *Non-equilibrium thermodynamics*. Springer, 1970.
- [44] Y Mishin. Thermodynamic theory of equilibrium fluctuations. *Annals of Physics*, 363:48–97, 2015.
- [45] Denis J Evans, Ezechiele Godert David Cohen, and Gary P Morriss. Probability of second law violations in shearing steady states. *Physical review letters*, 71(15):2401, 1993.

- [46] Denis J Evans and Debra J Searles. The fluctuation theorem. *Advances in Physics*, 51(7):1529–1585, 2002.
- [47] Denis J Evans and Debra J Searles. Equilibrium microstates which generate second law violating steady states. *Physical Review E*, 50(2):1645, 1994.
- [48] Christopher Jarzynski. Nonequilibrium equality for free energy differences. *Physical Review Letters*, 78(14):2690, 1997.
- [49] Christopher Jarzynski. Equilibrium free-energy differences from nonequilibrium measurements: A master-equation approach. *Physical Review E*, 56(5):5018, 1997.
- [50] Edward A Milne. The effect of collisions on monochromatic radiative equilibrium. *Monthly Notices of the Royal Astronomical Society*, 88:493, 1928.
- [51] Shu-Tao Ai. Non-equilibrium thermodynamics of ferroelectric phase transitions. *Ferroelectrics*, pages 253–274, 2010.
- [52] David Jou, Jose Casas-Vazquez, and Georgy Lebon. Extended irreversible thermodynamics revisited (1988-98). *Reports on Progress in Physics*, 62(7):1035, 1999.
- [53] SR De Groot and P Mazur. Non equilibrium thermodynamics—north-holland publ. Co., Amsterdam, 1962.
- [54] Eberhard Bodenschatz, David S Cannell, John R de Bruyn, Robert Ecke, Yu-Chou Hu, Kristina Lerman, and Guenter Ahlers. Experiments on three systems with non-variational aspects. *Physica D: Nonlinear Phenomena*, 61(1-4):77–93, 1992.

- [55] Tooru Taniguchi and EGD Cohen. Onsager-machlup theory for nonequilibrium steady states and fluctuation theorems. *Journal of Statistical Physics*, 126(1):1–41, 2007.
- [56] Tooru Taniguchi and EGD Cohen. Nonequilibrium steady state thermodynamics and fluctuations for stochastic systems. *Journal of Statistical Physics*, 130(4):633–667, 2008.
- [57] Lars Onsager. Reciprocal relations in irreversible processes. i. *Physical Review*, 37(4):405, 1931.
- [58] Réka Albert and Albert-László Barabási. Statistical mechanics of complex networks. *Reviews of modern physics*, 74(1):47, 2002.
- [59] Albert-László Barabási and Réka Albert. Emergence of scaling in random networks. *science*, 286(5439):509–512, 1999.
- [60] Atanu Chatterjee, Manju Manohar, and Gitakrishnan Ramadurai. Statistical analysis of bus networks in india. *PloS one*, 11(12):e0168478, 2016.
- [61] Atanu Chatterjee, Gitakrishnan Ramadurai, and Krishna Jagannathan. Contagion processes on urban bus networks in indian cities. *Complexity*, 21(S2):451–458, 2016.
- [62] Atanu Chatterjee. Studies on the structure and dynamics of urban bus networks in indian cities. *arXiv:1512.05909*, 2015.
- [63] Atanu Chatterjee and Gitakrishnan Ramadurai. Scaling laws in chennai bus network. *arXiv:1508.03504*, 2015.
- [64] Ilya Prigogine. Time, structure and fluctuations. *Nobel Lectures in Chemistry 1971-1980*, pages 263–285, 1977.

- [65] Siegfried Grossmann and Detlef Lohse. Fluctuations in turbulent rayleigh-bénard convection: the role of plumes. *Physics of Fluids*, 16(12):4462–4472, 2004.
- [66] W Ross Ashby. Principles of the self-organizing system. In *Facets of systems science*, pages 521–536. Springer, 1991.
- [67] Carlos Gershenson and Francis Heylighen. When can we call a system self-organizing? In *European Conference on Artificial Life*, pages 606–614. Springer, 2003.
- [68] Yoshiki Kuramoto and Ikuko Nishikawa. Statistical macrodynamics of large dynamical systems. case of a phase transition in oscillator communities. *Journal of Statistical Physics*, 49(3-4):569–605, 1987.
- [69] Dongmei Zhang, László Györgyi, and William R Peltier. Deterministic chaos in the belousov-zhabotinsky reaction: Experiments and simulations. *Chaos: An Interdisciplinary Journal of Nonlinear Science*, 3(4):723–745, 1993.
- [70] RP Behringer. Rayleigh-benard convection and turbulence in liquid helium. *Reviews of Modern Physics*, 57(3):657, 1985.
- [71] Ernst L Koschmieder. *Bénard cells and Taylor vortices*. Cambridge University Press, 1993.
- [72] Adrian Bejan. *Convection heat transfer*. John wiley & sons, 2013.
- [73] Dilip Kondepudi and Ilya Prigogine. *Modern thermodynamics: from heat engines to dissipative structures*. John Wiley & Sons, 2014.
- [74] Dilip Kondepudi. *Introduction to modern thermodynamics*. Wiley, 2008.

- [75] Per Bak, Chao Tang, and Kurt Wiesenfeld. Self-organized criticality: An explanation of the $1/f$ noise. *Physical review letters*, 59(4):381, 1987.
- [76] Per Bak. *How nature works: the science of self-organized criticality*. Springer Science & Business Media, 2013.
- [77] Alessandro Vespignani. Modelling dynamical processes in complex socio-technical systems. *Nature physics*, 8(1):32, 2012.
- [78] Markus Karl, Boris Nowak, and Thomas Gasenzer. Tuning universality far from equilibrium. *Scientific reports*, 3:2394, 2013.
- [79] Eberhard Bodenschatz, Werner Pesch, and Guenter Ahlers. Recent developments in rayleigh-bénard convection. *Annual review of fluid mechanics*, 32(1):709–778, 2000.
- [80] Lord Rayleigh. Lix. on convection currents in a horizontal layer of fluid, when the higher temperature is on the under side. *The London, Edinburgh, and Dublin Philosophical Magazine and Journal of Science*, 32(192):529–546, 1916.
- [81] Olga Shishkina, Richard JAM Stevens, Siegfried Grossmann, and Detlef Lohse. Boundary layer structure in turbulent thermal convection and its consequences for the required numerical resolution. *New journal of Physics*, 12(7):075022, 2010.
- [82] Leo P Kadanoff. Turbulent heat flow: structures and scaling. *Physics Today*, 54(8):34–39, 2001.
- [83] Jin-Qiang Zhong, Richard JAM Stevens, Herman JH Clercx, Roberto Verzicco, Detlef Lohse, and Guenter Ahlers. Prandtl-, rayleigh-, and rossby-number

- dependence of heat transport in turbulent rotating rayleigh-bénard convection. *Physical Review Letters*, 102(4):044502, 2009.
- [84] Richard JAM Stevens, Detlef Lohse, and Roberto Verzicco. Prandtl and rayleigh number dependence of heat transport in high rayleigh number thermal convection. *Journal of Fluid Mechanics*, 688:31–43, 2011.
- [85] Rodrigo Segura, Massimiliano Rossi, Christian Cierpka, and Christian J Kähler. Simultaneous three-dimensional temperature and velocity field measurements using astigmatic imaging of non-encapsulated thermo-liquid crystal (tlc) particles. *Lab on a Chip*, 15(3):660–663, 2015.
- [86] Ambrish Pandey, Janet D Scheel, and Jörg Schumacher. Turbulent superstructures in rayleigh-bénard convection. *Nature communications*, 9(1):2118, 2018.
- [87] Sebastian Moller, Joerg Koenig, Christian Resagk, and Christian Cierpka. Influence of the illumination spectrum and observation angle on temperature measurements using thermochromic liquid crystals. *Measurement Science and Technology*, 2019.
- [88] Y-B Du and Penger Tong. Enhanced heat transport in turbulent convection over a rough surface. *Physical Review Letters*, 81(5):987, 1998.
- [89] Y-B Du and Penger Tong. Turbulent thermal convection in a cell with ordered rough boundaries. *Journal of Fluid Mechanics*, 407:57–84, 2000.
- [90] Y-B Du and Penger Tong. Temperature fluctuations in a convection cell with rough upper and lower surfaces. *Physical Review E*, 63(4):046303, 2001.

- [91] Francesca Chillà, Marie Rastello, Sébastien Chaumat, and Bernard Castaing. Ultimate regime in rayleigh–bénard convection: The role of plates. *Physics of Fluids*, 16(7):2452–2456, 2004.
- [92] Jörg Schumacher. Lagrangian dispersion and heat transport in convective turbulence. *Physical Review Letters*, 100(13):134502, 2008.
- [93] F Chillà and J Schumacher. New perspectives in turbulent rayleigh–bénard convection. *The European Physical Journal E*, 35(7):58, 2012.
- [94] Subrahmanyan Chandrasekhar. *Hydrodynamic and hydromagnetic stability*. Courier Corporation, 2013.
- [95] JJ Niemela, L Skrbek, KR Sreenivasan, and RJ Donnelly. Turbulent convection at very high rayleigh numbers. *Nature*, 404(6780):837, 2000.
- [96] Richard JAM Stevens, Roberto Verzicco, and Detlef Lohse. Radial boundary layer structure and nusselt number in rayleigh–bénard convection. *Journal of Fluid Mechanics*, 643:495–507, 2010.
- [97] Yin Wang, Xiaozhou He, and Penger Tong. Boundary layer fluctuations and their effects on mean and variance temperature profiles in turbulent rayleigh–bénard convection. *Physical Review Fluids*, 1(8):082301, 2016.
- [98] Mahendra K Verma. *Physics of Buoyant Flows: From Instabilities to Turbulence*. World Scientific, 2018.
- [99] Mahendra K. Verma. Asymmetric energy transfers in driven nonequilibrium systems and arrow of time. *The European Physical Journal B*, 92(9):190, 2019.

- [100] Andrey Nikolaevich Kolmogorov. The local structure of turbulence in incompressible viscous fluid for very large reynolds numbers. In *Dokl. Akad. Nauk SSSR*, volume 30, pages 299–303, 1941.
- [101] Georgi Yordanov Georgiev and Atanu Chatterjee. The road to a measurable quantitative understanding of self-organization and evolution. In *Evolution and Transitions in Complexity*, pages 223–230. Springer, 2016.
- [102] Norbert Wiener et al. Generalized harmonic analysis. *Acta mathematica*, 55:117–258, 1930.
- [103] Atanu Chatterjee. Principle of least action and convergence of systems towards state of closure. *International Journal of Physical Research*, 1(1):21–27, 2013.
- [104] Vladimir García-Morales, Julio Pellicer, and José A Manzanares. Thermodynamics based on the principle of least abbreviated action: entropy production in a network of coupled oscillators. *Annals of Physics*, 323(8):1844–1858, 2008.
- [105] A Puglisi, A Sarracino, and A Vulpiani. Temperature in and out of equilibrium: A review of concepts, tools and attempts. *Physics Reports*, 709:1–60, 2017.
- [106] Janet D Scheel and Jörg Schumacher. Predicting transition ranges to fully turbulent viscous boundary layers in low prandtl number convection flows. *Physical Review Fluids*, 2(12):123501, 2017.
- [107] Sarada G Rajeev. Quantization of contact manifolds and thermodynamics. *Annals of Physics*, 323(3):768–782, 2008.
- [108] Shripad P Mahulikar, Tapan K Sengupta, Nidhi Sharma, and Pallavi Rastogi. Thermodynamic merger of fluctuation theorem and principle of least action:

- Case of rayleigh–taylor instability. *Journal of Non-Equilibrium Thermodynamics*, 44(4):363–371, 2019.
- [109] Bernard Beauzamy. *Introduction to Banach spaces and their geometry*, volume 68. Elsevier, 2011.
- [110] Jean Dieudonné. *Foundations of Modern Analysis, enlarged and corrected printing*. Academic Press, 1969.
- [111] George Ruppeiner. Riemannian geometry in thermodynamic fluctuation theory. *Reviews of Modern Physics*, 67(3):605, 1995.
- [112] Atanu Chatterjee and Germano Iannacchione. Time and thermodynamics extended discussion on “time & clocks: A thermodynamic approach”. *Results in Physics*, page 103165, 2020.
- [113] Atanu Chatterjee, Nicholas Mears, Abigail Charest, Saad Algarni, and Germano Iannacchione. High-resolution experimental study and numerical modeling of population dynamics in a bacteria culture. *arXiv:1912.08389*, 2019.
- [114] Atanu Chatterjee. Energy, entropy and complexity: Thermodynamic and information-theoretic perspectives on ageing. *M. Kyriazis (2016) Challenging Ageing: The anti-senescence effects of Hormesis, Environmental Enrichment, and Information Exposure*. Bentham Science, 2016.
- [115] Vivek Sharma and Arto Annala. Natural process–natural selection. *Biophysical chemistry*, 127(1-2):123–128, 2007.
- [116] Ville RI Kaila and Arto Annala. Natural selection for least action. *Proceedings of the Royal Society A: Mathematical, Physical and Engineering Sciences*, 464(2099):3055–3070, 2008.

- [117] Dominic Vella, John S Wettlaufer, et al. Fluctuation spectra and force generation in nonequilibrium systems. *Proceedings of the National Academy of Sciences*, page 201701739, 2017.
- [118] Atanu Chatterjee and Germano Iannacchione. Non-equilibrium thermodynamics from first principles. *Bulletin of the American Physical Society*, 63, 2018.
- [119] Yash Yadati, Sean McGrath, Atanu Chatterjee, Georgi Georgiev, and Germano Iannacchione. A detailed thermodynamic study of rayleigh-benard cells. *Bulletin of the American Physical Society (BAPS)*, Abstract: K47.00001, 2018.
- [120] Atanu Chatterjee, Georgi Georgiev, Than Vu, and Germano Iannacchione. Benard cells as a model for entropy production, entropy decrease, and action minimization in self-organization. *Conference on Complex Systems (CCS17)*, 2017.
- [121] Atanu Chatterjee and Germano Iannacchione. Equation of state for a far-from-equilibrium thermodynamic system with emergent scales at steady-state. *Bulletin of the American Physical Society*, 2020.
- [122] KS Glavatskiy. Lagrangian formulation of irreversible thermodynamics and the second law of thermodynamics. *The Journal of chemical physics*, 142(20):204106, 2015.
- [123] A Stokes. A lagrangian approach to classical thermodynamics. *EPL (Europhysics Letters)*, 117(3):30002, 2017.
- [124] François Gay-Balmaz and Hiroaki Yoshimura. A lagrangian formalism for nonequilibrium thermodynamics. *arXiv:1510.00792*, 2015.

- [125] Cenalo Vaz. A lagrangian description of thermodynamics. *arXiv:1110.6152*, 2011.
- [126] Jean-Pierre Badiali. Role of closed paths in the path integral approach of statistical thermodynamics. In *Journal of Physics: Conference Series*, volume 604, page 012002. IOP Publishing, 2015.